



# **Version 3.0 of the Crocus snowpack model**

Matthieu Lafaysse<sup>1</sup>, Marie Dumont<sup>1</sup>, Basile De Fleurian<sup>1</sup>, Mathieu Fructus<sup>1</sup>, Rafife Nheili<sup>1</sup>, Léo Viallon-Galinier<sup>1</sup>, Matthieu Baron<sup>1</sup>, Aaron Boone<sup>2</sup>, Axel Bouchet<sup>1</sup>, Julien Brondex<sup>1,4</sup>, Carlo Carmagnola<sup>1</sup>, Bertrand Cluzet<sup>1</sup>, Kévin Fourteau<sup>1</sup>, Ange Haddjeri<sup>1,4</sup>, Pascal Hagenmuller<sup>1</sup>, Giulia Mazzotti<sup>1,4</sup>, Marie Minvielle<sup>2</sup>, Samuel Morin<sup>1</sup>, Louis Quéno<sup>1,5</sup>, Léon Roussel<sup>1</sup>, Pierre Spandre<sup>1</sup>, François Tuzet<sup>1</sup>, and Vincent Vionnet<sup>1,3</sup>

**Correspondence:** Matthieu Lafaysse (matthieu.lafaysse@meteo.fr)

Abstract. This article presents a comprehensive description of the 3.0 stable release of the Crocus snowpack model in the SUR-FEX modelling platform. It synthesizes and harmonizes a number of equations disseminated in various previous publications, introduces a number of unpublished parameterizations and includes new developments implemented since 2012. Among the novelties, an explicit representation of the evolution of impurity mass in snow (e.g. black carbon, mineral dust) allows representing their impact on solar radiation absorption in the snowpack at different wavelengths and their feedback on all snowpack properties. The model also allows the formation of surface ice layers due to freezing rain. In addition, Crocus is coupled to the MEB "big-leaf" vegetation scheme and can therefore be applied in forested areas. A module for snow management can also be optionally activated to simulate the snowpack on ski slopes in ski resorts. The model can be coupled with various blowing snow schemes. The MEPRA expert system which analyses the mechanical stability of the simulated snowpack has been implemented directly within SURFEX. A multiphysics version of the model (ESCROC) was also developed by implementing from 2 to 4 parameterizations from the literature for each physical process represented by empirical parameterizations. The different combinations allow the quantification of simulations uncertainty for various applications. Finally, a technical solution was proposed for externalized applications allowing the use of the scheme in other Land Surface Models. The paper also reviews the available scientific evaluations and applications of the model. It describes its numerical efficiency and the main scientific and technical challenges providing guidance for the future of snow modelling.

#### 1 Introduction

A large variety of snowpack modelling systems (e.g. Krinner et al., 2018) have been developed for several decades for various applications (Largeron et al., 2020): the computation of energy fluxes at the atmosphere-cryosphere interface in climate modelling and numerical weather prediction; hydrological simulations for discharge forecasting, water resources and hydropower

<sup>&</sup>lt;sup>1</sup>Météo-France, CNRS, Univ. Grenoble Alpes, Univ. Toulouse, CNRM, Centre d'Études de la Neige, Grenoble, France

<sup>&</sup>lt;sup>2</sup>Météo-France, CNRS, Univ. Toulouse, CNRM, Toulouse, France

<sup>&</sup>lt;sup>3</sup>Meteorological Research Division, Environment and Climate Change Canada, Dorval, QC, Canada

<sup>&</sup>lt;sup>4</sup>now at Institut des Géosciences de l'Environnement (IGE), CNRS, INRAE, IRD, Grenoble INP, Univ. Grenoble Alpes, Grenoble, France

<sup>&</sup>lt;sup>5</sup>now at WSL Institute for Snow and Avalanche Research (SLF), Davos, Switzerland



30



management; physical process studies in the snowpack; avalanche hazard forecasting; glacier mass balance assessment; sea ice modelling; etc. The most detailed snowpack models include a detailed representation of the snowpack stratigraphy as well as an explicit representation of some microstructural properties of the snow layers through the implementation of empirical parameterization of snow metamorphism. There is a relatively limited number of snowpack models with such a level of detail: mainly the "Swiss" SNOWPACK model (Lehning et al., 1999), the "American" SNTHERM model (Jordan, 1991), the "Japanese" SMAP model (Niwano et al., 2012) and the "French" Crocus model. The latter has been initially developed by Brun et al. (1989, 1992) and was implemented in the early 2010s in the SURFEX platform of surface modelling (Masson et al., 2013) to facilitate coupling with atmospheric models and the other components of surface modelling, especially soil and vegetation schemes of the ISBA Land Surface Model. The last description of the model was published by Vionnet et al. (2012) after this major evolution.

However, numerous evolutions of the model have been implemented after Vionnet et al. (2012). Some of them are only partly described in dedicated scientific publications (Carmagnola et al., 2014; Spandre et al., 2016; Lafaysse et al., 2017; Tuzet et al., 2017; Vionnet et al., 2018; Quéno et al., 2018). These articles were generally published before the merging of all new developments in a unique and stable code version. A comprehensive and accurate description of the state of the last official model release is therefore missing. This lack of documentation has been identified by Menard et al. (2021) as one of the main factors of human errors in numerical simulations. The purpose of this paper is to provide an updated reference with all the functionalities available in the latest stable release of the model. To help the users to find any information they may need to understand the model implementation, all the equations disseminated in the various papers are reported here either in the main text or in Appendices, including the equations already published in previous references of Brun et al. (1992) and Vionnet et al. (2012) in order to provide a self-sufficient reference describing the whole model. Following the recommendations of Menard et al. (2021), a major effort has been dedicated to check the consistency and comprehensiveness between the code and the equations. The scope of this paper is limited to the snowpack on the ground. The coupled modules representing soil, vegetation and blowing snow remain beyond the scope of this paper and only the terms involved in the coupling are mentioned. More details can be found in the reference publications of the coupled models: Decharme et al. (2016); Boone et al. (2017) for soil and vegetation; Vionnet et al. (2014, 2018) and Baron et al. (2024) for blowing snow, cf. Section 2.4.2. Note that the standalone Crocus model was last designated as version 2.4. This versioning was discontinued by Vionnet et al. (2012) in favor of the SURFEX versioning system. However, due to the impossibility to synchronize Crocus and SURFEX main stable releases and the integration of Crocus in other Land Surface Models, a dedicated versioning is necessary for Crocus. This paper thus describes version 3.0 of Crocus. Section 2 presents all scientific equations necessary to make evolve the state variables of the model. Section 3 presents complementary diagnoses computed as output of the model. Section 4 presents technical features associated with running the model (simulation geometries, numerical efficiency, and associated tools to facilitate running and visualization). Finally, Section 5 reviews the available scientific evaluations of the model and provides an overview of its applications, to discuss the associated confidence and main remaining challenges for the future, including perspectives in terms of data assimilation.





# 2 Physical model

5 Compared to Vionnet et al. (2012), the model has become highly modular with the extension of applications and the development of a multiphysics framework by Lafaysse et al. (2017). The common modelling structure includes the discretization procedure and the solving of the heat diffusion equation which is the core of the model.

#### 2.1 Forcing variables

The model has to be forced with subdaily time series of air temperature  $T_a$  (K) and specific humidity  $q_a$  (kg kg<sup>-1</sup>) at a known level  $z_a$  (m), wind speed U (m s<sup>-1</sup>) at a known level  $z_a$  (m), incoming longwave radiation LW $\downarrow$  (W m<sup>-2</sup>), incoming shortwave direct and diffuse radiation SW<sub>DIR</sub> $\downarrow$  and SW<sub>DIF</sub> $\downarrow$  (W m<sup>-2</sup>), rainfall  $\mathcal{P}_r$  and snowfall  $\mathcal{P}_s$  (kg m<sup>-2</sup> s<sup>-1</sup>) and surface pressure  $P_s$  (Pa). The very low sensitivity of model results to  $P_s$  allows the user to provide constant  $P_s$  values when a time series is not available. The split of global shortwave radiation SW $\downarrow$  between direct and diffuse components is only used with specific model options (coupling with TARTES optical scheme, Section 2.4.9, and/or coupling with MEB big-leaf vegetation scheme, Section 2.4.14). When these options are not activated, a random split between both components is sufficient as only their sum is considered. For users interested in these options without available data to separate both components, the following parameterization as a function of the cosine of the solar zenithal angle  $\mu$  and derived from SBDART clear-sky modelling (Ricchiazzi et al., 1998) at Col de Porte is reasonable in mid-latitude areas and is applied by default in the code if the diffuse components is set to zero:

70 
$$\frac{\text{SW}_{\text{DIF}}}{\text{SW}_{\text{DIR}} + \text{SW}_{\text{DIF}}} = \min\left(\exp\left(-1.549919\mu^3 + 3.735357\mu^2 - 3.524211\mu + 0.029911\right), 1.\right)$$
(1)

Optionally, dry and wet deposition fluxes of Light-Absorbing Particles (LAP)  $W_{d,j}$  and  $W_{w,j}$  (kg m<sup>-2</sup> s<sup>-1</sup>) can be included for each type j depending on the physical option selected for radiative transfer (Section 2.4.9).

#### 2.2 State variables

The prognostic variables (i.e. transmitted from a given time step to the next one) describing each snow layer i are its mass  $m_i$  (kg m<sup>-2</sup>), density  $\rho_i$  (kg m<sup>-3</sup>), enthalpy  $H_i$  (J m<sup>-2</sup>) defined as the energy required to melt the snow layer i (Boone and Etchevers, 2001), age  $A_i$  (days since snowfall), and complementary variables for snow microstructure. The state variables initially used for snow microstructure as described in Vionnet et al. (2012) (dendricity, sphericity, grain size) were replaced by optical diameter  $d_i$  (m) and sphericity  $S_i \in [0,1]$  (Carmagnola et al., 2014). After several years of coexistence, the formulation from Brun et al. (1992) was removed from the code in order to improve its readability but also its efficiency as numerous expensive conditional statements could be removed. This change of state variables does not only affect metamorphism evolution laws but also various equations based on microstructure properties in other simulated processes. All modified equations are provided in the following section or in Appendix. In addition, a historical tracker  $h_i$  is used as a last state variable with its





**Table 1.** Possible values of the historical tracker  $h_i$ 

	Liquid water at any	Faceted crystals at any	More than one
	time before $t$	time before $t$	freezing-melting
			cycle before $t$ .
0	No	No	No
1	No	Yes	No
2	Yes	No	No
3	Yes	Yes	No
4	Yes	No	Yes
5	Yes	Yes	Yes

meaning summarized in Table 1.

Tuzet et al. (2017) added LAP mass contents  $\mathcal{M}_{i,j}$  (kg m<sup>-2</sup>) as new optional state variables for each layer i and LAP type j. Although the code is designed to deal with any number of LAP types, only the parameters corresponding to black carbon and mineral dust are implemented in version 3.0. LAP interact with the other variable states of the model through absorption of solar radiation when the TARTES optical scheme is activated (Section 2.4.9).

Note that the layer thickness  $z_i$  (m), the layer temperature  $T_i$  (K) and the layer mass of liquid water  $l_i$  (kg m<sup>-2</sup>) can be directly derived from the state variables and are used in many parts of the model.

$$z_i = \frac{m_i}{\rho_i} \tag{2}$$

$$T_i = \min(T_0, T_i^*) \tag{3}$$

$$l_i = \max(0, T_i^* - T_0) \frac{m_i c_I}{L_m} \tag{4}$$

where 
$$T_i^* = T_0 + \frac{H_i}{m_i c_I} + \frac{L_m}{c_I}$$
 (5)

95  $T_0$  (K) is the water triple point temperature,  $L_m$  (J kg<sup>-1</sup>) is the latent heat of fusion, and  $c_I$  (J kg<sup>-1</sup> K<sup>-1</sup>) the ice thermal capacity. Note also that the temperature  $\theta_i$  in °C is also used in some parameterizations:

$$\theta_i = T_i - T_0 \tag{6}$$

#### 2.3 Layering

#### 2.3.1 Vertical discretization

One of the main original feature of Crocus compared to the majority of snowpack schemes available in the literature is its Lagrangian vertical discretization based on a dynamical evolution of the number and thicknesses of the numerical snow layers.



105



The number of active layers N varies between  $N_{\min}=3$  and a user-defined maximum  $N_{\max}$  (the default value is 50). Each layer is referenced by the index i which varies from 1 for the surface layer to N for the deepest layer. The main discretization principles described in Vionnet et al. (2012) are still valid in the current version but they have been a bit complexified to solve numerical issues in specific applications. The current article provides the first comprehensive formulation of the algorithm.

First, a similarity criterion D(i, i+1) between adjacent layers i and i+1 is defined. The initial formulation was a Manhattan distance of weighted values of dendricity, sphericity and grain size but it has never been published. The strict variable transformation of Carmagnola et al. (2014) led to a unjustified complexity in the formulation of this distance. Therefore, this distance was simplified in the same spirit by:

110 
$$\begin{cases} D(i,i+1) &= 50(|S_{i+1} - S_i| + 2000 |d_{i+1} - d_i| + \delta_h(i,i+1)) & \text{if } (A_i - A_{i+1}) < 300 \\ D(i,i+1) &= 200 & \text{otherwise} \end{cases}$$
 (7)

where

$$\begin{cases} \delta_h(i,i+1) = 1 & \text{if } (h_i > 1 \text{ and } h_{i+1} \le 1) \text{ or } (h_i \le 1 \text{ and } h_{i+1} > 1) \\ \delta_h(i,i+1) = 0 & \text{otherwise} \end{cases}$$
(8)

The 2000 coefficient is chosen for normalization considering the typical range of  $5.10^{-4}$ m between highest and lowest values of  $d_i$  (Carmagnola et al., 2014) and the range of 1 between highest and lowest values of  $S_i$ . The  $\delta_h$  function avoids the aggregation between cold snow and wet/refrozen snow. The specific case of significant age difference was introduced to avoid the aggregation of a recent snow layer with layers describing permanent snow or glacier. This distance is noted D(n,1) when it is applied between a new snowfall and the surface layer.

When it is necessary to choose two layers to aggregate, a penalty criteria P(i, i+1) is defined by:

$$P(i,i+1) = D(i,i+1) + 25\left(\frac{z_i}{z_i^*} + \frac{z_{i+1}}{z_{i+1}^*}\right)$$
(9)

where  $z_i^*$  (m) is the layer thickness of the optimal attractor profile defined in Appendix A.

Layers  $l_{\mathrm{sup}}$  and  $l_{\mathrm{inf}}$  are the adjacent layers which satisfy:

$$P(l_{\sup}, l_{\inf}) = \min_{i \in [1, N-1]} (P(i, i+1))$$
(10)

The algorithm modifies the thicknesses at the previous time step  $z_i^{t-\Delta t}$  for  $i \in [1, N^{t-\Delta t}]$  towards a new profile  $z_i^t$  for  $i \in [1, N^t]$  following Equation 11 by a succession of exclusive conditional statements depending on the total initial depth  $Z^{t-\Delta t} = \sum_{i=1}^N z_i^{t-\Delta t}$ , the initial thickness of the first layer  $z_1^{t-\Delta t}$ , the thickness of new snowfall to add  $z_n = \frac{m_n}{\rho_n}$  (m), and the initial number of layers  $N^{t-\Delta t}$ . The computations of the mass  $m_n$  (kg m<sup>-2</sup>) and density of new snowfall  $\rho_n$  (kg m<sup>-3</sup>) are described later in Section 2.4.1.



130

135



$$\begin{cases} & \text{If } Z^{1-\Delta t} < Z_{\min} \\ & \text{or } N^{t-\Delta t} < X_{\min} \\ & \text{of } N^{t-\Delta t} < X_{\min} \\ & \text{of } \frac{z_{1}^{t} - \frac{z_{1}^{t}}{z_{1}^{t}} + y \in [1, N^{t}]}{z_{1}^{t} - \frac{z_{1}^{t}}{z_{1}^{t}} + y \in [1, N^{t}]} \\ & \text{or } \frac{z_{1}^{t} - \Delta t}{\Delta t} < 3 \times 10^{-5} \, \text{kg m}^{-2} \, \text{s}^{-3} \, \text{and } z_{1} < 2z_{1}^{t}} \\ & \text{or } z_{1}^{t-\Delta t} < 10^{-4} \\ & \text{else} \end{cases} \begin{cases} N^{t} = N^{t-\Delta t} + z_{n} \\ z_{1}^{t} = z_{n}^{t-\Delta t} < 10^{-4} \\ z_{1}^{t} = z_{1}^{t-\Delta t} + z_{n} \\ z_{1}^{t} = z_{n} \\ z_{1}^{t} = z_{n} \end{cases} \\ & \text{else} \end{cases} \begin{cases} N^{t} = N^{t-\Delta t} + 1 \\ & \text{fif } z_{1}^{t-\Delta t} < N_{\max} \\ z_{1}^{t} = z_{n} \\ z_{1}^{t} = z_{n}^{t-\Delta t} \forall i \in [2, N^{t}] \end{cases} \\ & \text{else} \end{cases} \begin{cases} N^{t} = N^{t-\Delta t} + 1 \\ & \text{else} \end{cases} \begin{cases} N^{t} = N^{t-\Delta t} + 1 \\ & \text{else} \end{cases} \\ & \text{else} \end{cases} \begin{cases} N^{t} = N^{t-\Delta t} + 1 \\ & \text{else} \end{cases} \end{cases} \\ & \text{else} \end{cases} \begin{cases} N^{t} = N^{t-\Delta t} + 1 \\ & \text{else} \end{cases} \begin{cases} N^{t} = N^{t-\Delta t} + 1 \\ & \text{else} \end{cases} \end{cases} \\ & \text{else} \end{cases} \begin{cases} N^{t} = N^{t-\Delta t} + 1 \\ & \text{else} \end{cases} \end{cases} \\ & \text{else} \end{cases} \begin{cases} N^{t} = N^{t-\Delta t} + 1 \\ & \text{else} \end{cases} \end{cases} \\ & \text{else} \end{cases} \begin{cases} N^{t} = N^{t-\Delta t} + 1 \\ & \text{else} \end{cases} \end{cases} \\ & \text{else} \end{cases} \begin{cases} N^{t} = N^{t-\Delta t} + 1 \\ & \text{else} \end{cases} \end{cases} \\ & \text{else} \end{cases} \begin{cases} N^{t} = N^{t-\Delta t} + 1 \\ & \text{else} \end{cases} \end{cases} \\ & \text{else} \end{cases} \begin{cases} N^{t} = N^{t-\Delta t} + 1 \\ & \text{else} \end{cases} \end{cases} \\ & \text{else} \end{cases} \begin{cases} N^{t} = N^{t-\Delta t} + 1 \\ & \text{else} \end{cases} \end{cases} \\ & \text{else} \end{cases} \begin{cases} N^{t} = N^{t-\Delta t} + 1 \\ & \text{else} \end{cases} \end{cases} \\ & \text{else} \end{cases} \begin{cases} N^{t} = N^{t-\Delta t} + 1 \\ & \text{else} \end{cases} \end{cases} \\ & \text{else} \end{cases} \begin{cases} N^{t} = N^{t-\Delta t} + 1 \\ & \text{else} \end{cases} \end{cases} \\ & \text{else} \end{cases} \begin{cases} N^{t} = N^{t-\Delta t} + 1 \\ & \text{else} \end{cases} \end{cases} \\ & \text{else} \end{cases} \begin{cases} N^{t} = N^{t-\Delta t} + 1 \\ & \text{else} \end{cases} \end{cases} \\ & \text{else} \end{cases} \begin{cases} N^{t} = N^{t-\Delta t} + 1 \\ & \text{else} \end{cases} \end{cases} \\ & \text{else} \end{cases} \begin{cases} N^{t} = N^{t-\Delta t} + 1 \\ & \text{else} \end{cases} \end{cases} \\ & \text{else} \end{cases} \begin{cases} N^{t} = N^{t-\Delta t} + 1 \\ & \text{else} \end{cases} \end{cases} \\ & \text{else} \end{cases} \begin{cases} N^{t} = N^{t-\Delta t} + 1 \\ & \text{else} \end{cases} \end{cases} \\ & \text{else} \end{cases} \begin{cases} N^{t} = N^{t-\Delta t} + 1 \\ & \text{else} \end{cases} \end{cases} \\ & \text{else} \end{cases} \begin{cases} N^{t} = N^{t-\Delta t} + 1 \\ & \text{else} \end{cases} \\ & \text{else} \end{cases} \begin{cases} N^{t} = N^{t-\Delta t} + 1 \\ & \text{else} \end{cases} \\ & \text{else} \end{cases} \begin{cases} N^{t} = N^{t-\Delta t} + 1 \\ & \text{else} \end{cases} \\ & \text{else} \end{cases} \end{cases} \\ & \text{else} \end{cases} \begin{cases} N^{t} = N^{t-\Delta t} + 1 \\ & \text{else} \end{cases} \\ & \text{else} \end{cases} \begin{cases} N^{t$$

In the definition of the initial number of layers (first line of Eq. 11),  $\lfloor . \rfloor$  designates the floor operator. The literal translation of Eq. 11 is as follows. A uniform layering is applied for new snowfall on the ground while the total snow depth does not reach  $Z_{\min}=0.03~\mathrm{m}$ . In other cases, snowfall is aggregated to the surface layer when it is similar to a sufficiently thin surface layer or when it is very low. When new snowfall is too thick or too different from the surface layer, a new layer is created, optionally after the aggregation of the two closest layers of the profile  $l_{\sup}$  and  $l_{\inf}$  (as defined by Equation 10), if  $N_{\max}$  is reached. When there is no snowfall, the algorithm applies only one of the following modification by order of priority: aggregation of surface layer or bottom layer when too thin, split of internal layer when too thick, aggregation of internal layer when too thin, relatively to the optimal attractor profile. Note than only one modification by point is allowed at each time step. Thus, when the conditions for an internal split or aggregation are obtained for several layers (i.e. several values of j) at the same time, it is only applied for the uppermost layer  $\min(j)$ . For glacier applications, aggregation is strictly forbidden between snow and





ice layers (i.e. when  $\rho_i < \rho_G$  and  $\rho_{i+1} > \rho_G$  where the threshold density for glacier  $\rho_G$  can be adjusted by the user (default  $850 \, \text{kg m}^{-3}$ ). 140

This algorithm is applied independently at each simulation point. Therefore, the vertical layering differs between points in terms of number and thickness of snow layers. This raises a number of vectorization issues in the management of loops which were the topic of recent investigations detailed in Appendix I.

#### 2.3.2 Aggregation of layers

When two layers i and i+1 are aggregated ( $z_i^t=z_i^{t-\Delta t}+z_{i+1}^{t-\Delta t}$  from Eq. 11) the state variables are modified in order to conserve mass and enthalpy. The optical diameter is updated in order to obtain a mass-weighted average of the corresponding albedo. A mass-weighted average is also applied for sphericity and age.

$$m_i^t = m_i^{t-\Delta t} + m_{i+1}^{t-\Delta t} \tag{12}$$

$$\rho_i^t = \frac{m_i^t}{z_i^t} \tag{13}$$

150 
$$H_i^t = H_i^{t-\Delta t} + H_{i+1}^{t-\Delta t}$$
 (14)

$$d_{i}^{t} = \left[ \frac{0.9 - \frac{m_{i}^{t-\Delta t} \left(0.9 - 15.4\sqrt{d_{i}^{t-\Delta t}}\right) + m_{i+1}^{t-\Delta t} \left(0.9 - 15.4\sqrt{d_{i+1}^{t-\Delta t}}\right)}{m_{i} + m_{i+1}}}{15.4} \right]^{2}$$

$$(15)$$

$$S_i^t = \frac{m_i^{t-\Delta t} S_i^{t-\Delta t} + m_{i+1}^{t-\Delta t} S_{i+1}^{t-\Delta t}}{m_i + m_{i+1}}$$
(16)

$$A_i^t = \frac{m_i^{t-\Delta t} A_i^{t-\Delta t} + m_{i+1}^{t-\Delta t} A_{i+1}^{t-\Delta t}}{m_i + m_{i+1}}$$

$$(17)$$

$$S_{i}^{t} = \frac{m_{i}^{t-\Delta t} S_{i}^{t-\Delta t} + m_{i+1}^{t-\Delta t} S_{i+1}^{t-\Delta t}}{m_{i} + m_{i+1}}$$

$$A_{i}^{t} = \frac{m_{i}^{t-\Delta t} A_{i}^{t-\Delta t} + m_{i+1}^{t-\Delta t} A_{i+1}^{t-\Delta t}}{m_{i} + m_{i+1}}$$

$$h_{i}^{t} = \begin{cases} h_{i}^{t-\Delta t} \text{ if } m_{i}^{t-\Delta t} \ge m_{i+1}^{t-\Delta t} \\ h_{i+1}^{t-\Delta t} \text{ otherwise} \end{cases}$$

$$(16)$$

155 
$$\mathcal{W}_{d,i}^t = \mathcal{W}_{d,i}^{t-\Delta t} + \mathcal{W}_{d,i+1}^{t-\Delta t}$$
 (19)

$$\mathcal{W}_{w,i}^t = \mathcal{W}_{w,i}^{t-\Delta t} + \mathcal{W}_{w,i+1}^{t-\Delta t} \tag{20}$$

The same equations apply to aggregate falling snow with the surface layer replacing  $x_i^t$ ,  $x_i^{t-\Delta t}$  and  $x_{i+1}^{t-\Delta t}$  by respectively  $x_1^t, x_1^{t-\Delta t}$  and  $x_n$  for each x representing all state variables  $m, \rho, H, d, S, A, h, \mathcal{W}_d$  and  $\mathcal{W}_w$  in Eq. 12-20.



165



# 2.3.3 Splitting of layers

When a layer i is splitted into two layers i and i+1 ( $z_i^t=z_{i+1}^t=\frac{z_i^{t-\Delta t}}{2}$  from Eq. 11), mass and enthalpy are divided into equal parts and microstructure properties are not modified:

$$m_i^t = m_{i+1}^t = \frac{m_i^{t-\Delta t}}{2} \tag{21}$$

$$\rho_i^t = \frac{m_i^t}{z_i^t} \tag{22}$$

$$H_i^t = H_{i+1}^t = \frac{H_i^{t-\Delta t}}{2} \tag{23}$$

 $d_i^t = d_{i+1}^t = d_i^{t-\Delta t}$ (24)

$$S_i^t = S_{i+1}^t = S_i^{t-\Delta t} (25)$$

$$A_i^t = A_{i+1}^t = A_i^{t-\Delta t} (26)$$

$$h_i^t = h_{i+1}^t = h_i^{t-\Delta t} (27)$$

$$\mathcal{W}_{d,i}^t = \mathcal{W}_{d,i+1}^t = \frac{\mathcal{W}_{w,i}^{t-\Delta t}}{2}$$

$$\mathcal{W}_{d,i}^t = \mathcal{W}_{d,i+1}^t = \frac{\mathcal{W}_{w,i}^{t-\Delta t}}{2}$$
(28)

170 
$$\mathcal{W}_{w,i}^t = \mathcal{W}_{w,i+1}^t = \frac{\mathcal{W}_{w,i}^{t-\Delta t}}{2}$$
 (29)

#### **Evolution equations**

#### Snowfall

The new snow amount is the result of solid precipitation, but also deposition of blowing snow and snowmaking, when the corresponding modules are activated. These three mass sources are respectively refered by the subscripts SP, BS and SM in the 175 following. In case of simultaneous occurrence, only one additional layer is created with weighted physical properties. Thus, the mass of the new layer is defined by:

$$m_n = m_{\rm SP} + m_{\rm BS} + m_{\rm SM} \tag{31}$$

The density of new snow  $\rho_n$ , optical diameter  $d_n$ , and sphericity  $S_n$  are expressed by:

180 
$$\rho_n = \frac{\rho_{\rm SP} m_{\rm SP} + \rho_{\rm BS} m_{\rm BS} + \rho_{\rm SM} m_{\rm SM}}{m_{\rm max}}$$
(32)

$$d_n = \frac{d_{\rm SP}m_{\rm SP} + d_{\rm SM}m_{\rm SM}}{m_n} \tag{33}$$

$$d_{n} = \frac{d_{\rm SP}m_{\rm SP} + d_{\rm BS}m_{\rm BS} + d_{\rm SM}m_{\rm SM}}{m_{n}}$$

$$S_{n} = \frac{S_{\rm SP}m_{\rm SP} + S_{\rm BS}m_{\rm BS} + S_{\rm SM}m_{\rm SM}}{m_{n}}$$
(34)

The mass of solid precipitation during the time step  $\Delta t$  is directly provided by the forcing:

$$m_{\rm SP} = \mathcal{P}_s \Delta t$$
 (35)



190



Several empirical expressions of the density of natural falling snow  $\rho_{\rm SP}$  are implemented (Vionnet et al., 2012; Schmucki et al., 2014; Anderson, 1976), as a function of 2-m air temperature  $T_a^*$  (°C) =  $T_a - T_0$  and 10-m wind speed  $U_{10}$  (m s<sup>-1</sup>). They can be activated through the SNOWFALL physical option following Equation 36. An illustration comparing these formulations is provided in Lafaysse et al. (2017), Figure 1 in the corrigendum. The parameters are listed in Appendix J3. When the forcing wind speed is not available at a 10 m height, a logarithmic adjustment is applied following Appendix B.

$$\begin{cases} \text{If SNOWFALL} = \text{V12:} & \rho_{\text{SP}} = \max(\rho_{\min}, a_{\rho} + b_{\rho} T_a^* + c_{\rho} \sqrt{U_{10}}) \\ \text{If SNOWFALL} = \text{S14:} & \begin{cases} \log_{10}(\rho_{\text{SP}}) = e_{\rho} + f_{\rho} T_a^* + g_{\rho} + h_{\rho} \sin^{-1}(\sqrt{i_{\rho}}) + j_{\rho} \log_{10}(\max[U_{10}, 2]) & \text{if } T_a^* \ge -14^{\circ}C \\ \log_{10}(\rho_{\text{SP}}) = e_{\rho} + f_{\rho} T_a^* + h_{\rho} \sin^{-1}(\sqrt{i_{\rho}}) + j_{\rho} \log_{10}(\max[U_{10}, 2]) & \text{otherwise} \end{cases}$$

$$\text{If SNOWFALL} = \text{A76:} & \rho_{\text{SP}} = \rho_{\min} + \max(k_{\rho} (T_a^* + l_{\rho})^{1.5}, 0)$$

$$(36)$$

Adjustments of parameter  $c_{\rho}$  were proposed by Woolley et al. (2024) to account for the uncertainties associated with the impact of wind speed on Arctic snowfall density. Although hard-coded in version 3.0, this parameter will be tunable in a future version.

Several formulations of microstructure properties of new snow were implemented by Vionnet et al. (2018) depending on SNOWDRIFT option. Again, Appendix B is used to assess the 5-m wind speed  $U_5$  from the forcing wind speed U at height  $z_u$ . SNOWDRIFT options are reformulated here with the new microstructure variables now used in the model:

$$\begin{cases} S_{\rm SP} = \min \left( \max \left( 0.0795U_5 + 0.38, 0.5 \right), 0.9 \right) \\ d_{\rm SP} = 10^{-4} \left( \delta_{\rm NONE} + \left( 1 - \delta_{\rm NONE} \right) (4 - S_{\rm SP}) \right) \\ \text{where } \delta_{\rm NONE} = \min \left( \max (1.29 - 0.173U_5, 0.2), 1 \right) \end{cases} \\ \begin{cases} S_{\rm SP} = 0.5 \\ d_{\rm SP} = 10^{-4} \end{cases} \\ \begin{cases} S_{\rm SP} = \min \left( \max \left( 0.035U_5 + 0.43, 0.5 \right), 0.9 \right) \\ d_{\rm SP} = 10^{-4} \left( \delta_{\rm VI13} + \left( 1 - \delta_{\rm VI13} \right) (4 - S_{\rm SP}) \right) \\ \text{where } \delta_{\rm VI13} = \min \left( \max \left( 1.14 - 0.07U_5, 0.2 \right), 1 \right) \end{cases} \\ \begin{cases} S_{\rm SP} = 1 - 0.49\delta_{\rm GA01} \\ d_{\rm SP} = 10^{-4} \left( \delta_{\rm GA01} + \left( 1 - \delta_{\rm GA01} \right) (4 - S_{\rm SP}) \right) \\ \text{where } \delta_{\rm GA01} = \min \left( \max \left( 2.868 \exp \left( -0.085U_5 \right) - 1, 0 \right), 1 \right) \end{cases} \end{cases}$$

VI13 refers to the approach of Vionnet et al. (2013) and GA01 refers to the approach of Gallée et al. (2001). The initial value of the historical tracker is  $h_n = 0$  and the initial value of snow age is  $A_n = 0$ . At each following time step, this variable



205

215

220



200 remembers the duration from the snowfall event by the simple evolution:

$$A_i^{t+\Delta t} = A_i^t + \frac{\Delta t}{86400} \tag{38}$$

# 2.4.2 Blowing snow

The mass, density, optical diameter and sphericity of blowing snow ( $m_{\rm BS}$ ,  $\rho_{\rm BS}$ ,  $d_{\rm BS}$ ,  $S_{\rm BS}$ ) can be provided by an external snow transport module. Within SURFEX, three different snow transport modules can be coupled to Crocus. The SYTRON module (Durand et al., 2001; Vionnet et al., 2018) is designed to simulate erosion and accumulation from the windward to the leeward side of the crests in French operational simulations based on an idealized topography. The SnowPappus module comprehensively described by Baron et al. (2024) is designed for gridded simulations at horizontal resolutions between 30 and 250 m (Haddjeri et al., 2024). Finally, snow transport can be solved by an explicit coupling with the MESO-NH Large Eddy Simulation model for process studies on small study domains and at the event scale (Vionnet et al., 2014, 2017).

#### 210 2.4.3 Machine-made snow

A representation of machine-made snow can optionally be provided by a dedicated module activated by the logical option SNOWMAK\_BOOL. This enables the model to compute the mass, density, optical diameter and sphericity of machine-made snow (snowmaking) ( $m_{\rm SM}$ ,  $\rho_{\rm SM}$ ,  $d_{\rm SM}$ ,  $S_{\rm SM}$ ) and its interaction with the rest of the snowpack. First, the wet bulb temperature  $T_w$  (expressed in K) is computed following Eq. F20 in Appendix F. The machine-made production is allowed if both the wet bulb temperature and the wind speed are lower than the respective user-defined thresholds  $T_{\rm lim}$  and  $U_{\rm lim}$ . When the meteorological conditions are satisfied, snowmaking is activated only during two periods over the winter season: the "base-layer generation" production period and the "reinforcement" production period (Spandre et al., 2016; Hanzer et al., 2020). The dates of beginning and end of each period and the times allowed in the day are defined by the user from parameters day 1 to day 3 and  $t_1$  to  $t_4$  described in Appendix J3. Two different strategies can be adopted depending on the SELF\_PROD logical option. When it is set to True, the production follows a pre-defined set of rules. In this case, during the base-layer generation period the production is allowed until a given amount of water  $p_{\rm lim}$  (kg m<sup>-2</sup>) is used. During the reinforcement period, instead, the production is allowed if the total snow depth Z is lower than a threshold  $Z_{\rm lim}$ . If SELF\_PROD is False, the production is forced to match a water use target (kg m<sup>-2</sup>) defined by the user for each simulated point, regardless of any meteorological or timing condition.

The mass of machine-made snow is then obtained by:

225 
$$m_{\rm SM} = (1 - \mathcal{L}_{\rm SM}) \frac{\mathcal{I}_{\rm SM}}{\mathcal{A}_{\rm SM}} \left( a_{\rm SM} (T_w - T_0) + b_{\rm SM} \right) \Delta t$$
 (39)

where  $\mathcal{I}_{\rm SM}=1$  when production is allowed, and 0 otherwise,  $\mathcal{A}_{\rm SM}$  is the surface area covered by a snow gun set to 3300 m<sup>2</sup>, and  $\mathcal{L}_{\rm SM}$  the loss factor set to 0.4 by Spandre et al. (2016).  $a_{\rm SM}$  (kg K<sup>-1</sup> s<sup>-1</sup>) and  $b_{\rm SM}$  (kg s<sup>-1</sup>) are regression coefficients of the parameterization of the potential mass produced by a snowgun. They can be adjusted by the user or derivated from Olefs et al. (2010).

The density  $\rho_{\rm SM}$  of machine-made snow can be adjusted by the user whereas the snow microstructure properties  $d_{\rm SM}$  and  $S_{\rm SM}$  are fixed following Spandre et al. (2016).



245



For more information about the implementation of the snowmaking practices in Crocus, please refer to Spandre et al. (2016) and Hanzer et al. (2020).

#### 2.4.4 Freezing rain

When liquid precipitation occurs at negative temperatures, the model can simulate the formation of an ice layer at the top of the surface following the work of Quéno et al. (2018). In a first step, the whole precipitation mass is assumed to form a new ice layer at  $T_0$ , only aggregated to the previous surface layer if a thin ice layer is already present (Eq. 40)

$$\begin{cases} m_n = \mathcal{P}_r \Delta t \\ \rho_n = \rho_I \\ H_n = -L_m \mathcal{P}_r \Delta t \\ A_n = 0 \\ d_n = 2 \times 10^{-3} \mathrm{m} \\ S_n = 1 \\ h_n = 2 \end{cases}$$
 (40) If  $(D(n,1) < 20$  and  $z_1^- < 0.01$ ) or  $N^- = N_{\mathrm{max}}$ : 
$$\begin{cases} N^+ = N^- \\ \mathrm{Eq.} \ 12 - 20 \ \mathrm{applied} \ \mathrm{to} \ (x_n, x_1^-) \\ \forall x \in [m, \rho, H, A, d, S, h] \\ x_1^+ = x_n \forall x \in [m, \rho, H, A, d, S, h] \ \mathrm{and} \ \forall i \in [2, N^+] \end{cases}$$
 The energy associated with the phase change  $E_{\mathrm{FRZ}}(\mathrm{W} \, \mathrm{m}^{-2})$  is computed by Eq. 41 and accounted for further as an additional

The energy associated with the phase change  $E_{FRZ}$  (W m<sup>-2</sup>) is computed by Eq. 41 and accounted for further as an additional energy source in the surface energy balance (Eq. 93), able to partly melt this new ice layer:

$$\begin{cases} \text{If } \mathcal{P}_r > 0 \text{ and } T_a < T_0: \quad E_{\text{FRZ}} = (1 - \phi_{\text{FRZ}}) L_m \mathcal{P}_r \Delta t \text{ where } \phi_{\text{FRZ}} = \frac{c_W}{L_m} (T_0 - T_a) \\ \text{else}: \qquad \qquad E_{\text{FRZ}} = 0 \end{cases}$$
(41)

The assumption behind Eq.41 is that a fraction  $\phi_{FRZ}$  of the latent heat release due to refreezing is consumed by the increase of temperature from  $T_a$  to  $T_0$  and the remaining part is fully stored by the surface layer and can either be available for melting either be partly dissipated through diffusion or heat exchanges with the atmosphere, as solved later in Sections 2.4.12 and 2.4.13.





Note that some other implementations of this process in other models consider than while all the precipitation eventually freezes and contributes to the formation of an ice layer at the surface, only a fraction of the associated latent heat is kept in the ice layer, while the remaining latent heat is transferred to the atmosphere at a shorter time scale than the model time step (Lackmann et al., 2002; Basnet and Thériault, 2025).

#### 250 Metamorphism

260

The prognostic equations of microstructure variables  $d_i$  and  $S_i$  are still fully empirical in the absence of physical evolution laws. They depend on conditions on the vertical temperature gradient  $G_i$  estimated by:

$$\begin{cases}
\mathcal{G}_{1} = \frac{2|T_{2} - T_{1}|}{z_{1} + z_{2}} \\
\mathcal{G}_{i} = \frac{2|T_{i+1} - T_{i-1}|}{z_{i-1} + 2z_{i} + z_{i+1}} \forall i \in [2, N - 1] \\
\mathcal{G}_{N} = \frac{2|T_{N} - T_{N-1}|}{z_{N-1} + z_{N}}
\end{cases} (42)$$

Following Brun et al. (1992) and Vionnet et al. (2012), the evolution of sphericity  $\Delta S_i$  during a time step  $\Delta_t$  is defined by 255 Eq. 43 (dry metamorphism) and 44 (wet metamorphism):

$$\text{If } l_i = 0: \begin{cases} \text{If } \mathcal{G}_i < 5 \, \text{K m}^{-1} & \begin{cases} \text{If } S_i < 1 & \Delta S_i = \text{sph}_1 e^{-6000/T_i} f_{\text{corr}}(d_i, S_i, h_i) \Delta t \\ \text{else} & \Delta S_i = 0 \end{cases} \\ \text{If } S_i > 0 & \Delta S_i = -\text{sph}_2 e^{-6000/T_i} \mathcal{G}_i^{0.4} \Delta t \\ \text{else} & \Delta S_i = 0 \end{cases}$$

$$\text{If } l_i > 0: \begin{cases} \text{If } S_i < 1: \quad \Delta S_i = \max \left( \text{sph}_3 \left( 100 \frac{l_i}{\rho_i z_i} \right)^3, \text{sph}_2 e^{-6000/T_0} \right) \Delta t \\ \text{If } S_i = 1: \quad \Delta S_i = 0 \end{cases}$$

$$(43)$$

If 
$$l_i > 0$$
: 
$$\begin{cases} \text{If } S_i < 1: \quad \Delta S_i = \max\left(\text{sph}_3\left(100\frac{l_i}{\rho_i z_i}\right)^3, \text{sph}_2 e^{-6000/T_0}\right) \Delta t \\ \text{If } S_i = 1: \quad \Delta S_i = 0 \end{cases}$$
(44)

Parameters  $sph_1$ ,  $sph_2$  and  $sph_3$  are provided in Appendix J3.  $f_{corr}(d_i, S_i, h_i)$  is an unpublished parameterization in the original code of Vionnet et al. (2012) which modifies the general behaviour of Eq. 43 by reducing the sphericity increase of depth hoar or large faceted crystals submitted to low thermal gradients. This prevents the formation of rounded grains from depth hoar or large faceted crystals. Indeed, the persistence of anisotropy in this case was obtained with a phase-field numerical model applied to snow microstructure (Bouvet et al., 2022) and recently confirmed by unpublished tomography observations.

$$\begin{cases} \text{If } S_i \ge 0.5 \ ; \ h_i = 1 \ \text{and} \ g_{s_i}(d_i, S_i) > 5 \times 10^{-4} \text{m} & f_{\text{corr}}(d_i, S_i, h_i) = 0 \\ \text{If } S_i < 0.5 \ ; \ h_i = 1 \ \text{and} \ g_{s_i}(d_i, S_i) > 5 \times 10^{-4} \text{m} & f_{\text{corr}}(d_i, S_i, h_i) = \exp(\frac{3 \times 10^{-4} - g_{s_i}(d_i, S_i)}{10^{-4}}) \\ \text{otherwise} & f_{\text{corr}}(d_i, S_i, h_i) = 1 \end{cases}$$

$$(45)$$

 $h_i$  is a tracker of the snow layer history (Table 1) for which the 1 value corresponds to the occurrence of depth hoar at any time since the layer creation.  $g_{s_i}(d_i, S_i)$  is a variable originally used to describe snow microstructure by Brun et al. (1992)



285



(grain size). Its retrieval from the current state variables  $d_i$  and  $S_i$  is described in Appendix D. It must be noticed that this parameterization was forgotten by Carmagnola et al. (2014) because it was unpublished and was only recently restored in the code.

Several prognostic evolutions of  $d_i$  during dry metamorphism were implemented by Carmagnola et al. (2014) and Lafaysse et al. (2017), following the works from Brun et al. (1992), Flanner and Zender (2006) and Schleef et al. (2014). Furthermore, several issues were found by Baron (2023) in the translation of the Brun et al. (1992) formalism (using dendricity and grain size) in terms of optical diameter evolution by Carmagnola et al. (2014) (details in Appendix D). A new parameterization (B21) was therefore recently implemented to solve the associated issues and now replaces the original implementation of Carmagnola et al. (2014) now removed from the code. The resulting available evolution laws of  $d_i$  during dry metamorphism are given by Eq. 46-49. 275

$$\begin{bmatrix} \text{If SNOWMETAMO=B21} \\ \text{and } l_i = 0 : \end{bmatrix} \begin{cases} \text{If } d_i \geq 10^{-4} (4 - S_i) : \begin{cases} \text{If } \mathcal{G}_i > 15 \, \text{K m}^{-1} \text{ and } S_i = 0 : & \Delta d_i = \frac{1}{2} f(\theta_i) h(\rho_i) g(\mathcal{G}_i) \Phi \Delta t \\ \text{else:} & \Delta d_i = \frac{d_i - 4 \times 10^{-4}}{1 + S_i} \Delta S_i \end{cases} \\ \text{else:} & \Delta d_i = 10^{-4} \left[ -\text{sph}_2 e^{-6000/T_i} \mathcal{J}_i (S_i - 3) + \frac{\Delta S_i}{\Delta t} \frac{10^4 d_i - 1}{S_i - 3} \right] \Delta t \\ \text{where } \begin{cases} \mathcal{J}_i = \mathcal{G}_i^{0.4} & \text{if } \mathcal{G}_i \geq 5 \\ \mathcal{J}_i = 1 & \text{if } \mathcal{G}_i < 5 \end{cases} \end{cases}$$

$$\begin{bmatrix} \text{If SNOWMETAMO=F06} \\ \text{and } l_i = 0 : \end{bmatrix} \Delta d_i = 2\dot{r}_0(\rho_i, T_i, \mathcal{G}_i) \left[ \frac{\tau(\rho_i, T_i, \mathcal{G}_i)}{\frac{d_i}{2} - r_0 + \tau(\rho_i, T_i, \mathcal{G}_i)} \right]^{\frac{1}{\kappa(\rho_i, T_i, \mathcal{G}_i)}} \Delta t$$

$$\begin{bmatrix} \text{If SNOWMETAMO=S-B} \\ \text{and } l_i = 0 : \end{bmatrix} \begin{cases} \text{If } A_i \leq 2 \, \text{days} \quad \Delta d_i = \frac{a_s \rho_i d_i^2}{6} + \frac{b_s T_i \left(\frac{\theta}{\rho_i}\right)^{m_s - 1}}{d_i^{m_s - 2}} \\ \text{else:} \qquad \text{Equation 46} \end{cases}$$

$$\begin{bmatrix} \text{If SNOWMETAMO=S-F} \end{bmatrix} \begin{cases} \text{If } A_i \leq 2 \, \text{days} \quad \text{Equation 48} \end{cases}$$

$$\begin{bmatrix} \text{If SNOWMETAMO=F06} \\ \text{and } l_i = 0 : \end{bmatrix} \Delta d_i = 2\dot{r}_0(\rho_i, T_i, \mathcal{G}_i) \begin{bmatrix} \tau(\rho_i, T_i, \mathcal{G}_i) \\ \frac{d_i}{2} - r_0 + \tau(\rho_i, T_i, \mathcal{G}_i) \end{bmatrix}^{\frac{1}{\kappa(\rho_i, T_i, \mathcal{G}_i)}} \Delta t \tag{47}$$

$$\begin{bmatrix} \text{If SNOWMETAMO=S-B} \\ \text{and } l_i = 0 : \end{bmatrix} \begin{cases} \text{If } A_i \leq 2 \text{ days} \quad \Delta d_i = \frac{a_s \rho_i d_i^2}{6} + \frac{b_s T_i \left(\frac{6}{\rho_i}\right)^{m_s - 1}}{d_i^{m_s - 2}} \\ \text{else:} \qquad \qquad \text{Equation 46} \end{cases}$$

$$(48)$$

$$\begin{bmatrix} \text{If SNOWMETAMO=S-F} \\ \text{and } l_i = 0 : \end{bmatrix} \begin{cases} \text{If } A_i \leq 2 \text{ days} & \text{Equation 48} \\ \text{else:} & \text{Equation 47} \end{cases}$$

$$(49)$$

280 (50)

Functions  $f(\theta_i)$ ,  $h(\rho_i)$ ,  $g(\mathcal{G}_i)$  and parameter  $\Phi$  used in Eq. 46 for the growth of faceted crystals in the case of high gradient metamorphism follow Marbouty (1980) and are defined in Appendix C. In Eq. 47 from Flanner and Zender (2006), coefficients  $\dot{r}_0(\rho_i, T_i, \mathcal{G}_i), \tau(\rho_i, T_i, \mathcal{G}_i)$  and  $\kappa(\rho_i, T_i, \mathcal{G}_i)$  are retrieved from look-up tables provided in a parameters file (cf. section on Data and Code availability) and  $r_o = 5 \times 10^{-5}$  m. Experimental parameters  $a_s$ ,  $b_s$ ,  $m_s$  in Eq. 49 are defined in Appendix J3 from Schleef et al. (2014).

Regardless of the SNOWMETAMO option, wet metamorphism is always parameterized with the laws published by Vionnet et al. (2012), rewritten here with the new microstructure prognostic variables and the methodology described in Appendix D:





$$\text{If } l_{i} > 0 \begin{cases} \text{If } d_{i} < 10^{-4} (4 - S_{i}) : \begin{cases} \text{If } S_{i} < 1 : \Delta d_{i} = 10^{-4} \left( \frac{10^{4} d_{i} - 1}{S_{i} - 3} - (S_{i} - 3) \right) \Delta S_{i} \\ \text{If } S_{i} = 1 : \Delta d_{i} = 2.10^{-4} \max \left( \text{sph}_{3} \left( 100 \frac{l_{i}}{\rho_{i} z_{i}} \right)^{3}, \text{sph}_{2} e^{-6000/T_{0}} \right) \Delta t \end{cases}$$

$$\text{else : } \begin{cases} \text{If } S_{i} < 1 : \Delta d_{i} = \frac{d_{i} - 4.10^{-4}}{S_{i} + 1} \Delta S_{i} \\ \text{If } S_{i} = 1 : \Delta d_{i} = \frac{2}{\pi} \frac{\left[ v_{0} + v_{1} \left( 100 \frac{l_{i}}{\rho_{i} z_{i}} \right)^{3} \right]}{d_{i}^{2}} \Delta t \end{cases}$$

$$(51)$$

To follow its definition in Table 1, the historical tracker  $h_i$  is updated at the end of this subroutine by:

$$\begin{cases} \text{If } S_{i} = 0 \text{ and } h_{i}^{t} = 0 : h_{i}^{t+\Delta t} = 1 \\ \\ \text{If } S_{i} = 1 \text{ and } \frac{l_{i}}{\rho_{i}z_{i}} > 0.005 : \begin{cases} \text{If } h_{i}^{t} = 0 : h_{i}^{t+\Delta t} = 2 \\ \text{If } h_{i}^{t} = 1 : h_{i}^{t+\Delta t} = 3 \\ \text{else } : h_{i}^{t+\Delta t} = h_{i}^{t} \end{cases} \\ \text{else } : \begin{cases} \text{If } I_{i}^{t} = 2 : h_{i}^{t+\Delta t} = 4 \\ \text{If } I_{i}^{t} = 2 : h_{i}^{t+\Delta t} = 4 \end{cases} \\ \text{If } h_{i}^{t} = 3 : h_{i}^{t+\Delta t} = 5 \\ \text{else } : h_{i}^{t+\Delta t} = h_{i}^{t} \end{cases} \\ \text{else } : h_{i}^{t+\Delta t} = h_{i}^{t} \end{cases}$$

#### 2.4.6 Natural compaction

For a given layer of density  $\rho_i$  the mechanical settling under the over burden  $\sigma_i$  (Pa) is expressed with a visco-elastic model (Anderson, 1976; Navarre, 1975):

If SNOWCOMP 
$$\in$$
 [B92, T11] :  $\Delta \rho_i = \frac{\rho_i \sigma_i}{\eta_i} \Delta t$  (53)

295

$$\begin{cases}
\sigma_i = g \cos \gamma \sum_{j=1}^{i-1} \rho_j z_j \forall i \in [2, N] \\
\sigma_1 = g \cos \gamma \times 0.5 \rho_1 z_1
\end{cases}$$
(54)

g is the gravitational acceleration and  $\gamma$  the slope angle from horizontal.

The viscosity  $\eta_i$  is a function of density  $\rho_i$  and temperature  $\theta_i$  (°C) depending on the SNOWCOMP option (Lafaysse et al., 2017; Teufelsbauer, 2011):

300 
$$\begin{cases} \text{If SNOWCOMP = B92:} & \eta_i = f_1(w_i) f_2(d_i, S_i) \eta_0 \frac{\rho_i}{c_\eta} e^{a_\eta(-\theta_i) + b_\eta \rho_i} \\ \text{If SNOWCOMP = T11:} & \eta_i = f_1(w_i) f_2(d_i, S_i) * 0.05 \rho_i^{-0.0371\theta_i + 4.4} (10^{-4} e^{0.018\rho_i} + 1) \end{cases}$$
 (55)





The parameters for case B92 are defined in Appendix J3. The multiplicative function  $f_1$  accelerates the settlement of wet snow as a function of the volumetric liquid water content  $w_i$ . The multiplicative function  $f_2$  reduces the settlement of layers consisting of faceted snow types as a function of microstructure properties  $d_i$  and  $S_i$  (translation of the formula from Vionnet et al. (2012) in the new formalism).

$$f_1(w_i) = \frac{1}{1 + 60\frac{w_i}{\rho_{in}}} \tag{56}$$

$$f_2(d_i, S_i) = \begin{cases} \min\left(4, \exp\left(\min\left(4, g_{s_i}(d_i, S_i) \times 10^4 - 2\right)\right)\right) & \text{if } d_i > (4 - S_i) \times 10^{-4} \text{ and } S_i \le 0.5\\ 1 & \text{otherwise} \end{cases}$$
(57)

where  $g_{s_i}(d_i, S_i)$  is defined by Eq. D6. The compaction rate however has a complex dependence to snow microstructure (Lehning et al., 2002) which cannot be described by the representation of snow microstructure in Crocus. Alternatively to equation 53, it is possible to use a parameterization from Schleef et al. (2014) derived from tomographic observations and representing a non-linear relationship between settlement, the stress  $\sigma_i$  (Pa) and the optical diameter increase for the first 48 hours after snowfall:

If SNOWCOMP = S14: 
$$\begin{cases} \Delta \rho_i = B_S \frac{\Delta d_i}{d_i^2} \sigma_i^{k_S} & \text{if } A_i \le 2 \text{ days} \\ \text{Equation 53} & \text{if } A_i > 2 \text{ days} \end{cases}$$
(58)

with  $B_S = 3.96 \times 10^{-2}$  and  $k_S = 0.18$ . The current Crocus parameterization is applied when the snow layer age exceeds 2 days.

Alternative parameterizations reducing compaction in the presence of low vegetation were proposed by Woolley et al. (2024) combining earlier works from Domine et al. (2016) and Royer et al. (2021). Although not available in version 3.0, they will be implemented in a future version.

# 2.4.7 Grooming

310

325

The effects of grooming machines (snowcats) on the snow physical properties include the compaction induced by their overburden weight and the mixing of surface layers produced by the tiller. Both these effects can optionally be simulated in Crocus (Spandre et al., 2016).

The compaction effect is activated using the logical switch SNOWCOMPACT and only applies if the total mass  $M = \sum_{i=1}^{N} m_i$  is higher than  $20 \text{ kg m}^{-2}$  (a minimum value required by the grooming machines) and between 8pm and 9pm (and also 6am-9am in case of snowfall during the night). Grooming starts on November 1st and continues until the date day<sub>END</sub> chosen by the user. Its frequency  $f_{\text{GRO}}$  (number of grooming sessions per day) is also user-defined. It is worth noticing that it is possible to activate grooming without activating snowmaking, but the opposite would not be realistic. The static stress due to the weight of the snowcat itself  $\sigma_{\text{GRO}_i}$  (Pa) is expressed for layer i by:





$$\text{If SNOWCOMPACT} \begin{cases} \text{If} \quad \sum_{j=1}^{i} m_{j} < 50 \text{ kg m}^{-2} : \sigma_{\text{GRO}_{i}} = g \cos \gamma \times 500 \\ \text{If} \quad 50 \text{ kg m}^{-2} \le \sum_{j=1}^{i} m_{j} < 150 \text{ kg m}^{-2} : \sigma_{\text{GRO}_{i}} = g \cos \gamma \times (150 - \sum_{j=1}^{i} m_{j}) * 5 \\ \text{If} \quad \sum_{j=1}^{i} m_{j} \ge 150 \text{ kg m}^{-2} : \sigma_{\text{GRO}_{i}} = 0 \end{cases}$$
 (59)

and the corresponding density change is obtained by replacing  $\sigma_i$  by  $\sigma_{\text{GRO}_i}$  in Eq. 53.

330 The tilling effect is activated using the logical switch SNOWTILLER, applies down to 35 kg m<sup>-2</sup> below the surface and only if SNOWCOMPACT = True. The tiller mounted at the rear of snowcats produces two main effects: it further increases the density of the snow by loading the snowpack with extra pressure and it modifies the snow microstructure by creating smaller, rounded grains. As a result, all impacted layers are mixed together, their properties are homogenized and some of them are modified (Spandre et al., 2016). These effects are simulated in Crocus by directly modifying the density, optical diameter and sphericity of the impacted layers. The density reached by the snowpack after grooming is parameterized as:

If SNOWTILLER: 
$$\rho_i = \max\left(\overline{\rho}, \frac{2\overline{\rho} + 3\rho_{\text{GRO}}}{5}\right) \forall i \in [1, k] | \sum_{i=1}^k m_i <= 35 \text{kg m}^{-2}$$
 (60)

where  $\bar{\rho} = \frac{\sum_{i=1}^k \rho_i m_i}{\sum_{i=1}^k m_i}$  is the weighted average density of the k impacted layers and  $\rho_{\rm GRO}$  is the target density that should eventually be reached by the grooming process (Spandre et al., 2016; Hanzer et al., 2020). The optical diameter and sphericity of snow are altered analogously, using the respective target values  $d_{\rm GRO}$  and  $S_{\rm GRO}$  (Appendix J3, Spandre et al., 2016; Hanzer et al., 2020).

#### 2.4.8 Drifting snow

345

Even if the Crocus model is not coupled with a dedicated module able to transport snow from one simulation point to another, it is possible to activate a parameterization from Vionnet et al. (2012) simulating the impact of drifting snow on compaction and metamorphism, but with mass conservation. This parameterization relies on two possible definitions of a mobility indice MOB<sub>i</sub> (Guyomarc'h and Merindol, 1998; Vionnet et al., 2012):

$$\begin{cases} \text{If SNOWMOB=GM98} \\ \text{If SNOWMOB=VI12} \end{cases} \begin{cases} \text{If } d_i < 10^{-4}(4-S_i): & \text{MOB}_i = 0.5(1-S_i) + 0.75\delta_i \\ \text{else:} & \text{MOB}_i = 0.833(1-S_i) - 0.583g_{s_i} \\ \text{If } d_i < 10^{-4}(4-S_i): & \text{MOB}_i = 0.34 \times (0.5(1-S_i) + 0.75\delta_i) + 0.66F(\rho_i) \\ \text{else:} & \text{MOB}_i = 0.34 \times (0.833(1-S_i) - 0.583g_{s_i}) + 0.66F(\rho_i) \end{cases}$$

where 
$$F(\rho) = [1.25 - 0.0042 \,(\text{max}(\rho_{\text{min}}, \rho) - \rho_{\text{min}})]$$
 and  $\rho_{\text{min}} = 50 \,\text{kg m}^{-3}$ . (62)





In addition, a threshold is applied on the mobility indice in case of melt forms:

If 
$$h_i >= 2$$
: MOB<sub>i</sub> = min(-0.0583, MOB<sub>i</sub> from Eq.61) (63)

The mobility indice was expressed with the original formalism of metamorphism. The conversion functions  $\delta_i(d_i, S_i)$  and  $g_{s_i}(d_i, S_i)$  are defined in Appendix D by Eq. D2 and D6. Redefining this indice as a function of the current state variables  $(d_i$  and  $S_i)$  would be more consistent and flexible but it would require a significant new effort of evaluation. It highlights the issues involved by changes in the variable states in a model which have been underestimated in the work of Carmagnola et al. (2014).

A driftability indice  $\mathcal{D}_i$  is then obtained by combining the mobility indice and the 5 m wind speed  $U_5$ :

355 
$$\mathcal{D}_i = \max(\text{MOB}_i - (2.868 * \exp(-0.085 \times U_5) - 1.), 0)$$
 (64)

We then introduce:

365

370

$$\mathcal{D}_{\text{EFF}_i} = \mathcal{D}_i \times \exp\left(-10 \times \left(\sum_{j=1}^{i-1} z_j (3.25 - \mathcal{D}_j) + \frac{z_i}{2} (3.25 - \mathcal{D}_i)\right)\right)$$

$$(65)$$

to formulate the variation of density due to snow drift by:

$$\Delta \rho_i = \mathcal{D}_{\text{EFF}_i} \max \left( \rho_{\text{MAX}} - \rho_i, 0 \right) \frac{\Delta t}{\tau_{\text{DRIFT}}}$$
(66)

with  $\rho_{\rm MAX}=350~{\rm kg~m^{-3}}$  and  $\tau_{\rm DRIFT}=172800~{\rm s}$  (2 days). Adjustments of parameters  $\rho_{\rm MAX}$  and  $\tau_{\rm DRIFT}$  were proposed by several authors for Arctic snow as summarized by Woolley et al. (2024). Although hard-coded in version 3.0, they will be adjustable by the user in a future version. Then, the variation of microstructure properties due to fragmentation during snow transport are obtained by Eq. 67. The origin of this expression is provided in Appendix E.

$$\begin{cases}
\text{If } d_i < 10^{-4}(4 - S_i) : \quad \Delta d_i = \mathcal{D}_{\text{EFF}_i} \times 10^{-4} \left[ (2.5 - 1.5S_i)\delta_i - 1 + S_i \right] \frac{\Delta t}{\tau_{\text{DRIFT}}} \\
\text{else} \qquad \qquad \Delta d_i = \mathcal{D}_{\text{EFF}_i} \left( -5 \times 10^{-4} \frac{1 + S_i}{2} + (d_i - 4 \times 10^{-4}) \frac{1 - S_i}{1 + S_i} \right) \frac{\Delta t}{\tau_{\text{DRIFT}}}
\end{cases}$$
(67)

$$\Delta S_i = \mathcal{D}_{\text{EFF}_i} (1 - S_i) \frac{\Delta t}{\tau_{\text{DRIFT}}}$$
(68)

Optionally, a mass loss due to blowing snow sublimation can be estimated and removed from the surface layer. The parameterization is inspired from Gordon et al. (2006) with a modification of a threshold wind speed  $U_t$  to account for the microstructure-related mobility indice. This option is not activated by default due to the large associated uncertainties and lack of evaluation but is considered to be necessary in polar environments (Brun et al., 2013; Woolley et al., 2024). The mass reduction of the surface layer due to sublimation  $\Delta m_1$  is obtained by:

$$\Delta m_1 = \min\left(0.5m_1, a_{\text{SUBL}}\left(\frac{T_0}{T_a}\right)^{\gamma_{\text{SUBL}}} U_t \rho_a q_{sat}(T_a) \left(1 - \frac{q_a}{q_{sat}(T_a)}\right) \left(\frac{U_5}{U_t}\right)^{b_{\text{SUBL}}} \Delta t\right) \text{ where } U_t = \frac{-\log(\frac{\text{MOB}_1 + 1}{c_{\text{SUBL}}})}{d_{\text{SUBL}}}$$
(69)



390

395



The air volumetric mass  $\rho_a$  (kg m<sup>-3</sup>) and the saturation specific humidity  $q_{sat}(T_a)$  (kg kg<sup>-1</sup>) are computed following Appendix F.  $a_{\text{SUBL}}$ ,  $b_{\text{SUBL}}$ ,  $c_{\text{SUBL}}$ ,  $c_{\text{SUBL}}$ ,  $d_{\text{SUBL}}$  are dimensionless parameters defined in Appendix J3

#### 375 **Absorption of solar radiation**

Two schemes of different complexities are currently implemented and can be activated through the SNOWRAD option. When SNOWRAD=B92, the initial 3-band scheme of Brun et al. (1992) is applied, inspired from Warren (1982). The incoming solar radiation at the interface between layers i and i + 1 is defined by:

$$R_{i} = \sum_{k=1}^{3} (1 - \alpha_{k}) \gamma_{k} SW \downarrow \exp\left(-\sum_{j=1}^{i} \beta_{k_{j}} z_{j}\right) \forall i \in [0, N] \quad \text{if SNOWRAD=B92}$$

$$(70)$$

The spectral partitioning of incoming radiation is fixed by parameters  $\gamma_k$  (Appendix J3, with  $\sum_{k=1}^{3} \gamma_k = 1$ ). 380

Spectral albedo values  $\alpha_k$  are parameterized by:

$$\alpha_k = \chi \alpha_{k_1} + (1 - \chi)\alpha_{k_2} \forall k \in [1, 3] \tag{71}$$

where 
$$\chi = 0.8 \min\left(1, \frac{z_1}{0.02}\right) + 0.2 \min\left[1, \max\left(0, \frac{z_1 - 0.02}{0.01}\right)\right]$$
 (72)

385 
$$\begin{cases} \alpha_{1_{i}} &= \max \left[ 0.6, \min \left( 0.92, 0.96 - 1.58\sqrt{d_{i}} \right) - 0.2 \frac{A_{i}}{\tau_{a}} \times \min \left( \max \left( 0.5, \frac{P_{s}}{P_{\text{CDP}}} \right), 1.5 \right) \right] \text{ if } \rho_{i} < \rho_{G} \\ \alpha_{1_{i}} &= \alpha_{1_{G}} \text{ if } \rho_{i} \ge \rho_{G} \end{cases}$$

$$\begin{cases} \alpha_{2_{i}} &= \max \left( 0.3, 0.9 - 15.4\sqrt{d_{i}} \right) \text{ if } \rho_{i} < \rho_{G} \\ \alpha_{2_{i}} &= \alpha_{2_{G}} \text{ if } \rho_{i} \ge \rho_{G} \end{cases}$$

$$\begin{cases} \alpha_{2_{i}} &= \alpha_{2_{G}} \text{ if } \rho_{i} \ge \rho_{G} \end{cases}$$

$$\begin{cases} \alpha_{2_{i}} &= 346.3d_{i}^{i} - 32.31\sqrt{d_{i}^{i}} + 0.88 \text{ if } \rho_{i} < \rho_{G} \text{ where } d_{i}^{i} = \min (d_{i}, 0.0023) \end{cases}$$

$$(74)$$

$$\begin{cases}
\alpha_{2_i} = \max\left(0.3, 0.9 - 15.4\sqrt{d_i}\right) \text{ if } \rho_i < \rho_G \\
\alpha_{2_i} = \alpha_{2_G} \text{ if } \rho_i \ge \rho_G
\end{cases}$$
for  $i \in [1, 2]$ 

$$(74)$$

$$\begin{cases} \alpha_{3_{i}} = 346.3d'_{i} - 32.31\sqrt{d'_{i}} + 0.88 \text{ if } \rho_{i} < \rho_{G} & \text{where} \quad d'_{i} = \min(d_{i}, 0.0023) \\ \alpha_{3_{i}} = \alpha_{3_{G}} \text{ if } \rho_{i} \ge \rho_{G} \end{cases}$$
 for  $i \in [1, 2]$  (75)

Note that compared to Vionnet et al. (2012), the consideration of optical diameters of the first two layers, already in the code but not documented, is now made explicit in Eq. 71. The time constant  $\tau_a$  in Eq. 73 is the main control of the parameterization reducing snow albedo in the visible band as a function of the age of the layer  $A_i$  in order to mimic the effect of Light-Absorbing Particles (LAP). Its default value is set to 60 days with an elevation-dependent multiplicative correction factor (function of P<sub>s</sub>) assuming that LAP deposition decreases with elevation. However, it is recommended to adjust this parameter depending on the expected amount of LAP in the target region (Gaillard et al., 2025), to consider calibration against observed albedo time series when possible, or to apply several values of this parameter in multiphysics applications (Lafaysse et al., 2017). Last modification, constant glacier spectral albedo values  $\alpha_{k_G}$  on snow-free glacier surfaces. Default values (Appendix J5) are taken from Lejeune (2009) but must be adjusted to each specific glacier (e.g. Réveillet et al., 2018)



405

420



Absorption coefficients  $\beta_{k_i}$  (m<sup>-1</sup>) for band k and layer i are parameterized by:

$$\beta_{1_i} = \max\left(40, 0.00192 \frac{\rho_i}{\sqrt{d_i}}\right) \forall i \in [1, N]$$
(76)

$$\beta_{2_i} = \max\left(100, 0.01098 \frac{\rho_i}{\sqrt{d_i}}\right) \forall i \in [1, N]$$
(77)

$$400 \quad \beta_{3_1} = +\infty \tag{78}$$

Alternatively to Eq. 70, an option is available for solar radiative transfer calculation in the snowpack (SNOWRAD=T17) combining the TARTES radiative scheme (Two-streAm Radiative TransfEr in Snow model, Picard and Libois, 2024) and an explicit modelling of LAP (Tuzet et al., 2017). TARTES is a two-stream radiative transfer scheme based on an analytical formulation of radiative transfer in snow (Kokhanovsky and Zege, 2004). The scheme is applied separately for the direct (DIR) and diffuse (DIF) components of solar radiation. For both components, TARTES computes spectral solar absorption within each layer  $E_{k_i}$  (Eq. 59-63 in the comprehensive scientific documentation of TARTES, Picard and Libois, 2024) and the spectral albedo  $\alpha_k$  (Eq. 63 in Picard and Libois, 2024). Eq. 79 is used to come back to the profile of  $R_i$  used in Crocus:

$$R_{i} = \sum_{k=1}^{N_{k}} \left( (1 - \alpha_{k \text{ DIR}}) \gamma_{k \text{ DIR}} SW_{\text{DIR}} \downarrow - \sum_{j=1}^{i} E_{k_{j} \text{DIR}} + (1 - \alpha_{k \text{ DIF}}) \gamma_{k \text{ DIF}} SW_{\text{DIF}} \downarrow - \sum_{j=1}^{i} E_{k_{j} \text{DIF}} \right) \forall i \in [0, N] \quad \text{if SNOWRAD=T17}$$

$$(79)$$

The default spectral resolution is 20 nm for  $N_k = 111$  spectral bands in the interval [300 nm - 2500 nm]. Coefficients  $\gamma_k$  DIR and  $\gamma_k$  DIF to split input direct and diffuse broadband radiation in spectral solar irradiance are currently provided as fixed parameters derived from SBDART (Ricchiazzi et al., 1998) under the conditions encountered at Col de Porte site.

To compute  $E_{k_i}$ , TARTES accounts for the effect of snow physical properties (SSA and density) and Light-Absorbing Particles using the mass absorption efficiency of each LAP type and its mass content vertical profile. For dust, the mass absorption efficiency is defined following Eq. 83 of Picard and Libois (2024) with parameters  $\lambda_0 = 400$  nm, MAE( $\lambda_0$ ) =  $110 \text{ m}^2\text{kg}^{-1}$  and AAE = 4.1 (values for dust PM2.5 from Libya in Table 4 of Caponi et al., 2017). For black carbon, the mass absorption efficiency is defined following Eq. 82 of Picard and Libois (2024) with a constant density  $\rho_{BC} = 1270 \text{ kg m}^{-3}$  (Flanner et al., 2012) and a constant refractive index ( $m_{BC} = 1.95 - 0.79i$  from Bond and Bergstrom, 2006). The MAE is then scaled with a multiplicative factor  $f_{BC} = 1.638$  to obtain an MAE value at 550 nm of  $1.125 \times 10^4 \text{ m}^2\text{kg}^{-1}$  consistently with measurements of Hadley and Kirchstetter (2012). The scaling makes it possible to implicitly account for the potential absorption enhancement due to internal particle mixing or particle coating. The implementation of new types of LAP would require the implementation of the description of their associated mass absorption efficiency. The vertical profile of LAP mass content is obtained following Section 2.4.10.





#### 2.4.10 Light-Absorbing Particles

From Tuzet et al. (2017), the evolution law of the mass  $\mathcal{M}_{i,j}$  of LAP j in layer i is expressed as follows:

425 
$$\mathcal{M}_{1,j}^{+} = \mathcal{M}_{1,j}^{-} + \mathcal{W}_{w,j} \Delta t + \frac{\mathcal{W}_{d,j} \Delta t \exp\left(\frac{-z_1}{h}\right)}{\sum_{k=1}^{N} \exp\left(\frac{-Z_k}{h}\right)}$$
(80)

$$\mathcal{M}_{i,j}^{+} = \mathcal{M}_{i,j}^{-} + \frac{\mathcal{W}_{d,j} \Delta t \exp\left(\frac{-Z_i}{h}\right)}{\sum_{k=1}^{N} \exp\left(\frac{-Z_k}{h}\right)} \forall i \in [2, N]$$
(81)

where  $Z_i$  represents the depth of layer i from the surface  $(Z_i = \sum_{j=1}^i z_j)$  and h the e-folding depth characterizing the decrease rate with depth of the impact of the dry deposition flux  $W_{d,j}$ . The wet deposition flux  $W_{w,j}$  only affects the uppermost layer.

However, in case of thin layers at the surface, an homogeneous repartition is then applied on the uppermost  $N_{10}$  layers gathering the first  $10 \text{ kg m}^{-2}$  of snow. This limits artificial albedo variations due to vertical regridding (Dumont et al., 2020):

$$\mathcal{M}_{i,j}^{+} = \frac{m_i}{\sum_{k=1}^{N_{10}} m_k} \times \sum_{k=1}^{N_{10}} \mathcal{M}_{k,j}^{+} \forall i \in [1, N_{10}] \text{ where } N_{10} \text{ is the highest integer such as } \sum_{k=1}^{N_{10}-1} m_k < 10 \text{ kg m}^{-2}$$
(82)

Note than the wet deposition flux should be consistent with the occurrence of precipitation in the model input data. If not, any positive wet deposition flux without precipitation is not incorporated to the snowpack LAP mass content (Reveillet et al., 2022).

# 2.4.11 Turbulent fluxes

The sensible and latent turbulent heat fluxes are expressed by:

$$H = \rho_a c_P C_H U_{>1} \left( \frac{T_1}{\Pi_s} - \frac{T_a}{\Pi_a} \right) \tag{83}$$

$$LE = \rho_a L_s C_H U_{>1} (q_{sat}(T_1) - q_a)$$
(84)

 $\rho_a$  is the air volumetric mass (kg m<sup>-3</sup>),  $\Pi_s$  and  $\Pi_a$  the Exner functions at the surface and at the level of the atmospheric forcing and  $q_{sat}(T_1)$  the saturation specific humidity at surface temperature  $T_1$  (kg kg<sup>-1</sup>), cf. Appendix F for their computations. A minimum value of 1 m s<sup>-1</sup> is applied to wind speed ( $U_{>1} = \max(U, 1 \text{ m s}^{-1})$ ) to maintain minimal fluxes even with very low wind speeds. Note that a simplification has been introduced compared to Vionnet et al. (2012) by considering only surface sublimation and not evaporation of liquid water. The exchange coefficient  $C_H$  depends on the stability of the atmosphere through the Richardson Number Ri (Appendix F) following Noilhan and Mahfouf (1996):

$$\begin{cases}
C_{H} = \frac{\kappa_{\text{VK}}^{2}}{\ln\left(\frac{z_{u}}{z_{0}}\right)\ln\left(\frac{z_{a}}{z_{0_{h}}}\right)} \left(1 - \frac{15\text{Ri}}{1 + C_{h}\sqrt{|\text{Ri}|}}\right) & \text{if Ri} <= 0 \\
C_{H} = \frac{\kappa_{\text{VK}}^{2}}{\ln\left(\frac{z_{u}}{z_{0}}\right)\ln\left(\frac{z_{a}}{z_{0_{h}}}\right)} \times \frac{1}{1 + 15\text{Ri}^{*}\sqrt{1 + 5\text{Ri}^{*}}} & \text{if Ri} > 0 \text{ where Ri}^{*} = \min(\text{Ri}, \text{Ri}_{l})
\end{cases}$$
(85)





where  $\kappa_{VK}$  is the Von Karman constant. Coefficient  $C_h$  in the unstable case is defined by:

$$C_{h} = 15 \left( 3.2165 + 4.3431 \ln \left( \frac{z_{0}}{z_{0_{h}}} \right) + 0.5360 \left( \ln \left( \frac{z_{0}}{z_{0_{h}}} \right) \right)^{2} - 0.0781 \left( \ln \left( \frac{z_{0}}{z_{0_{h}}} \right) \right)^{3} \right) \frac{k^{2}}{\ln \left( \frac{z_{u}}{z_{0}} \right) \ln \left( \frac{z_{a}}{z_{0_{h}}} \right)} \left( \frac{z_{a}}{z_{0_{h}}} \right)^{p}$$
(86)

where 
$$p = 0.5802 - 0.1571 \ln \left( \frac{z_0}{z_{0_h}} \right) + 0.0327 \left( \ln \left( \frac{z_0}{z_{0_h}} \right) \right)^2 - 0.0026 \left( \ln \left( \frac{z_0}{z_{0_h}} \right) \right)^3$$
 (87)

In the stable case, an adjustable threshold  $Ri_l$  is applied on the Richardson number (Martin and Lejeune, 1998). Considering the high uncertainty of these parameterizations of turbulent processes, sensitivity analyses to momentum and thermodynamic roughness lengths  $z_0$  and  $z_{0_h}$  (m) and to parameter  $Ri_l$  are recommended for robust applications of the model (Lafaysse et al., 2017).

#### 2.4.12 Heat diffusion and energy balance

The formalism of this section is largely inspired by the documentation of the ISBA-ES (Explicit Snow) snowpack scheme from Boone (2002). The model solves the heat diffusion in the stratified snowpack using an implicit time integration scheme:

$$c_{I}\rho_{i}z_{i}\frac{T_{i}^{+}-T_{i}^{-}}{\Delta t}+E_{i}=G_{i-1}^{+}-G_{i}^{+}\ \forall i\in[1,N]$$
(88)

where  $G_i^+$  (Wm<sup>-2</sup>) represents the heat flux between layers i and i+1  $\forall i \in [1,N-1]$  at the end of the time step.  $G_0^+$  and  $G_N^+$  are the heat fluxes at the interfaces with atmosphere and soil at the end of the time step and  $E_i$  (Wm<sup>-2</sup>) the energy of phase change for layer i. The main assumption of the model is that it is possible to separate heat diffusion and phase changes. Thus, the diffusion is solved assuming  $E_i = 0$   $\forall i \in [1, N]$ .

The heat flux between two snow layers i and i+1 is the sum between the radiative flux  $R_i$  and the heat conduction  $K_i^+$  (Wm<sup>-2</sup>) between these layers:

$$G_i^+ = K_i^+ + R_i \,\forall i \in [1, N-1] \tag{89}$$

The conduction flux  $K_i$  is expressed at the end of the time step by:

$$K_i^+ = 2\overline{\lambda}_i \frac{T_i^+ - T_{i+1}^+}{z_i + z_{i+1}} \,\forall i \in [1, N-1]$$

$$\tag{90}$$

where  $\overline{\lambda_i}$  is the weighted mean of the thermal conductivities of layers i and i+1:

$$\overline{\lambda_i} = \frac{z_i \lambda_i + z_{i+1} \lambda_{i+1}}{z_i + z_{i+1}} \tag{91}$$

Note that some models (including ISBA-ES) rather use a harmonic weighted mean although there is not a clear agreement in the literature that it outperforms the modelling of heat diffusion (Kadioglu et al., 2008).





The thermal conductivity  $\lambda_i$  of layer i is parameterized as a function of density  $\rho_i$  following parameterizations of Yen (1981), Calonne et al. (2011) or Boone and Etchevers (2001):

If SNOWCOND=Y81: 
$$\lambda_{i} = \max \left[ a_{\lambda} \left( \frac{\rho_{i}}{\rho_{w}} \right)^{1.88} ; \lambda_{\min} \right]$$
If SNOWCOND=C11: 
$$\lambda_{i} = b_{\lambda} \rho_{i}^{2} + c_{\lambda} \rho_{i} + d_{\lambda}$$
If SNOWCOND=I02: 
$$\lambda_{i} = e_{\lambda} + f_{\lambda} \rho_{i}^{2} + \left( g_{\lambda} + \frac{h_{\lambda}}{T_{i}^{-} + i_{\lambda}} \right) \frac{P_{0}}{P}$$
(92)

All empirical parameters are provided in Appendix J3. Alternatives to Eq. 92 were proposed by Woolley et al. (2024) for Arctic snow. Although not available in version 3.0, they will be implemented in a future version.

The heat flux between the atmosphere and the surface is the sum of all energy fluxes at the surface:

$$G_0 = R_0 + \epsilon (LW \downarrow -\sigma T_1^4) - H - LE + \mathcal{P}_r \Delta t \times c_W (T_a - T_0) + E_{FRZ}$$

$$\tag{93}$$

All fluxes in Equation 93 are expressed at time  $t + \Delta t$  with the following approximation:

$$F^{+} = F^{-} + \frac{\partial F}{\partial T_{1}} (T_{1}^{+} - T_{1}^{-}) \tag{94}$$

480 Thus

$$G_{0}^{+} = R_{0} + \epsilon (LW \downarrow -\sigma(T_{1}^{-})^{3} (4T_{1}^{+} - 3T_{1}^{-})) - \rho_{a} c_{P} C_{H} U_{>1} (\frac{T_{1}^{+}}{\Pi_{s}} - \frac{T_{a}}{\Pi_{a}})$$

$$- \rho_{a} L_{s} C_{H} U_{>1} \left( q_{sat} (T_{1}^{-}) - q_{a} + \frac{\partial q_{sat}}{\partial T_{1}} (T_{1}^{+} - T_{1}^{-}) \right) + \mathcal{P}_{r} \Delta t \times c_{W} (T_{a} - T_{0}) + E_{FRZ}$$

$$(95)$$

The computation of  $\frac{\partial q_{sat}}{\partial T_1}$  is detailed in Appendix F. The heat flux between the bottom layer and the ground  $G_N^+$  is expressed with a semi-implicit coupling (i.e. considering the ground surface temperature  $T_{G_1}^-$  at time step t) in order to solve separately the thermal diffusion in the soil, outside the snowpack model:

485 
$$G_N^+ = 2\overline{\lambda_N} \frac{T_N^+ - T_{G_1}^-}{z_N + z_{G_1}} + R_N$$
 (96)

where  $\overline{\lambda_N}$  is the harmonic mean between the thermal conductivity of the bottom snow layer  $\lambda_N$  and the thermal conductivity of the first soil layer  $\lambda_{G_1}$ :

$$\overline{\lambda_N} = \frac{z_N + z_{G_1}}{\frac{z_N}{\lambda_N} + \frac{z_{G_1}}{\lambda_{G_1}}} \tag{97}$$

Combining and rearranging Eq. 88-90, 95 and 96 the system to solve becomes:

$$\begin{cases}
\left\{ \frac{\left(\frac{c_{I}\rho_{1}z_{1}}{\Delta t} + \frac{2\overline{\lambda_{1}}}{z_{1}+z_{2}} + 4\epsilon\sigma(T_{1}^{-})^{3} + \rho_{a}C_{H}U_{>1}\left(\frac{c_{P}}{\Pi_{s}} + L_{s}\frac{\partial q_{sat}}{\partial T_{1}}\right)\right)T_{1}^{+} - \frac{2\overline{\lambda_{1}}}{z_{1}+z_{2}}T_{2}^{+} = \\
\left\{ \frac{c_{I}\rho_{1}z_{1}}{\Delta t}T_{1}^{-} + R_{0} - R_{1} + \epsilon\left(LW\downarrow + 3\sigma(T_{1}^{-})^{4}\right) + \rho_{a}C_{H}U_{>1}\left(c_{P}\frac{T_{a}}{\Pi_{a}} + L_{s}\left(q_{a} - q_{sat}(T_{1}^{-}) + \frac{\partial q_{sat}}{\partial T_{1}}T_{1}^{-}\right)\right) \\
+ \mathcal{P}_{r}\Delta t \times c_{W}(T_{a} - T_{0}) + E_{FRZ} \\
-\frac{2\overline{\lambda_{i-1}}}{z_{i-1}+z_{i}}T_{i-1}^{+} + \left(\frac{c_{I}\rho_{i}z_{i}}{\Delta t} + \frac{2\overline{\lambda_{i}}}{z_{i}+z_{i+1}} + \frac{2\overline{\lambda_{i-1}}}{z_{i-1}+z_{i}}\right)T_{i}^{+} - \frac{2\overline{\lambda_{i}}}{z_{i}+z_{i+1}}T_{i+1}^{+} = \frac{c_{I}\rho_{i}z_{i}}{\Delta t}T_{i}^{-} + R_{i-1} - R_{i} \,\forall i \in [2, N-1] \\
-\frac{2\overline{\lambda_{N-1}}}{z_{N-1}+z_{N}}T_{N-1}^{+} + \left(\frac{c_{I}\rho_{N}z_{N}}{\Delta t} + \frac{2\overline{\lambda_{N}}}{z_{N}+z_{G_{1}}} + \frac{2\overline{\lambda_{N-1}}}{z_{N-1}+z_{N}}\right)T_{N}^{+} = \frac{2\overline{\lambda_{N}}}{z_{N}+z_{G_{1}}}T_{G_{1}}^{-} + \frac{c_{I}\rho_{N}z_{N}}{\Delta t}T_{N}^{-} + R_{N-1} - R_{N}
\end{cases}$$
(98)





The first line of Eq. 98 is rewritten in the form:

$$\frac{1}{C_T \Delta t} T_1^+ - \frac{\zeta_2}{C_T \Delta t} T_2^+ = \frac{\zeta_1}{C_T \Delta t} \tag{99}$$

where 
$$C_T = \frac{1}{c_I \rho_1 z_1}$$
 (100)

$$\zeta_2 = \frac{2C_T\overline{\lambda_1}}{\mathcal{A}(z_1 + z_2)} \tag{101}$$

$$\mathcal{A} = \frac{1}{\Delta t} + C_T \left[ \frac{2\overline{\lambda_1}}{z_1 + z_2} + 4\epsilon\sigma(T_1^-)^3 + \rho_a C_H U_{>1} \left( \frac{c_P}{\Pi_s} + L_s \frac{\partial q_{sat}}{\partial T_1} \right) \right]$$
(102)

$$\zeta_1 = \frac{\mathcal{B}T_1^- + \mathcal{C}}{\Delta} \tag{103}$$

$$\mathcal{B} = \frac{1}{\Delta t} + C_T \left[ 3\epsilon \sigma (T_1^-)^3 + \rho_a C_H U_{>1} \frac{\partial q_{sat}}{\partial T_1} \right]$$
(104)

$$C = C_T \left[ R_0 - R_1 + \epsilon LW \downarrow + \rho_a C_H U_{>1} \left( c_P \frac{T_a}{\Pi_a} + L_s \left( q_a - q_{sat}(T_1^-) \right) \right) + \mathcal{P}_r \Delta t \times c_W (T_a - T_0) + E_{FRZ} \right]$$

$$(105)$$

Therefore, the temperature profile at time  $t + \Delta t$  is obtained by:

$$\begin{bmatrix}
T_1^+ \\
T_2^+ \\
... \\
T_i^+ \\
... \\
T_N^+
\end{bmatrix} = \begin{bmatrix}
B_1 & C_1 & 0 & 0 & ... & ... & 0 \\
A_2 & B_2 & C_2 & 0 & ... & ... & 0 \\
0 & A_3 & ... & ... & ... & ... & ... \\
0 & 0 & ... & B_i & C_i & ... & 0 \\
... & ... & ... & 0 & ... & ... & ... \\
0 & 0 & ... & ... & ... & ... & 0 \\
... & ... & ... & ... & ... & ... & ... & ... \\
0 & 0 & ... & 0 & 0 & A_N & B_N
\end{bmatrix} \begin{bmatrix}
Y_1 \\
Y_2 \\
... \\
Y_i \\
... \\
... \\
Y_N
\end{bmatrix}$$
(106)

495





where vectors  $A = (A_2, ..., A_i, ...A_N)$ ,  $B = (B_1, ..., B_i, ...B_N)$ ,  $C = (C_1, ..., C_i, ...C_{N-1})$ ,  $Y = (Y_1, ..., Y_i, ...Y_N)$  are defined by:

$$\begin{cases}
A_{i} = -\frac{2\overline{\lambda_{i-1}}}{z_{i-1}+z_{i}} \forall i \in [2, N] \\
B_{1} = \frac{1}{C_{T}\Delta t} \\
B_{i} = \left(\frac{c_{I}\rho_{i}z_{i}}{\Delta t} + \frac{2\overline{\lambda_{i}}}{z_{i}+z_{i+1}} + \frac{2\overline{\lambda_{i-1}}}{z_{i-1}+z_{i}}\right) \forall i \in [2, N-1] \\
B_{N} = \left(\frac{c_{I}\rho_{N}z_{N}}{\Delta t} + \frac{2\overline{\lambda_{N}}}{z_{N}+z_{G_{1}}} + \frac{2\overline{\lambda_{N-1}}}{z_{N-1}+z_{N}}\right) \\
C_{1} = -\frac{C_{2}}{C_{T}\Delta t} \\
C_{i} = -\frac{2\overline{\lambda_{i}}}{z_{i}+z_{i+1}} \forall i \in [2, N-1] \\
Y_{1} = \frac{C_{1}}{C_{T}\Delta t} \\
Y_{i} = \frac{c_{1}\rho_{i}z_{i}}{\Delta t} T_{i}^{-} + R_{i-1} - R_{i} \forall i \in [2, N-1] \\
Y_{N} = \frac{2\overline{\lambda_{N}}}{z_{N}+z_{G_{1}}} T_{G_{1}}^{-} + \frac{c_{I}\rho_{N}z_{N}}{\Delta t} T_{N}^{-} + R_{N-1} - R_{N}
\end{cases}$$
(107)

# 2.4.13 Adjustments in case of surface melting

The possibility for  $T_1^+$  to exceed the freezing point in the solving of Eq. 106 can lead to overestimate the surface energy fluxes that depend on  $T_1^+$  and to overestimate the heat conduction  $K_1$  below surface. To avoid this numerical artefact, Crocus distinguishes the case of first melting  $(T_1^- < T_0)$  and  $T_1^+ > T_0)$ , and ongoing melting  $(T_1^- \ge T_0)$  and  $T_1^+ > T_0)$ .

In the case of a first melting  $(T_1^- < T_0 \text{ and } T_1^+ > T_0)$ , the temperature profile for layers  $i \in [2, N]$  is not updated, so only the surface fluxes are adjusted replacing  $T_1^+$  by  $T_0$  in Eq. 83, 84, 95. The new temporary surface temperature (before melting) is obtained by converting the difference in both consecutive estimates of the surface energy flux  $G_0$  in terms of temperature change:

If 
$$T_{1}^{-} < T_{0}$$
 and  $T_{1}^{+} > T_{0}$ :
$$\begin{cases}
G_{0}^{+} = R_{0} + \epsilon (LW \downarrow -\sigma(T_{1}^{-})^{3} (4T_{0} - 3T_{1}^{-})) - \rho_{a} c_{P} C_{H} U_{>1} (T_{0} - T_{a}) \\
-\rho_{a} L_{s} C_{H} U_{>1} \left( q_{sat} (T_{1}^{-}) - q_{a} + \frac{\partial q_{sat}}{\partial T_{0}} (T_{0} - T_{1}^{-}) \right) + \mathcal{P}_{r} \Delta t \times c_{W} (T_{a} - T_{0}) \\
T_{1}^{+} = T_{1}^{\text{first}} + \frac{\Delta t}{c_{I} \rho_{i} z_{i}} (G_{0}^{+} - G_{0}^{\text{first}})
\end{cases}$$
(108)

where  $T_1^{\text{first}}$  is the solution of Eq. 106, and  $G_0^{\text{first}}$  the flux obtained applying Eq. 95 with  $T_1^{\text{first}}$ . This ensures that the energy budget over the snowpack is closed.

In the case of an ongoing melting (i.e. the solution of Eq. 106 provides a temperature above freezing point for the surface layer at two consecutive time steps:  $T_1^- \ge T_0$  and  $T_1^+ > T_0$ ), the system is solved a second time for layers  $i \in [2, N]$  by





constraining  $T_1^+ = T_0$ :

$$\begin{bmatrix} T_2^+ \\ \dots \\ T_i^+ \\ \dots \\ T_N^+ \end{bmatrix} = \begin{bmatrix} B_2 & C_2 & 0 & \dots & \dots & 0 \\ A_3 & \dots & \dots & \dots & \dots & \dots \\ 0 & \dots & B_i & C_i & \dots & 0 \\ \dots & \dots & A_i & \dots & \dots & 0 \\ \dots & \dots & \dots & \dots & \dots & C_{N-1} \\ 0 & \dots & 0 & 0 & A_N & B_N \end{bmatrix}^{-1} \begin{bmatrix} Y_2 + \frac{2\overline{\lambda_1}}{z_1 + z_2} T_0 \\ \dots & \dots & \dots & \dots \\ Y_i \\ \dots & \dots & \dots & \dots \\ Y_N \end{bmatrix}$$
(109)

Then, the surface energy fluxes are updated replacing  $T_1^+$  and  $T_1^-$  by  $T_0$  in Eq. 83, 84, 95 and the conduction flux between the two first layers is updated with the solution of Eq. 109. A new estimate of the surface layer  $T_1^+$  is temporarily obtained from Eq. 88 (i = 1) consistently with these updated fluxes, before the transfer of exceeding energy in phase change ( $E_1$ , see Section 2.4.16):

If 
$$T_{1}^{-} \geq T_{0}$$
 and  $T_{1}^{+} > T_{0}$ :
$$\begin{cases}
G_{0}^{+} = R_{0} + \epsilon(LW \downarrow -\sigma T_{0}^{4}) - \rho_{a} c_{P} C_{H} U_{>1}(T_{0} - T_{a}) \\
-\rho_{a} L_{s} C_{H} U_{>1}(q_{sat}(T_{0}) - q_{a}) + \mathcal{P}_{r} \Delta t \times c_{W}(T_{a} - T_{0}) \\
K_{1}^{+} = 2 \overline{\lambda_{i}} \frac{T_{0} - T_{2}^{+}}{z_{i} + z_{i+1}} \\
T_{1}^{+} = T_{0} + \frac{\Delta t}{c_{I} \rho_{i} z_{i}} \left(G_{0}^{+} - K_{1}^{+} - R_{1}\right)
\end{cases}$$
(110)

This also guarantees the closure of the energy budget in that case. Note that Fourteau et al. (2024) recently proposed alternative model formulations to compute a more stable surface energy balance with a better coupling between surface melting and heat transfers. This should be explored in the future to avoid the need of such numerical adjustments.

# 2.4.14 Coupling with MEB

530

535

MEB (Multiple Energy Balance, Boone et al., 2017) is a variant of the ISBA land surface scheme in which the soil-vegetation system is no longer described by a composite approach but by an explicit representation of vegetation with a big-leaf approach. This allows to represent the main physical processes involved in forest-snow interactions including snowfall interception and radiative impacts of the trees. An extensive description of this implementation is beyond the scope of this paper but available in Boone et al. (2017). However, as coupled processes require a coupled solving of snow surface and vegetation temperatures  $T_1$  and  $T_v$ , the solving of heat diffusion is modified when Crocus is coupled to the MEB scheme. In that case, the values of the surface energy fluxes are no longer obtained through the implicit solving of Eq. 98-106 but are imposed as a boundary condition to conserve energy. Eq. 88 is modified for the surface layer to maintain the fluxes obtained from MEB:

$$c_I \rho_i z_i \frac{T_1^+ - T_1^-}{\Delta t} + E_1 = G_{0_{\text{MEB}}} - R_1 - K_1^+ \tag{111}$$

where 
$$G_{0_{\text{MEB}}} = R_0 + \epsilon (\text{LW} \downarrow -\sigma T_{1_{\text{MEB}}}^4) - H_{\text{MEB}} - LE_{\text{MEB}} + \mathcal{P}_r \Delta t \times c_W (T_a - T_0)$$
 (112)



540

555

560



 $G_{0_{\mathrm{MEB}}}$  represents the total surface energy flux in agreement with the first estimate of surface temperature from MEB  $T_{1_{\mathrm{MEB}}}$  and the associated turbulent fluxes  $H_{\mathrm{MEB}}$  and  $LE_{\mathrm{MEB}}$ . LW $\downarrow$  accounts for vegetation radiation and is therefore linked to the solution obtained for vegetation temperature  $T_{v_{\mathrm{MEB}}}$ . It must be noted that as  $R_0$  and  $R_1$  are already needed in MEB, they are computed with the same routine as described in Section 2.4.9 but earlier in the time step (before the MEB solving) to guarantee identical values at both steps (MEB and Crocus), and accounting for shading by trees in SW $\downarrow$ .

Consistently with Eq. 111, the first line of Eq. 98 is replaced by:

$$\left(\frac{c_I \rho_1 z_1}{\Delta t} + \frac{2\overline{\lambda_1}}{z_1 + z_2}\right) T_1^+ - \frac{2\overline{\lambda_1}}{z_1 + z_2} T_2^+ = \frac{c_I \rho_1 z_1}{\Delta t} T_1^- + G_{0_{\text{MEB}}} - R_1 \tag{113}$$

Rewriting Eq. 113 with the same form as Eq. 99 is equivalent to replacing Eq. 102, 104, 105 by:

$$\mathcal{A} = \frac{1}{\Delta t} + C_T \left[ \frac{2\overline{\lambda_1}}{z_1 + z_2} \right] \tag{114}$$

$$\mathcal{B} = \frac{1}{\Delta t} \tag{115}$$

$$C = C_T \left[ G_{0_{\text{MEB}}} - R_1 \right] \tag{116}$$

and to solving the linear system of Eq. 106 with coefficients  $C_1$  and  $Y_1$  of Eq. 107 modified accordingly to the new values of  $\zeta_2$  and  $\zeta_1$  from Eq. 101 and Eq. 103. The adjustments of Section 2.4.13 are no longer required as  $G_0$  is imposed by MEB and phase change was already accounted for to compute this flux.

The validity of Eq. 113 would require that no modification of the state variables of the snowpack has occurred between the computation of  $G_{0_{\rm MEB}}$  and the solving of Eq. 106 because  $G_{0_{\rm MEB}}$  depends on snow properties through Eq. 48 and 49 in Boone et al. (2017) and the associated Appendix I4. In practice, the SURFEX code structure makes this constraint especially challenging. The violation of this assumption can generate numerical instabilities especially with thin surface layers due to the violation of the second principle of thermodynamics. To reduce as much as possible the occurrence of this problem, the sequence of routines is modified following Figure 1. However, there is currently no solution to avoid modifications due to snow interception by vegetation because this term can not be computed before MEB solving (the mass balance depends on latent heat terms known only after the solving). Numerical instabilities are therefore still possible and further investigations are in progress to safely allow large scale applications of MEB-Crocus. This issue is more challenging than in the case of the coupling of MEB with ES snow scheme (Boone et al., 2017; Napoly et al., 2020) which has already been successfully applied in large scale simulations. This is probably due to the possible occurrence of thinner surface snow layers with Crocus.

# 2.4.15 Total melting or sublimation

The snowpack is assumed to totally disappear when

565 
$$G_0^+ - G_N^+ \ge \frac{-\sum_{i=1}^{N^t} H_i^+ + H_{\text{subl}}}{\Delta t} \text{ or } \frac{\max(0, LE^+)\Delta t}{L_s} \ge \sum_{i=1}^{N^t} m_i$$
 (117)

The first condition corresponds to a total melt of the snowpack (energy gain during the time step exceeds available internal energy for melting. It requires to remove the enthalpy of surface snow potentially sublimated  $H_{\rm subl}$  from the total enthalpy.





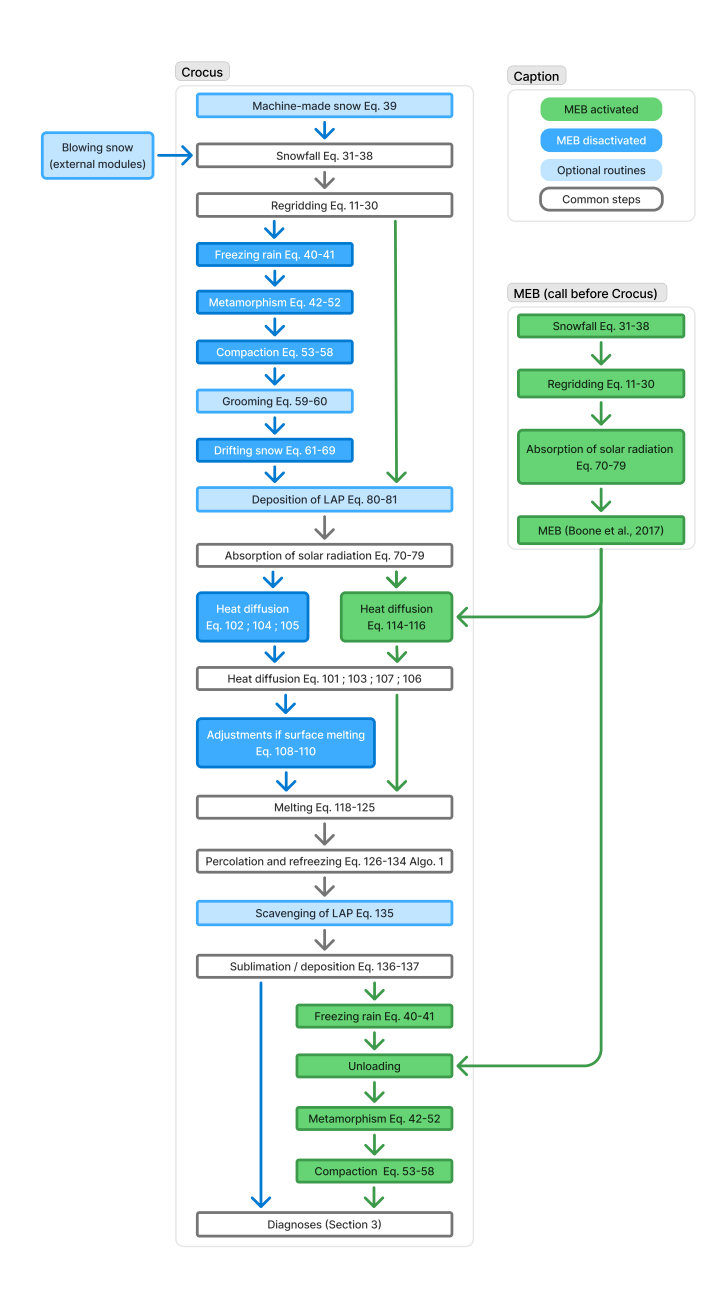


**Figure 1.** Sequence of Crocus subroutines for each time step without (blue) or with (green) coupling with MEB. Optional subroutines in light blue.





The second condition corresponds to a total sublimation of the snowpack, which is a very unusual case of snow disappearance but can appear especially when a snow transport module provide a very low amount of snow on bare ground in cold and windy conditions.

In both cases, for mass conservation, the runoff at the bottom of the snowpack is set to the total snow mass and the energy associated with  $LE^+$  is transmitted to the soil scheme as a correction term. If Eq. 117 is not verified, the procedure follows Sect. 2.4.16 to Sect. 2.4.20.

### **2.4.16** Melting

580

Let's define the mass of solid and liquid fractions of the snow before any phase change  $s_i^-$  and  $l_i^-$  (kg m<sup>-2</sup>):

$$s_i^- = m_i - l_i^- \tag{118}$$

When the heat diffusion solving provides a temperature  $T_i^+$  above the melting point  $T_0$  for layer i, the model simulates melting. The energy available for fusion  $E_{f_i}$  (J m<sup>-2</sup>) on layer i can be constrained either by the heating energy either by the available mass of the solid fraction of snow before melting  $s_i^-$ . Thus, the energy and mass  $f_i$  (kg m<sup>-2</sup>) of melting during the time step are computed by:

$$E_{f_i} = \min\left(c_I \rho_i (T_i^+ - T_0), L_m s_i^-\right) \tag{119}$$

$$f_i = \frac{E_{f_i}}{L_m} \tag{120}$$

The mass of solid and liquid fractions after melting are:

$$s_i^+ = s_i^- - f_i (121)$$

585 
$$l_i^+ = l_i^- + f_i$$
 (122)

The corresponding updates of depth and total density can be expressed by:

$$z_i^+ = z_i^- \times \frac{m_i - l_i^+}{m_i - l_i^-} \tag{123}$$

$$\rho_i^+ = \frac{m_i}{z_i^+} \tag{124}$$

In case of melting, the melting point temperature is attributed to the layer temperature:

590 
$$T_i^{++} = \min(T_0, T_i^+)$$
 (125)

In practice, a first evaluation of Eq.119-120 is computed for all layers to identify cases where a numerical layer fully melts out  $(c_I\rho_i(T_i^+-T_0)\geq L_ms_i^-)$ . In such a case, the numerical layer i is aggregated with the numerical layer i+1 for  $i\in[1,N-1]$ , following Equations 12-20. If the bottom layer N is concerned, it is agregated with the above layer N-1. Several iterations can be done in case of melting of multiple consecutive layers. Then, the melting is computed again with this updated discretization with the guarantee that all numerical layers remain defined.



600



# 2.4.17 Refreezing

When the heat diffusion solving provides a temperature  $T_i^+$  below the melting point  $T_0$  whereas liquid water is present, the model simulates refreezing. The energy available for refreezing  $E_{r_i}$  (J m<sup>-2</sup>) can be constrained either by the layer cooling after diffusion either by the maximum available liquid water content before refreezing  $l_i^-$ . Thus, the energy and mass  $r_i$  (kg m<sup>-2</sup>) of refreezing during the time step are computed by:

$$E_{r_i} = \min(c_I \rho_i (T_0 - T_i^+), L_m l_i^-) \tag{126}$$

$$r_i = \frac{E_{r_i}}{L_m} \tag{127}$$

The mass of solid and liquid fractions after refreezing are:

$$s_i^+ = s_i^- + r_i$$
 (128)

$$605 \quad l_i^+ = l_i^- - r_i \tag{129}$$

The energy conservation during the refreezing process is expressed by:

$$c_I \rho_i (T_i^+ - T_i^{++}) s_i^+ + E_{r_i} + c_I \rho_i (T_0 - T_i^+) r_i = 0$$
(130)

where  $T_i^+$  and  $T_i^{++}$  (K) are the layer temperature of the solid fraction before and after refreezing. In Eq. 130, the first term corresponds to the heating of the solid fraction after refreezing, the second term to the latent heat release due to refreezing and the third term to the cooling of the refrozen part necessary for the thermal equilibrium of the solid phase.

By combining Eq. 130 and 129, the evolution of the layer temperature due to refreezing is computed by:

$$T_i^{++} = T_0 + (T_i^+ - T_0) \frac{s_i^-}{s_i^+} + \frac{E_{r_i}}{c_I \rho_i s_i^+}$$
(131)

Equations 126-131 are not applied independently but jointly with liquid water percolation as described in Section 2.4.18 within Algorithm 1

# 615 2.4.18 Liquid water percolation

Let's define the volumetric liquid water content  $w_i$  (kg m<sup>-3</sup>):

$$w_i = \frac{l_i}{z_i} \tag{132}$$

and the snow porosity:

$$\phi_i = 1 - \frac{\rho_i^- - w_i}{\rho_I} \tag{133}$$

where  $\rho_I$  is the volumetric mass of pure ice. The liquid water flow  $\mathcal{F}_i$  (kg m<sup>-2</sup>) between layers i and i+1 is computed by a simple and conceptual bucket approach where the layers are seen as superposed water reservoirs with a maximum liquid water



625



holding capacity  $w_{i \max}$ . The excess water drains to the underlying layer when  $w_i$  exceeds  $w_{i \max}$  following Algorithm 1. Snow layer densities  $\rho_i$  are updated with the resulting net mass flux  $\mathcal{F}_i - \mathcal{F}_{i-1}$ . However, in the limit case of ice layers  $(\rho = \rho_I)$ , in case of refreezing, the excess mass increases the ice layer depth at constant density. Note that another choice would be possible (Fourteau et al., 2024) by considering ice layers impermeable (i.e. computing  $\mathcal{F}_i$  before any refreezing and  $r_i$  after percolation) with potential impacts on glaciers simulations.

### Algorithm 1 Buckets algorithm for liquid water percolation

$$\begin{split} \mathcal{F}_0 &= \mathcal{P}_r \Delta t \\ \text{for } i \in [1, N] \text{ do} \\ &\text{Compute } r_i, s_i, w_i \text{ with Eq. 126-132} \\ w_i^* &= w_i + \frac{\mathcal{F}_{i-1} + f_i - r_i}{z_i} \\ \mathcal{F}_i &= \max(0, w_i^* - w_{i \max}) z_i \\ w_i &= w_i^* - \frac{\mathcal{F}_i}{z_i} \\ \rho_i^+ &= \rho_i^- (\mathcal{F}_i - \mathcal{F}_{i-1}) \frac{\rho_W}{z_i} \\ \text{if } \rho_i^+ &> \rho_I \text{ then} \\ z_i &= \frac{\rho_i^+}{\rho_I} z_i \\ \rho_i^+ &= \rho_I \\ \text{end if} \\ \text{end for} \end{split}$$

Several formulations of  $w_{i \text{ max}}$  were implemented by Lafaysse et al. (2017):

$$\begin{cases} \text{If SNOWLIQ = B92:} & w_{i \max} = 0.05 \rho_{w} \phi_{i} \\ \text{If SNOWLIQ = SPK:} & \begin{cases} w_{i \max} = \rho_{w} \left( 0.08 - 0.1023 (0.97 - \phi_{i}) \right) & \text{if } \phi_{i} \geq 0.77 \\ w_{i \max} = \rho_{w} \left( 0.0264 + 0.0099 \frac{\phi_{i}}{1 - \phi_{i}} \right) & \text{otherwise} \end{cases} \\ \text{If SNOWLIQ = B02:} & w_{i \max} = \rho_{i} \left( r_{\min} + \left( r_{\max} - r_{\min} \right) \max \left( 0, \frac{\rho_{r} - \rho_{i}}{\rho_{r}} \right) \right) \end{cases}$$

Parameters  $r_{\min}$ ,  $r_{\max}$   $\rho_r$  are defined in Appendix J3.

The resolution of Richards equations might help improve the realism of this process in a detailed snowpack model (Wever et al., 2014, 2015, 2016a, b, 2017). However, the developments of D'Amboise et al. (2017) are not sufficiently robust to be available in this official release. More stable and numerically efficient alternatives are emerging and might be preferred in the future following the recommendations of Fourteau et al. (2025).

#### 2.4.19 Scavenging of LAP

635 When LAP are activated (Section 2.4.10), liquid water percolation may carry a fraction of LAP mass (Tuzet et al., 2017):

$$\mathcal{M}_{i,j}^{+} = \mathcal{M}_{i,j}^{-} - \mathcal{F}_i \times C_{\text{scav},j} \times \frac{\mathcal{M}_{i,j}^{-}}{m_i}$$
(135)





The scavenging coefficient  $C_{\text{scav},j}$  can be adjusted by the user for each LAP j (default values are set to  $C_{\text{scav},j} = 0$  i.e. no scavenging).

#### 2.4.20 Sublimation and deposition

Sublimation and deposition are accounted for adding or deleting mass to the surface layer accordingly with the surface latent heat flux (Eq. 84 where  $T_1$  is the solution of Eq. 106, 108 or 110 depending on the occurrence of melting).

$$z_i^+ = \max(z_i + LE \frac{\Delta t}{L_s(\rho_i^- - \frac{l_i}{z_-^-})}, 0)$$
(136)

$$\rho_i^+ = \rho_i^- + \frac{l_i}{z_i^+} \tag{137}$$

Microstructure properties are not modified. Therefore, the current Crocus snow model does not allow to follow the burying of surface hoar as a dedicated snow layer. In the very unusual cases when the mass of the surface layer is insufficient for sublimation  $(-LE\frac{\Delta t}{L_s}>z_i(\rho_i^--\frac{l_i}{z_i^-})$  which only occurs for extremely thin snowpacks), the quantity  $-LE\frac{\Delta t}{L_s}-z_i(\rho_i^--\frac{l_i}{z_i^-})$  is later extracted from the first soil layer in the ISBA-DIF soil scheme to conserve energy, and the remaining liquid water, if any, is transferred to the next layer. A homogeneous regridding is applied before the next time step.

#### 2.4.21 Unloading from vegetation

In case of unloading from vegetation, the initial implementation of MEB consisted in adding the unloaded mass to the mass of solid precipitation  $m_{\rm SP}$ , following Eq. 36 and 37 for snow density and microstructure. This could lead to unrealistic surface density when unloading occurred in cold conditions. A recent new parameterization instead attributes a fixed density  $\rho_{\rm UN}$  and microstructure properties  $d_{\rm UN}$  and  $S_{\rm UN}$  to unloaded snow. The associated snow mass is either aggregated to the surface snow layer following Eq. 12-20 or associated to a new snow layer depending on the properties of the surface snow layer.

### 655 3 Diagnoses

This section describes the complementary diagnoses of a Crocus simulation provided in addition to the state variables of the model.

#### 3.1 Diagnoses of recent, wet or refrozen snow

We define  $n_X$  as the number of snow layers more recent than X days, i.e. satisfying the following condition:

660 
$$A_i < X \, \forall i \in [1, n_X]$$
 (138)





Thus, thickness  $Z_X$  and mass  $M_X$  of snow more recent than X days are defined by:

$$Z_X = \sum_{i=1}^{n_X} z_i \tag{139}$$

$$M_X = \sum_{i=1}^{n_X} m_i \tag{140}$$

These diagnoses are provided for  $X \in [0.5, 1, 3, 5, 7]$ . Similarly, the number of wet and refrozen snow layers from the surface  $n_w$  and  $n_r$  are defined by:

$$l_i > 0 \,\forall i \in [1, n_w] \tag{141}$$

$$l_i < 0 \,\forall i \in [1, n_r] \tag{142}$$

The thickness of wet and refrozen snow  $Z_w$  and  $Z_r$  are diagnosed by:

$$Z_w = \sum_{i=1}^{n_w} z_i \tag{143}$$

670 
$$Z_r = \sum_{i=1}^{n_r} z_i$$
 (144)

# 3.2 Grain type classification

For each snow layer, a diagnosis of grain type  $\Theta_i$  is derived from values of optical diameter and sphericity through the following classification (Eq. 145) in which  $\delta_i(d_i, S_i)$  and  $g_{s_i}(d_i, S_i)$  are defined respectively by Eq. D2 and D6. The values taken by  $\Theta_i$  are taken from the International Snow Classification (Fierz et al., 2009) and include PP (Precipitation Particles), DF (Decomposited Fragments), RG (Rounded Grains), FC (Faceted Crystals), DH (Depth Hoars), MF (Melt Forms) and combinations of these types.





$$\text{If } d_i < 10^{-4} (4-S_i) \\ \text{If } \delta_i \in [0;0.3] \\ \text{If } \delta_i \in [0.3;0.6] \\ \text{O}_i = \text{DF} \\ \text{If } \delta_i \in [0.3;0.6] \\ \text{O}_i = \text{DF} \\ \text{If } \delta_i \in [0.6;0.8] \\ \text{O}_i = \text{PP} \\ \text{If } \delta_i \in [0.8;1.0] \\ \text{O}_i = \text{PP} \\ \text{If } \delta_i \in [0.8;1.0] \\ \text{O}_i = \text{PP} \\ \text{If } S_i \in [0.2;0.8] \\ \text{O}_i = \text{RG} \\ \text{If } S_i \in [0.2;0.8] \\ \text{O}_i = \text{RG} \\ \text{If } S_i \in [0.2;0.8] \\ \text{O}_i = \text{RG} \\ \text{If } S_i \in [0.2;0.8] \\ \text{O}_i = \text{RG} \\ \text{If } S_i \in [0.2;0.8] \\ \text{O}_i = \text{RG} \\ \text{If } S_i \in [0.2;0.8] \\ \text{O}_i = \text{RG} \\ \text{O}_i = \text{RG} \\ \text{If } S_i \in [0.55,1.05] \\ \text{If } S_i \in [0.55,1.05] \\ \text{If } S_i \in [0.55,0.5] \\ \text{If } S_i \in [0.55,0.55] \\ \text{If } S_i \in [0.55,0.5] \\ \text{If } S_i \in [0.55,0.55] \\ \text{O}_i = \text{MF} \\ \text{O}_i = \text{O}_i = \text{MF} \\ \text{O}_i = \text{MF} \\ \text{O}_i = \text{MF} \\ \text{O}_i = \text{MF}$$

# 3.3 Snowmaking diagnoses

The water use for snowmaking is obtained by:

$$V_{\rm SM} = \frac{m_{\rm SM} A_{\rm SM}}{(1 - \mathcal{L}_{\rm SM})\rho_w} \tag{146}$$

It is cumulated since the beginning of the season in the model diagnoses.





#### 3.4 Optical diagnoses

The specific surface area  $SSA_i$  (m<sup>2</sup>kg<sup>-1</sup>) of each snow layer i is directly diagnosed from the optical diameter by:

$$SSA_i = \frac{6}{d_i \rho_I} \tag{147}$$

When CSNOWRAD=T17, spectral albedo values are also provided from an integration of incoming and absorbed radiations over user-defined spectral bands.

### 3.5 Mechanical diagnoses

#### 3.5.1 Penetration resistance

A penetration resistance is computed for each layer. It is designed to represent the measurement obtained by the rammsonde commonly used in field snowpack observations (Giraud et al., 2002). The value of penetration resistance  $\mathcal{R}_{p_i}$  is inferred for each layer  $i \in [1, N]$  by Eq. 148 from microstructure properties  $(d_i, S_i)$  and the transformation  $g_{s_i}(d_i, S_i)$  following Eq. D6), density  $\rho_i$ , liquid water content  $w_i$  (kg m<sup>-3</sup>) and temperature  $\theta_i$  (°C). The result is expressed in kgf (1 kgf  $\simeq$  9.81 N).

$$\begin{cases} \text{If } d_{i} < 10^{-4} (4 - S_{i}) : & \mathcal{R}_{p_{i}} = \frac{d_{i} \times 10^{4} - 4 + S_{i}}{S_{i} - 3} \times \max(1, 0.018\rho_{i} - 1.363) + \frac{1 - d_{i} \times 10^{4}}{S_{i} - 3} \times \max[2, S_{i}(0.17\rho_{i} - 31) + (1 - S_{i})(0.085\rho_{i} - 14.9)] \\ \text{If } \Theta_{i} = \text{RG} : & \begin{cases} \text{If } \rho_{i} < 200 : \mathcal{R}_{p_{i}} = 3 \\ \text{else:} \mathcal{R}_{p_{i}} = 0.17\rho_{i} - 31 \end{cases} \\ \text{If } \Theta_{i} = \text{RG+FC} : & \begin{cases} \text{If } \rho_{i} < 200 : \mathcal{R}_{p_{i}} = 2 \\ \text{else:} \mathcal{R}_{p_{i}} = S_{i} \times (0.17\rho_{i} - 31) + (1 - S_{i}) \times (0.17\rho_{i} - 31) \cdot (0.8 - g_{s_{i}}(d_{i}, S_{i})) + 2 \times g_{s_{i}}(d_{i}, S_{i}) \end{cases} \\ \text{else:} & \begin{cases} \text{If } \theta_{i} < 200 : \mathcal{R}_{p_{i}} = 2 \\ \text{else:} \mathcal{R}_{p_{i}} = 3 \cdot (0.8 - g_{s_{i}}(d_{i}, S_{i})) + 2 \cdot g_{s_{i}}(d_{i}, S_{i}) \end{cases} \\ \text{else:} & \begin{cases} \text{If } \theta_{i} < 200 : \mathcal{R}_{p_{i}} = 3 \cdot (0.8 - g_{s_{i}}(d_{i}, S_{i})) + 2 \cdot g_{s_{i}}(d_{i}, S_{i}) \\ \text{else:} \mathcal{R}_{p_{i}} = 0.17\rho_{i} - 31 \end{cases} \\ \text{If } \Theta_{i} \in \begin{bmatrix} \text{MF} \\ \text{MF+RG} \\ \text{MF+PC} \\ \text{MF+DH} \end{bmatrix} : & \begin{cases} \text{If } \theta_{i} < -0.2 \text{ or } w_{i} < 5 ) : \mathcal{R}_{p_{i}} = \max(10, 0.103\rho_{i} - 19.666) \\ \rho_{i} < 250, \mathcal{R}_{p_{i}} = 1 \\ 250 \leq \rho_{i} < 350, \mathcal{R}_{p_{i}} = 2 \\ \rho_{i} \geq 350, \mathcal{R}_{p_{i}} = 0.16\rho_{i} - 54 \end{cases} \end{cases}$$

$$(148)$$

# 3.5.2 Shear strength

To be able to compute stability indices of the snowpack, a shear resistance  $\mathcal{R}_{s_i}$  computed is diagnosed for each layer i. It is also computed from microstructure properties, density, liquid water content and temperature through Eq. 149.  $\mathcal{R}_{s_i}$  is expressed





in kgf dm<sup>-2</sup> (1 kgf dm<sup>-2</sup>  $\simeq 0.981$  kPa).

 $C_1, C_2, C_3, C_4$  and  $C_5$  multiplicative functions are defined in Appendix G.

# 700 **3.6 MEPRA**

705

MEPRA was a standalone module designed to estimate the avalanche hazard from the snowpack stratigraphy simulated by Crocus, from mechanical diagnosis and expert rules (Giraud et al., 2002). It has been fully implemented in the SURFEX platform, and its output are now available with the other diagnostic variables. The general idea is to compare the shear strength  $\mathcal{R}_{s_i}$  as defined previously, to the shear stress in the layer. For natural release, only the weight of overlying layers is taken into account while the load related to the presence of a skier at the snowpack surface is added to represent the accidental triggering. Expert rules are then defined to determine a hazard indice from these mechanical stability indicators, both for natural release and accidental triggering. Expert rules were defined with the work of Giraud et al. (2002) but remained largely unpublished and evolved through versions of Crocus, mainly from feedbacks of operational forecasters. Equations implemented in the current version of SURFEX are described below. They are only valid for slope angle valus  $\gamma = 40^{\circ}$ .

# 710 3.6.1 Mechanical stability of snowpack layers

A simple mechanical diagnosis for stability is computed by dividing the shear resistance  $\mathcal{R}_{s_i}$  by the shear in the layer. Two values are computed, to discriminate between natural avalanche activity and human triggering.

#### Natural release

The stability indice  $\mathcal{S}_{\mathrm{nat}_i}$  for natural release is defined in each layer i as follows:

715 
$$S_{\text{nat}_i} = \frac{\mathcal{R}_{s_i}}{\sigma_{i+1}}$$
 (150)

where  $\sigma_{i+1}$  is the weight of overlying layers (including considered layers), projected on the slope-parallel axis, as defined by Eq. 54.

## **Accidental triggering**

The stability indice for accidental triggering  $S_{acc_i}$  is similar to equation 150, with a supplementary term for shear stress to represent the additional load on the snowpack:

$$S_{\text{acc}_i} = \frac{\mathcal{R}_{s_i}}{\sigma_{i+1} + \Xi_i \sigma_{\text{acc}_i}} \tag{151}$$





where  $\sigma_{acc_i}$  is designed to represent the shear load induced by a skier, defined as a piecewise linear decreasing function of depth  $Z_i = \sum_{j=1}^i z_j$ :

$$\sigma_{\text{acc}_{i}} = \begin{cases} 4 - 15Z_{i} & \text{if } Z_{i} < 0.1\\ 2.5 - 10(Z_{i} - 0.1) & \text{if } 0.1 \leq Z_{i} < 0.15\\ 2 - 8(Z_{i} - 0.15) & \text{if } 0.15 \leq Z_{i} < 0.2\\ 1.6 - 4(Z_{i} - 0.2) & \text{if } 0.2 \leq Z_{i} < 0.35\\ 1 - 2(Z_{i} - 0.35) & \text{if } 0.35 \leq Z_{i} < 0.5\\ 0.7 - 1.5(Z_{i} - 0.5) & \text{if } 0.5 \leq Z_{i} < 0.8\\ 0 & \text{if } 0.8 \leq Z_{i} \end{cases}$$

$$(152)$$

and  $\Xi_i$  is designed to represent the bonding effect reducing the shear stress in the layers, defined by:

$$\Xi_{i} = \frac{\sum_{j=1}^{i} m_{j} \xi_{j}}{\sum_{j=1}^{i} m_{j}} \text{ where } \xi_{i} : \begin{cases} \text{If } \Theta_{i} \in \begin{cases} \text{MF, RG+MF,} \\ \text{MF+FC, MF+DF} \end{cases} & \begin{cases} \text{If } \theta_{i} < -0.2, \ \xi_{i} = 0.5 \\ \text{else: } \xi_{i} = 1.1 \end{cases} \\ \text{If } \mathcal{R}_{s_{i}} > 1.5 : \ \xi_{i} = 1.0 \\ \text{else: } \xi_{i} = 1.2 \end{cases}$$

$$(153)$$

#### 3.6.2 Hazard indices

MEPRA analyses the profiles of  $S_{\text{nat}_i}$  and  $S_{\text{acc}_i}$  mechanical indices with other parameters (mainly grain type, temperature and liquid water content and snow heights), to assess a natural avalanche hazard indice  $\mathcal{H}_{\text{nat}}$ , on a scale of 0-5 and accidental hazard indice  $\mathcal{H}_{\text{acc}}$  on a scale 0-3, with a set of expert rules presented below. These hazard indices are associated with levels of instability (one for high instability,  $Z_h$ , and one for moderate instability,  $Z_m$ , at most). For natural release, a classification between 5 avalanche types is also provided.

#### Natural release

730

The natural release analysis relies on a classification of the upper layers of the snowpack (referred as "superior profile") in 4 classes: NEW (new snow), WET (wet snowpack), FRO (refrozen snowpack) or NAN (when it could not be classified in other class), based on the conditions listed in Table H1. A height of this superior profile  $Z_{SUP}$  is also defined below which the snowpack is significantly different, and called inferior profile. The latter is also classified into three classes (SOF, HAR and NAN) following Table H2.

Levels of high and moderate instabilities are looked for in the superior profile, as the uppermost buried layer where  $S_{\text{nat}_i}$  is below a threshold  $S_h = 2$  or  $S_m = 3$  respectively (or  $S_m = 3.05$  for a NEW type of superior profile):





If 
$$\exists j | Z_j > 0.1$$
 and  $Z_j \le Z_{\text{SUP}}$  and  $S_{\text{nat}_j} \le S_h : Z_h = Z_j - \frac{z_j}{2}$  (154)

If 
$$\exists k | Z_k > 0.1$$
 and  $Z_j \le Z_{\text{SUP}}$  and  $S_{\text{nat}_j} \le S_m$  and  $j \ne k : Z_m = Z_k - \frac{z_k}{2}$  (155)

A first natural avalanche hazard indice  $\mathcal{H}_{nat}$  is defined depending on depths of instability level  $Z_h$  and  $Z_m$ , superior profile height  $Z_{SUP}$  and superior profile type with the following expert rules:

$$\mathcal{H}_{\text{nat}_{1}} = \begin{cases} Z_{h} > 0.8 \begin{cases} \text{NEW} \rightarrow 5 \\ \text{WET} \rightarrow 5 \\ \text{FRO} \rightarrow 3 \end{cases} & \begin{cases} Z_{m} > 0.8 \begin{cases} \text{NEW} \rightarrow 3 \\ \text{WET} \rightarrow 3 \\ \text{FRO} \rightarrow 1 \end{cases} & \begin{cases} \text{NEW} \rightarrow 1 \\ \text{FRO} \rightarrow 0 \end{cases} \\ \text{NEW} \rightarrow 4 \\ \text{FRO} \rightarrow 3 \end{cases} & \begin{cases} \text{NEW} \rightarrow 3 \\ \text{NEW} \rightarrow 3 \end{cases} & \begin{cases} \text{NEW} \rightarrow 3 \\ \text{FRO} \rightarrow 1 \end{cases} \\ \text{NEW} \rightarrow 2 & \mathcal{H}_{\text{nat}_{2}} = \begin{cases} \text{NEW} \rightarrow 3 \\ \text{NEW} \rightarrow 3 \end{cases} & \mathcal{H}_{\text{nat}_{3}} = \begin{cases} \text{NEW} \rightarrow 1 \\ \text{Sup} > 0.4 \end{cases} & \begin{cases} \text{NEW} \rightarrow 1 \\ \text{WET} \rightarrow 1 \\ \text{FRO} \rightarrow 0 \end{cases} \\ \text{NEW} \rightarrow 1 \end{cases} \\ Z_{m} > 0.2 \begin{cases} \text{NEW} \rightarrow 3 \\ \text{WET} \rightarrow 3 \end{cases} & \mathcal{H}_{\text{nat}_{3}} = \begin{cases} \text{NEW} \rightarrow 1 \\ \text{Z}_{\text{SUP}} > 0.2 \end{cases} & \begin{cases} \text{NEW} \rightarrow 1 \\ \text{WET} \rightarrow 1 \\ \text{FRO} \rightarrow 1 \end{cases} \\ Z_{m} > 0 \end{cases} & \begin{cases} \text{NEW} \rightarrow 1 \\ \text{WET} \rightarrow 1 \end{cases} \\ Z_{m} > 0 \end{cases} & \begin{cases} \text{NEW} \rightarrow 1 \\ \text{WET} \rightarrow 1 \end{cases} \\ Z_{m} > 0 \end{cases} & \begin{cases} \text{NEW} \rightarrow 1 \\ \text{WET} \rightarrow 1 \end{cases} \\ Z_{m} > 0 \end{cases} & \begin{cases} \text{NEW} \rightarrow 1 \\ \text{NEW} \rightarrow 1 \end{cases} \\ Z_{m} > 0 \end{cases} & \begin{cases} \text{NEW} \rightarrow 1 \\ \text{NEW} \rightarrow 1 \end{cases} \\ Z_{m} > 0 \end{cases} & \begin{cases} \text{NEW} \rightarrow 1 \\ \text{NEW} \rightarrow 1 \end{cases} \\ Z_{m} > 0 \end{cases} & \begin{cases} \text{NEW} \rightarrow 1 \\ \text{NEW} \rightarrow 1 \end{cases} \\ Z_{m} > 0 \end{cases} & \begin{cases} \text{NEW} \rightarrow 1 \\ \text{NEW} \rightarrow 1 \end{cases} \\ Z_{m} > 0 \end{cases} & \begin{cases} \text{NEW} \rightarrow 1 \\ \text{NEW} \rightarrow 1 \end{cases} \\ Z_{m} > 0 \end{cases} & \begin{cases} \text{NEW} \rightarrow 1 \\ \text{NEW} \rightarrow 1 \end{cases} \\ Z_{m} > 0 \end{cases} & \begin{cases} \text{NEW} \rightarrow 1 \\ \text{NEW} \rightarrow 1 \end{cases} \\ Z_{m} > 0 \end{cases} & \begin{cases} \text{NEW} \rightarrow 1 \\ \text{NEW} \rightarrow 1 \end{cases} \\ Z_{m} > 0 \end{cases} & \begin{cases} \text{NEW} \rightarrow 1 \\ \text{NEW} \rightarrow 1 \end{cases} \\ Z_{m} > 0 \end{cases} & \begin{cases} \text{NEW} \rightarrow 1 \\ \text{NEW} \rightarrow 1 \end{cases} \\ Z_{m} > 0 \end{cases} & \begin{cases} \text{NEW} \rightarrow 1 \\ \text{NEW} \rightarrow 1 \end{cases} \\ Z_{m} > 0 \end{cases} & \begin{cases} \text{NEW} \rightarrow 1 \\ \text{NEW} \rightarrow 1 \end{cases} \\ Z_{m} > 0 \end{cases} & \begin{cases} \text{NEW} \rightarrow 1 \\ \text{NEW} \rightarrow 1 \end{cases} \\ Z_{m} > 0 \end{cases} & \begin{cases} \text{NEW} \rightarrow 1 \\ \text{NEW} \rightarrow 1 \end{cases} \\ Z_{m} > 0 \end{cases} & \begin{cases} \text{NEW} \rightarrow 1 \\ \text{NEW} \rightarrow 1 \end{cases} \\ Z_{m} > 0 \end{cases} & \begin{cases} \text{NEW} \rightarrow 1 \\ \text{NEW} \rightarrow 1 \end{cases} \\ Z_{m} > 0 \end{cases} & \begin{cases} \text{NEW} \rightarrow 1 \\ \text{NEW} \rightarrow 1 \end{cases} \\ Z_{m} > 0 \end{cases} & \begin{cases} \text{NEW} \rightarrow 1 \\ \text{NEW} \rightarrow 1 \end{cases} \\ Z_{m} > 0 \end{cases} & \begin{cases} \text{NEW} \rightarrow 1 \\ \text{NEW} \rightarrow 1 \end{cases} \\ Z_{m} > 0 \end{cases} & \begin{cases} \text{NEW} \rightarrow 1 \\ \text{NEW} \rightarrow 1 \end{cases} \\ Z_{m} > 0 \end{cases} & \begin{cases} \text{NEW} \rightarrow 1 \\ \text{NEW} \rightarrow 1 \end{cases} \\ Z_{m} > 0 \end{cases} & \begin{cases} \text{NEW} \rightarrow 1 \\ \text{NEW} \rightarrow 1 \end{cases} \\ Z_{m} > 0 \end{cases} & \begin{cases} \text{NEW} \rightarrow 1 \\ \text{NEW} \rightarrow 1 \end{cases} \\ Z_{m} > 0 \end{cases} & \begin{cases} \text{NEW} \rightarrow 1 \\ \text{NEW} \rightarrow 1 \end{cases} \\ Z_{m} > 0 \end{cases} & \begin{cases} \text{NEW} \rightarrow 1 \\ \text{NEW} \rightarrow 1 \end{cases} \\ Z_{m} > 0 \end{cases} & \begin{cases} \text{NEW} \rightarrow 1 \\ \text{NEW} \rightarrow 1 \end{cases} \\ Z_{m} > 0 \end{cases} & \begin{cases} \text{NEW} \rightarrow 1 \\ \text{NEW} \rightarrow 1 \end{cases} \\ Z_{m} > 0 \end{cases} & \begin{cases} \text{NEW} \rightarrow 1 \\ \text{NEW} \rightarrow 1 \end{cases} \\ Z_{m} > 0 \end{cases} & \begin{cases} \text{NEW} \rightarrow 1 \\ \text{NEW} \rightarrow 1 \end{cases} \\ Z_{m} > 0 \end{cases} & \begin{cases} \text{NEW}$$

The avalanche situation is then classified in 6 classes following Appendix H2. Finally,  $\mathcal{H}_{\text{nat}}$  is updated by expert rules accounting from the temporal evolution between times  $t - \Delta t_M$  and t following Appendix H3. Note that these rules are sensitive to the MEPRA time step  $\Delta t_M$ , set to 3 hours by Giraud et al. (2002).

#### Accidental triggering

750  $\mathcal{H}_{acc}$  is based on the identification of a slab structure in the snowpack including a slab (layer i and possibly layers above) over a weak layer (layer i + 1). This structure is identified through the following conditions:

$$\begin{cases} \text{MF} \notin \Theta_{i-1} \\ \mathcal{R}_{s_i} > 1.3 \\ \Theta_i \in [\text{DF+RG, RG, RG+FC, DF}] \\ 0.01m \leq Z_i < 1m \\ \Theta_{i+1} \in [\text{FC, DH, FC+DH, PP, PP+DF, DF}] \end{cases}$$

$$(157)$$



755



Similarly to the natural instability levels (Eq. 154 and 155), levels of high accidental instability and moderate accidental instability are looked for among the identified weak layers satisfying Eq. 157:

If 
$$\exists i | \Theta_{i+1} \in [FC, DH, FC+DH]$$
 and  $S_{acc_{i+1}} < 1.5 : Z_h = Z_{i+1} - \frac{z_{i+1}}{2}$  (158)

If 
$$\exists i | \Theta_{i+1} \in [PP, PP+DF, DF]$$
 or  $(\Theta_{i+1} \in [FC, DH, FC+DH] \text{ and } 1.5 \le S_{acc_{i+1}} < 2.5) : Z_m = Z_{i+1} - \frac{z_{i+1}}{2}$  (159)

The accidental hazard indice is finally defined with the following expert rules:

$$\begin{cases}
\text{If } \exists i | \text{ Eq. 158} : \begin{cases}
\text{If } Z_c < 0.01 : \mathcal{H}_{acc} = \max(3, \mathcal{H}_{eq}) \\
\text{else:} \mathcal{H}_{acc} = \max(1, \mathcal{H}_{eq})
\end{cases} \\
\text{If } \exists i | \text{ Eq. 159} : \begin{cases}
\text{If } Z_c < 0.01 : \mathcal{H}_{acc} = \max(2, \mathcal{H}_{eq}) \\
\text{else:} \mathcal{H}_{acc} = \max(1, \mathcal{H}_{eq})
\end{cases} \\
\text{If } \exists i | \text{Eq. 158 or Eq. 159} : \mathcal{H}_{acc} = \max(0, \mathcal{H}_{eq})
\end{cases}$$

where  $\mathcal{H}_{eq}$  is a function of the natural indice  $\mathcal{H}_{nat}$  following Appendix H4 and  $Z_c$  is the cumulated depth of crusts above a 760 layer:

$$Z_{c_h} = \sum_{i} z_i \text{ for } i | \theta_i < 0.2 \text{ and MF} \in \Theta_i \text{ and } Z_i < Z_h \text{ and (PP} \notin \Theta_j \text{ and DF} \notin \Theta_j \forall j \in [1, i-1])$$

$$\tag{161}$$

$$Z_{c_m} = \sum_i z_i \text{ for } i | \theta_i < 0.2 \text{ and MF} \in \Theta_i \text{ and } Z_i < Z_m \text{ and } (PP \notin \Theta_j \text{ and DF} \notin \Theta_j \forall j \in [1, i-1])$$

$$(162)$$

Note that only one value for  $Z_h$  and  $Z_m$  is provided in the diagnoses output file. If  $\mathcal{H}_{acc} = \mathcal{H}_{eq}$  in Eq. 160, they correspond to Eq. 154 and 155, otherwise they correspond to Eq. 158 and 159.

#### 765 4 Technical features

775

### 4.1 Implemented simulation geometries

All variables in the code are defined as vectors including at least a spatial dimension, and when necessary the snow layers as second dimension. The implication in terms of numerical efficiency of loops in the code is described in detail in Appendix I. This 1D spatial dimension allows to use either discontinuous collections of points or regular grids for simulations. A typical example of a collection of points is the semi-distributed geometry based on homogeneous massifs and topographic classes which has been used for more than 30 years for operational simulations in French mountains and in the associated 66-year reanalysis (Vernay et al., 2022). Gridded experiments can also be easily defined through the standard SURFEX tools which include regular latitude-longitude coordinates or various conformal projections. Over the French territory, the Lambert 93 projection is recommended as a national standard for gridded simulations (i.e. Deschamps-Berger et al., 2022; Haddjeri et al., 2024).



780

785

790

800

805



### 4.2 Parallelization and numerical efficiency

In the general case where Crocus is not coupled with a snow transport model, the processes currently represented by the model do not involve any mass or energy exchange between the snowpacks of the different spatial units. Therefore, parallelization can be very efficiently applied without any need of communication between processors in the physical model. A distributed memory parallelism has be chosen for that purpose in the offline driver of the SURFEX platform based on MPI libraries. However, the standard SURFEX Input-Output routines are not currently parallelized. Therefore, all input and output data are forwarded to a single processor. As a result, over large domains, the efficiency of parallel computing is currently limited by the saturation of the IO processor, in all cases but especially when the user chooses to output a large number of diagnoses at high temporal resolution. The XIOS library (Yepes-Arbós et al., 2022) implemented in SURFEX is designed to deal with this issue but the implementation of its compatibility with Crocus variables is still in progress. The numerical cost of the model itself depends on the number of layers created by the model. Therefore, it can significantly vary from a domain to another and from a season to another, depending on the number of layers of each simulated snowpack which highly depends on total snow depth.

To give the magnitude of the numerical cost, Table 2 presents the computing time of a 1-year simulation over 4471 simulation points in the French Alps. It must be noticed than the numerical cost of Crocus is very low compared to the cost of IO, providing a clear guidance for priorities in future optimizations. Crocus also only represents 26% of the computation time of the ISBA land surface model itself. Even in an alpine region, the variability of snow cover in time and space makes the snow component relatively cheap with a similar level of complexity compared to the 20-layer soil model running all year over all points. As a result, the numerical cost of Crocus  $(0.3 \text{ cores} \times \text{s per year and simulation point for this example})$  can not be considered as a valid argument to prefer simpler models in large scale applications of LSM or coupled applications.

Considering the partitioning of numerical costs between the different subroutines within Crocus, it appears clearly that the complexity of the discretization rules emphasized by Eq. 11 has a significant impact as this routine represents 33% of the whole model cost. The metamorphism routine is the second most contributing routine although its cost has been considerably reduced compared to previous versions (Carmagnola et al., 2014). The numerical core of the model solving heat diffusion and energy balance is very efficient contributing to less than 6% of the cost. Numerical optimizations are still possible in some routines representing an unjustified contribution compared to their low complexity (e.g. thermal conductivity). Possible optimizations may concern the management of loops (cf. Appendix I) or some iterative calls to scalar functions in external modules.





**Table 2.** Numerical cost of a 1-year simulation from 1 Aug 2023 to 1 Aug 2024 over 4471 simulation points corresponding to the French Alps domain described in Vernay et al. (2022) and the default physical options as in Lafaysse et al. (2017). The code was compiled with Intel®MPI library version 2018.5.274 and O2 optimization level. Output are minimized (reduced to daily snow depth), otherwise the total execution time would be highly increased. The simulation is performed using 80 MPI threads on 80 physical cores on one 2.2 GHz AMD©Rome computing node constituted by 2 sockets of 64 cores. Results are presented in cores × s. The real elapsed time for this simulation in this architecture is 449 s.

	Time (cores $\times$ s)	Ratio with Crocus time (%)
SURFEX run	35964	2480
IO reading and communications	29390	2026
ISBA land surface model	5513	380
Crocus snow model	1450	100
Snowfall and vertical discretization	491	33.4
Metamorphism	173	11.9
Absorption of solar radiation	162	11.2
Compaction	95	6.6
Regridding (aggregation / dissociation)	77	5.3
Heat diffusion (Eq. 106-107)	64	4.4
Thermal conductivity	61	4.2
Percolation and refreezing	58	4.0
Melting	30	2.1
Aggregation of vanishing layers	27	1.9
Drift	25	1.7
Diagnostic of energy fluxes	23	1.6
Energy balance (Eq. 101-105)	20	1.4

#### 4.3 Running environment and visualization

Beyond the FORTRAN code itself, most offline applications of the model have to deal with the management of input and output files to perform various experiments with different forcing files, namelists, or binaries, different setting of initial and final simulation dates, standard initialization procedures (soil spinup, etc.). Therefore, a common running environment of the model in Python is provided in an independent package called snowtools coming with a full user documentation and an interface for technical support (cf. Code availability section).

Crocus scalar diagnoses can be easily processed by any scientific plotting software supporting netcdf format as input. However, the irregular vertical discretization of the snowpack model complexifies the visualization of the simulated profiles. A simple software provided in the snowtools package is able to combine the variables to plot with the depth of each layer to





produce detailed instantaneous stratigraphies or temporal evolution of a given stratified variable. For spatialized simulations, plotting the spatial variability of the vertical structure of the snowpack is still a challenge.

#### 4.4 Externalization

820 Although the reference implementation of Crocus is within the SURFEX land surface modelling platform (Masson et al., 2013), there is an increasing need of being able to couple Crocus with other land surface schemes. For that purpose, an externalized version of the source codes is now available as an independent Fortran library that can be compiled alone and called by other land surface models (cf. Code availability section). It includes all the processes described in this paper except the coupling with external components (snow transport modules and MEB vegetation module). Thus, Crocus is also now fully integrated within the SVS2 land surface system (Vionnet et al., 2025). It was also recently implemented within the Flexible Snow Model (FSM2, 825 Essery et al., 2025) allowing the coupling with its more detailed vegetation model (Mazzotti et al., 2024). SURFEX, SVS2 and FSM2 rely on a unique code repository of Crocus that guarantees the long-term maintenance and convergence of the code and therefore facilitates the contributions of different research groups to the model developments. For instance, as mentioned for several processes in Section 2, various new parameterizations better suited for Arctic snow were recently proposed within the SVS2 implementation (Woolley et al., 2024; Vionnet et al., 2025). Thanks to this method, these developments will integrate 830 soon a future release and be beneficial for SURFEX and FSM2 applications. Therefore, we strongly encourage other groups that have copied the code within their specific applications to try to converge towards this unique code version. This includes the implementation of Crocus within WRF-Hydro (Eidhammer et al., 2021), the coupling of Crocus with Noah LSM (Navari et al., 2024), the MAR regional climate model largely used for polar regions (Fettweis et al., 2017; Agosta et al., 2019) and 835 from which the Crocus version has diverged for a long time (Gallée et al., 2001), and even applications which have only extracted specific routines such as the CryoGrid permafrost model (Zweigel et al., 2021).

### 5 Review of evaluations and scientific applications

## 5.1 With a local scale meteorological forcing

840

845

The most direct evaluations of the model are performed on well-instrumented sites allowing to minimize errors in the meteorological forcing and in the observations used for evaluation. Model skills have been documented in detail at the Col de Porte experimental site (Morin et al., 2012; Lejeune et al., 2019), a mid-elevation meadow in French Alps. The very first evaluations of Brun et al. (1989) present qualitative evaluations of surface and internal temperature, snow depth, and basal runoff during short periods of the winter 1986-1987. Brun et al. (1992) extended the evaluations to the whole winter 1988-1989 on the same variables as well as a subjective comparison between the simulated stratigraphies and weekly observed profiles. Extensions of the evaluation period were successively published by Essery et al. (1999); Boone and Etchevers (2001); Strasser et al. (2002); Etchevers et al. (2004); Avanzi et al. (2016) in the context of model intercomparisons, and also by Vionnet et al. (2012). These papers also included evaluations of albedo and SWE. Lafaysse et al. (2017) extended these evaluations to all multiphysics op-



850

855

860

865

870

875

880



tions and accounted for observation uncertainties usually ignored in previous papers. The scores of the model on these variables have not significantly changed since the first years of development. Complementary evaluations of density and microstructure profiles are provided by Morin et al. (2013) and Carmagnola et al. (2014). However, quantitative evaluation of internal snow properties is still a methodological challenge due to frequent discreapancies between numerical and observed snow layers that can easily lead to double penalty issues. This can only be partly solved with vertical adjustments algorithms (Viallon-Galinier et al., 2020; Herla et al., 2021) or with an expert layer tracking (Calonne et al., 2020).

More challenging evaluations include a variety of environmental and climate conditions. Evaluations driven by local meteorological observations were performed in Svalbard (Bruland et al., 2001; Sauter and Obleitner, 2015), at the high elevation site of Weissflujoch, Switzerland (Etchevers et al., 2004), over tropical glaciers and moraines in Bolivia (Leieune et al., 2007) and Ecuador (Wagnon et al., 2009), at Sherbrooke University, Quebec (Langlois, et al., 2009), at Torgnon, Italy (Di Mauro et al., 2019). The most comprehensive evaluations in terms of number of sites and years were performed on 10 contrasted sites through the Earth System Model-Snow Model Intercomparison Project (ESM-SnowMIP, Krinner et al., 2018; Menard et al., 2021) and with a few more sites for albedo evaluations by Gaillard et al. (2025). Typical errors on SWE, density, albedo, surface temperature and ground temperature are in the range of state-of-the art snow models but similar overall skill can be obtained by simpler models on these variables. A cold bias in surface temperature was identified in these experiments (Menard et al., 2021). It may be attributed to the parameterization of turbulent fluxes which are suspected to be underestimated in the standard option but this bias can be removed with the other options (Martin and Lejeune, 1998; Lafaysse et al., 2017). This assumption was also recently supported by more detailed evaluations of all components of the energy balance including eddy-covariance observations of turbulent fluxes in Québec (Lackner et al., 2022) and in Finnish peatlands (Nousu et al., 2024). However, it is especially important to be aware that the equifinality of the different empirical parameterizations and the complex compromises in multivariate evaluations (Essery et al., 2013; Lafaysse et al., 2017) should encourage future attempts to improve processes representations to be tested robustly with ensemble multiphysics simulations and multivariate evaluations (e.g. Woolley et al., 2024).

## 5.2 With a regional scale meteorological forcing

In many other applications, the model was forced by meteorological reanalyses (e.g. Durand et al., 2009; Brun et al., 2013; Vernay et al., 2022) or short-term forecasts (e.g. Vionnet et al., 2016; Skaugen et al., 2018) or a combination of both (Vionnet et al., 2022). Although these studies often include snow depth evaluations on a large range of stations, in this case the resulting modelling errors of any snow model are dominated by errors in the meteorological forcing (Raleigh et al., 2015; Günther et al., 2019) and Crocus does not make an exception (Quéno et al., 2017; Réveillet et al., 2018; Vionnet et al., 2019; Gouttevin et al., 2022). Thus, the attribution of some limitations of the simulation results to the snowpack model itself is difficult. However, this is sometimes the only possible method for the assessment of some specific processes. For instance, the simulated concentrations of Light-Absorbing Particles (Tuzet et al., 2017), the spectral reflectances from the TARTES optical scheme (Cluzet et al., 2020), the blowing snow fluxes (Vionnet et al., 2018; Baron et al., 2024) were only evaluated in such context. The same applies to the ability of the model to reproduce the properties of polar snow (e.g. Dang et al., 1997; Libois et al.,



885

890

895

905

910



2015; Barrere et al., 2017; Vionnet et al., 2025), the spatial distribution of snow conditions depending on topography (Revuelto et al., 2018; Skaugen et al., 2018; Haddjeri et al., 2024), or its adequation with complex remote sensing signals (Veyssière et al., 2019). Similar simulation frameworks are used to investigate the suitability of the model for hydrological diagnoses (e.g. Strasser and Etchevers, 2005), glacier mass balance (e.g. Réveillet et al., 2018; Roussel et al., 2025) or avalanche activity (Eckert et al., 2010; Viallon-Galinier et al., 2022).

Based on the confidence provided by these available evaluations, the model is used for various purposes including the understanding of internal physical processes (e.g. Domine et al., 2013; Dick et al., 2023; Roussel et al., 2024), the quantification of contributions to the energy balance (e.g. Tuzet et al., 2020; Dumont et al., 2020; Reveillet et al., 2022, for light-absorbing particles), the monitoring of the long-term climatology of extreme snow loads (Le Roux et al., 2022) or avalanche activity (Reuter et al., 2022, 2025), the investigation of the links between snow cover and alpine ecosystems evolutions (Nicoud et al., 2025), and climate projections of natural snow conditions (Rousselot et al., 2012; Verfaillie et al., 2018), avalanche hazard (Castebrunet et al., 2014) and ski resorts operating conditions (Spandre et al., 2019; Morin et al., 2021; François et al., 2023). The development efforts were originally dedicated to operational avalanche hazard forecasting (Durand et al., 1999). However, after about 30 years of operation, the model did not become the main tool of the forecasters because this application is especially sensitive to uncertainties (Vernay et al., 2015) among numerous other challenges as reviewed by Morin et al. (2020). The statistical post-processing of simulations through various techniques of artifical intelligence (Nousu et al., 2019; Evin et al., 2021; Viallon-Galinier et al., 2023) might provide guidance to improve the practical interest of such simulations for operational applications including avalanche forecasting.

#### 900 5.3 Towards data assimilation

The long memory of the snowpack on the past meteorological conditions and past snow processes imply that all sources of modelling errors tend to cumulate all along the season. Therefore, there is a large avenue for data assimilation algorithms in order to improve the initial states of the simulations (Largeron et al., 2020). However, the variable dimension size of the Crocus state vector and the high non-linearities in the simulated processes make especially challenging the application to this model of a number of data assimilation algorithms. Therefore, most recent efforts intended to apply different variants of the Particle Filter to weight the members of an ensemble of simulations according to their distance to some observations (Charrois et al., 2016; Cluzet et al., 2021, 2022; Deschamps-Berger et al., 2022). The different options of the algorithm are described in Cluzet et al. (2021) and the implemented variables are snow depth and optical reflectance, for which the observation operator is simply the identity function as these variables are direct diagnoses of the model. The assimilation of optical reflectance is however constrained by the retrieval errors of this variable in complex terrain (Cluzet et al., 2020) that still exceed the requirements for an efficient data assimilation (Revuelto et al., 2021). Large efforts are planned in a near future to extend these possibilities. For some common satellite observations (e.g. snow cover fraction, wet snow fraction), this will require the development of appropriate observation operators from the simulated state variables.





#### 6 Conclusion

915

920

925

This article provides a comprehensive description of all equations implemented in version 3.0 of the Crocus snow model. It gathers the recent developments of the last 13 years in a unique publication: (i) modelling of Light-Absorbing Particles, (ii) coupling with the TARTES optical scheme, (iii) modelling of ice layers due to freezing rain, (iv) coupling with the MEB big-leaf vegetation scheme, (v) snow management practices on ski slopes, (vi) coupling with blowing snow schemes, (vii) multiphysics parameterizations for most processes and (viii) diagnosis of the snowpack mechanical stability. In addition, this article documents a number of equations implemented in previous code versions but never published in the literature. It must be mentioned that during the preparation of this publication, a considerable number of errors or discreapancies between the code and previous publications were identified and corrected. This is in full agreement with the main conclusions of Menard et al. (2021) suggesting that insufficient model documentation is a key factor for the difficulty to improve snow modelling in the last decades. This comprehensive documentation is expected to help snow scientists to better interpret results based on this model. This is especially important in the context of an in-progress extension of Crocus applications in several land surface schemes. This documentation effort is also expected to help the snow modelling community improve numerical models in the future thanks to an accurate knowledge of the existing parameterizations and numerical difficulties. Despite our best efforts to minimize errors, previous literature and experience suggest that some errors may still remain in this publication. In such a case, corrigenda will be associated to this publication in due course.

### 930 Appendix A: Attractor profile in layering

The attractor profile  $z_i^*$  used in Equation 11 depends only on the total snow depth Z and number of layers N. Let's define  $N^*$  and  $Z^*$  by:

$$\begin{cases} \text{if } Z > 20 \text{ and } N > \frac{N_{\text{max}}}{3} + 2 \begin{cases} N^* = N - \frac{N + N_{\text{max}}}{6} \\ Z^* = 3 \end{cases} \end{cases}$$

$$\begin{cases} N^* = N \\ Z^* = Z \end{cases} \tag{A1}$$





Then, the attractor profile is defined by:

$$\begin{cases} z_1^* = \min(0.01, \frac{Z^*}{N^*}) \\ z_2^* = \min(0.0125, \frac{Z^*}{N^*}) \\ z_3^* = \min(0.03, \frac{Z^*}{N^*}) \text{ if } N^* > 3 \\ z_4^* = \min(0.04, \frac{Z^*}{N^*}) \text{ if } N^* > 4 \\ z_5^* = \min(0.05, \frac{Z^*}{N^*}) \text{ if } N^* > 5 \\ z_6^* = \max(0.07, \min(\frac{Z^*}{N^*}, 0.5)) \text{ if } N^* > 6 \\ z_7^* = \max(0.07, \min(\frac{Z^*}{N^*}, 1.)) \text{ if } N^* > 7 \\ z_8^* = \max(0.07, \min(\frac{Z^*}{N^*}, 2.)) \text{ if } N^* > 8 \\ z_9^* = \max(0.07, \min(\frac{Z^*}{N^*}, 4.)) \text{ if } N^* > 9 \\ z_{10}^* = \max(0.07, \min(\frac{Z^*}{N^*}, 4.)) \text{ if } N^* > 10 \\ z_i^* = \max(0.07, \min(\frac{Z}{N^*}, 1.)) \text{ if } N^* > 11 \\ z_i^* = (i - N^*) \frac{2(Z - 3)}{(N - N^*)(N - N^* + 1)} \forall i \in [N^* + 1, N] \text{ if } Z > 20 \\ z_N^* = \min(0.02, \frac{Z}{N^*}) \\ \text{if } Z > 3 \text{ and } N^* > 10 \begin{cases} z_{N-1}^* = 0.66z_N^* + 0.34z_{N-3}^* \\ z_{N-2}^* = 0.34z_N^* + 0.66z_{N-3}^* \end{cases} \text{ instead of previous definitions} \end{cases}$$

It extends the definition of Vionnet et al. (2012) in order to converge towards a profile allowing a numerically stable resolution of heat diffusion for thick snowpacks and glacier applications.

#### Appendix B: Adjustment of wind speed

Several parameterizations of the model are formulated with a wind speed at a specific height corresponding to the experimental conditions but might not correspond to the reference height of the forcing variable. In these cases, the wind speed  $U_z$  (ms<sup>-1</sup>) at height z (m) is adjusted assuming a logarithmic profile in the surface boundary layer based following:

$$U_z = U \frac{\ln\left(\frac{z}{z_0}\right)}{\ln\left(\frac{z_u}{z_0}\right)} \tag{B1}$$

where  $z_0$  is the surface roughness length (m).





#### Appendix C: Growth of faceted crystals in B21 metamorphism parameterizations

The growth of faceted crystals in B21 parameterization (Eq. 46) is based on cold room experiments from Marbouty (1980). These functions already published by Vionnet et al. (2012) are reminded here for the comprehensiveness of this paper. f, g, h and  $\Phi$  are dimensionless functions from 0 to 1 given by:

$$f(\theta_i) = \begin{cases} 0 & \text{if } \theta_i < -40 \text{ °C} \\ 0.011 \times (\theta_i + 40) & \text{if } -40 \le \theta_i < -22 \text{ °C} \\ 0.2 + 0.05 \times (\theta_i + 22) & \text{if } -22 \le \theta_i < -6 \text{ °C} \\ 0.7 - 0.05\theta_i & \text{otherwise} \end{cases}$$
(C1)

950 
$$h(\rho_i) = \begin{cases} 1. & \text{if } \rho_i < 150 \text{ kg m}^{-3} \\ 1 - 0.004 \times (\rho_i - 150) & \text{if } 150 < \rho_i < 400 \text{ kg m}^{-3} \\ 0. & \text{otherwise} \end{cases}$$
 (C2)

$$g(\mathcal{G}_i) = \begin{cases} 0. & \text{if } \mathcal{G}_i < 15 \,\mathrm{K\,m^{-1}} \\ 0.01 \times (\mathcal{G}_i - 15) & \text{if } 15 \le \mathcal{G}_i < 25 \,\mathrm{K\,m^{-1}} \\ 0.1 + 0.037 \times (\mathcal{G}_i - 25) & \text{if } 25 \le \mathcal{G}_i < 40 \,\mathrm{K\,m^{-1}} \\ 0.65 + 0.02 \times (\mathcal{G}_i - 40) & \text{if } 40 \le \mathcal{G}_i < 50 \,\mathrm{K\,m^{-1}} \\ 0.85 + 0.0075 \times (\mathcal{G}_i - 50) & \text{if } 50 \le \mathcal{G}_i < 70 \,\mathrm{K\,m^{-1}} \\ 1. & \text{otherwise} \end{cases}$$
(C3)

$$\Phi = 1.0417.10^{-9} \,\mathrm{m \, s^{-1}} \tag{C4}$$

#### Appendix D: New formalism of metamorphism

960

The translation of the original metamorphism parameterizations in terms of dendricity, sphericity and size from Brun et al. (1992) to the new formalism of Carmagnola et al. (2014) in terms of optical diameter and sphericity, was based on the original expression of the optical diameter  $d_i$  as a function of dendricity  $\delta_i$ , sphericity  $S_i$  and grain size  $g_{s_i}$  (as already published in Eq. 13 of Vionnet et al. (2012)):

$$d_i = \begin{cases} 10^{-4} \left[ \delta_i + (1 - \delta_i) \left( 4 - S_i \right) \right] & \text{if } \delta_i > 0 \text{ (dendritic case)} \\ g_{s_i} \times S_i + (1 - S_i) \times \max \left( 4.10^{-4}, \frac{g_{s_i}}{2} \right) & \text{if } \delta_i = 0 \text{ (non-dendritic case)} \end{cases}$$
 (D1)

This relationship has always been required to compute the absorption of solar radiation from the equations of Section 2.4.9. In the dendritic case, the transformation  $(S_i, \delta_i) \Rightarrow (S_i, d_i)$  is bijective. The inversion of this relationship lead to:



970

980

985



$$\delta_i = \frac{10^4 \times d_i - 4 + S_i}{S_i - 3} \text{ if } d_i < 10^{-4} (4 - S_i)$$
(D2)

and the new evolution law of  $d_i$  was obtained by Carmagnola et al. (2014) using

$$\frac{dd_i}{dt} = \frac{\partial d_i}{\partial \delta_i} \frac{d\delta_i}{dt} + \frac{\partial d_i}{\partial S_i} \frac{dS_i}{dt}$$
(D3)

Thus, the combination of Eq. D3 with the equations from Table 1 of Vionnet et al. (2012) provides the second line of Eq. 46 in this paper (which is close to the right column of Table 2 in Carmagnola et al. (2014) after typo corrections).

In the non-dendritic case, the transformation  $(S_i, g_{s_i}) \Rightarrow (S_i, d_i)$  is not bijective. When  $S_i = 0$ , Eq. D1 gives  $d_i = 4 \times 10^{-4} \forall g_{s_i} \in [3 \times 10^{-4}, 8 \times 10^{-4}]$ . As a result, the metamorphism functions from Table 1 of Vionnet et al. (2012) can not be reproduced in the space  $(S_i, d_i)$  when  $S_i = 0$  (e.g. depth hoar). Then, Eq. D1 is discontinuous at the limit between dendritic case and non-dendritic case. Indeed, the limit of the dendritic case gives  $\lim_{\delta_i \to 0} d_i = 10^{-4} (4 - S_i)$ . When combined with the non dendritic case, this would result in  $g_{s_i} = 3 \times 10^{-4}$  while the initial value of  $g_{s_i}$  was actually higher for non-spheric particles in Brun et al. (1992):  $g_{s_i} = 10^{-4} (4 - s_i)$ . In the other cases, the inversion of Eq. D1 can provide a relationship for  $g_{s_i}$  as a function of  $d_i$  and  $S_i$ :

$$g_{s_i} = \begin{cases} 2\frac{d_i}{S_i + 1} & \text{if } d_i \ge 4 \times 10^{-4}(S_i + 1) \\ \frac{d_i - 4 \times 10^{-4}(1 - S_i)}{S_i} & \text{if } d_i < 4 \times 10^{-4}(S_i + 1) \end{cases}$$
(D4)

Eq. D4 is actually more complex than Eq. 3 of Carmagnola et al. (2014) which was an incorrect simplification corresponding only to the initialization of grain size at the dendritic - non-dendritic transition. It is also not defined when  $S_i = 0$  and  $d_i < 4 \times 10^{-4}(S_i + 1)$ . Last, the derivation of an evolution law for optical diameter was obtained by Carmagnola et al. (2014) in the non-dendritic case (left column of their Table 2) by considering only  $\frac{dd_i}{dt} = \frac{\partial d_i}{\partial S_i} \frac{dS_i}{dt}$ . This is actually inconsistent with the original formalism in the non-dendritic case as it ignores the term  $\frac{\partial d_i}{\partial g_{s_i}} \frac{dg_{s_i}}{dt}$ . Ignoring this term may be convenient to avoid the problems mentioned above but it affects the metamorphism of faceted crystals and depth hoar without any scientific justification whereas they are the most critical snow types for further analyses in terms of mechanical stability. Furthermore, a number of parameterizations of other processes and diagnoses in the code were also affected by the incorrect simplification of Eq. D4. The original difficulty of this translation of formalisms comes from the fact that Eq. D1 is neither bijective nor continuous. However, we considered that it is better to adapt this unpublished formula and preserve as much as possible the metamorphism laws, the parameterizations of other processes and the diagnoses relying on microstructure properties. A new metamorphism option (B21) has therefore been defined, replacing the expression from Carmagnola et al. (2014) by:

$$d_i = g_{s_i} \times S_i + (1 - S_i) \frac{4 \times 10^{-4} + g_{s_i}}{2} \text{ if } \delta_i = 0 \text{ (non-dendritic case)}$$
(D5)

This allows to replace Eq. D4 by:



995



$$g_{s_i} = 2\frac{d_i - 2 \times 10^{-4} (1 - S_i)}{1 + S_i} \tag{D6}$$

This way, the evolution of optical diameter in the non dendritic case can be obtained by:

$$\frac{dd_i}{dt} = \frac{\partial d_i}{\partial g_{s_i}} \frac{dg_{s_i}}{dt} + \frac{\partial d_i}{\partial S_i} \frac{dS_i}{dt}$$
(D7)

$$= \frac{1+S_i}{2} \frac{dg_{s_i}}{dt} + (\frac{g_{s_i}}{2} - 2 \times 10^{-4}) \frac{dS_i}{dt}$$
(D8)

$$= \frac{1+S_i}{2} \frac{dg_{s_i}}{dt} + \frac{d_i - 4 \times 10^{-4}}{1+S_i} \frac{dS_i}{dt}$$
 (D9)

The main advantage of this new formalism is that it respects the original evolution law of  $\frac{dg_{s_i}}{dt}$  as published by Vionnet et al. (2012). As a result, all parameterizations and diagnostics calibrated in the original formalism can still considered to be valid in this new formalism. Finally, the first line of Eq. 46 corresponds to the combination of Eq. D9 and Table 1 of Vionnet et al. (2012). Complementary analyses by Baron (2023) have shown that the obtained microstructure properties of B21 option are closer to the original formalism of Vionnet et al. (2012) than the implementation of Carmagnola et al. (2014) (also referred as C13 in Lafaysse et al. (2017). This is especially true when this parameterization is combined with the snow drift options. More details are available in Baron (2023).

Similarly for wet metamorphism, the combination of Eq. D9 and Table 2 of Vionnet et al. (2012) provides Eq. 51 of this paper. The transformation of wet metamorphism laws in this new formalism were neither provided in Carmagnola et al. (2014) nor correctly implemented.

#### Appendix E: Evolution of optical diameter during snow drift

The evolution of microstructure properties was parameterized in terms of dendricity  $\delta_i$ , sphericity  $S_i$  and grain size  $g_{s_i}$  from simple evolution laws provided in Table 3 of Vionnet et al. (2012) in which sign errors must be accounted for in the evolution of  $\delta_i$  and  $g_{s_i}$ :

$$\frac{d\delta_i}{dt} = \frac{-\delta_i}{2\tau_{\text{DRIFT}}} \text{if } \delta_i > 0 \text{ (dendritic case)}$$
 (E1)

$$\frac{dg_{s_i}}{dt} = \frac{-5 \times 10^{-4}}{\tau_{\text{DRIFT}}} \text{if } \delta_i = 0 \text{ (non-dendritic case)}$$
 (E2)

$$\frac{dS_i}{dt} = \frac{1 - S_i}{\tau_{\text{DRIFT}}} \tag{E3}$$

In the dendritic case, the evolution of the optical diameter  $d_i$  is obtained by the introduction of Eq. E1 and E3 in Eq. D3 and computing  $\frac{\partial d_i}{\partial S_i}$  and  $\frac{\partial d_i}{\partial S_i}$  from the first line of Eq. D1. In the non-dendritic case, the evolution of the optical diameter  $d_i$  is





obtained by the introduction of Eq. E2 and E3 in Eq. D7 and computing  $\frac{\partial d_i}{\partial g_{s_i}}$  and  $\frac{\partial d_i}{\partial S_i}$  from Eq. D5. Finally:

$$\begin{cases}
\frac{dd_i}{dt} = 10^{-4} (S_i - 3) \times \left(\frac{-\delta_i}{2\tau_{\text{DRIFT}}}\right) + 10^{-4} (\delta_i - 1) \times \frac{1 - S_i}{\tau_{\text{DRIFT}}} & \text{if } d_i < 10^{-4} (4 - S_i) \\
\frac{dd_i}{dt} = \frac{S_i + 1}{2} \times \frac{-5 \times 10^{-4}}{\tau_{\text{DRIFT}}} + \frac{g_{s_i} - 4 \times 10^{-4}}{2} \times \frac{1 - S_i}{\tau_{\text{DRIFT}}} & \text{if } d_i > = 10^{-4} (4 - S_i)
\end{cases}$$
(E4)

The first line can be slightly simplified and Eq. D6 introduced in the second line to finally obtain the equivalent discrete 1015 formulation of Eq. 67.

#### Appendix F: Thermodynamical functions

The air volumetric mass  $\rho_a$  is obtained by:

$$\rho_a = \frac{P_s}{R_a T_a \left(1 + \left(\frac{R_v}{R_a} - 1\right) q_a\right) + g \times z_a} \tag{F1}$$

The Exner functions at surface and at the forcing level are defined by:

1020 
$$\Pi_a = \left(\frac{P_a}{P_0}\right)^{\frac{R_a}{c_P}} \tag{F2}$$

$$\Pi_s = \left(\frac{P_s}{P_0}\right)^{\frac{R_a}{c_P}} \tag{F3}$$

where  $P_0 = 10^5 \text{Pa}$  and the atmospheric pressure at forcing level  $P_a$  is obtained from hydrostatism:

$$P_a = P_s - \rho_a g z_a \tag{F4}$$

The saturation specific humidity at temperature T is obtained by:

1025 
$$q_{sat}(T) = \frac{\frac{R_a}{R_v} \times \frac{e_{sat}(T)}{P_s}}{1 + \left(\frac{R_a}{R_v} - 1\right) \frac{e_{sat}(T)}{P_s}}$$
(F5)

where the water vapor partial pressure at saturation  $e_{sat}(T)$  is obtained from the Clapeyron formula:

$$\begin{cases}
\operatorname{If} T \ge T_0 & e_{sat}(T) = \exp\left(\alpha_w - \frac{\beta_w}{T} - \gamma_w \ln(T)\right) \\
\operatorname{If} T < T_0 & e_{sat}(T) = \exp\left(\alpha_I - \frac{\beta_I}{T} - \gamma_I \ln(T)\right)
\end{cases}$$
(F6)





where  $\gamma_w = \frac{c_W - c_{P_v}}{R_v}$ (F7)

1030

$$\beta_w = \frac{L_v}{R_v} + \gamma_w T_0 \tag{F8}$$

$$\alpha_w = \ln(e_{sat}(T_0)) + \frac{\beta_w}{T_0} + \gamma_w \ln(T_0)$$
(F9)

$$\gamma_I = \frac{c_I - c_{P_v}}{R_v} \tag{F10}$$

$$\beta_I = \frac{L_s}{R_u} + \gamma_I T_0 \tag{F11}$$

$$\alpha_I = \ln(e_{sat}(T_0)) + \frac{\beta_I}{T_0} + \gamma_I \ln(T_0) \tag{F12}$$

1035

$$e_{sat}(T_0) = 611.14 \,\mathrm{Pa}$$
 (F13)

The derivation  $\frac{\partial q_{sat}(T)}{\partial T}$  is obtained by:

$$\frac{\partial q_{sat}(T)}{\partial T} = \frac{\partial e_{sat}(T)}{\partial T} q_{sat}(T) \times \frac{1}{1 + \frac{\frac{R_a}{R_v} - 1}{1 + \frac{R_a}{R} \left(\frac{1}{a - 1/T}\right) - 1}}$$
(F14)

where  $\frac{\partial e_{sat}(T)}{\partial T} = \frac{\beta_w}{T^2} - \frac{\gamma_w}{T}$ (F15)

The Richardson number is computed by:

1040

$$Ri = g\cos\gamma z_u^2 \frac{\theta_{v_a} - \theta_{v_s}}{0.5(\theta_{v_a} + \theta_{v_s})\max(U, U_{th})^2 z_a}$$
(F16)

where 
$$\theta_{v_a} = \frac{T_a}{\Pi_a} \left( 1 + \left( \frac{R_v}{R_a} - 1 \right) q_a \right)$$
 (F17)

$$\theta_{v_s} = \frac{T_1}{\Pi_s} \left( 1 + \left( \frac{R_v}{R_a} - 1 \right) q_{sat}(T_1) \right) \tag{F18}$$

(F19)

The wet bulb temperature  $T_w^*$  (°C) is computed by Eq. F20:

1045 
$$T_w^* = \frac{\gamma \cdot T_a^* + \frac{\partial e_{sat}(T)}{\partial T} \cdot T_d^*}{\gamma + \frac{\partial e_{sat}(T)}{\partial T}}$$
(F20)

where the slope of the saturation vapor pressure curve  $\frac{\partial e_{sat}(T)}{\partial T}$  is given by Eq. F15; the dew point temperature  $T_d^*$  (°C) is parameterized by

$$T_d^* = [116.9 + 237.3ln(e)]/[16.78 - ln(e)]$$
 (F21)

and the psychrometric constant  $\gamma$  (in kPa K<sup>-1</sup>) is obtained by:

$$1050 \quad \gamma = \frac{c_{P_m} \cdot P_s}{0.622 \cdot L_v} \tag{F22}$$

where  $c_{P_m}$  is the specific heat capacity of moist air at constant pressure (in kJ kg<sup>-1</sup>  $^{\circ}$ C<sup>-1</sup>).





### Appendix G: Functions in the parameterization of shear resistance

$$\begin{cases} \text{If } S_i > 0.8 \text{ and } h_i \in [3,5]: \quad \mathcal{C}_1(d_i,S_i) = 1.05 \\ \\ \text{else:} \end{cases} \qquad \mathcal{C}_1(d_i,S_i) = \begin{cases} 0.45 + 0.7S_i & \text{if } S_i < 0.25 \\ 0.625 + 1.0 \cdot (S_i - 0.25) & \text{if } 0.25 \le S_i < 0.5 \\ 0.875 + 0.6 \cdot (S_i - 0.5) & \text{if } 0.5 \le S_i < 0.75 \\ 1.025 + 0.5 \cdot (S_i - 0.75) & \text{if } 0.75 \le S_i \end{cases} \tag{G1}$$

$$\mathcal{C}_{2}(d_{i}, S_{i}) = \begin{cases}
1 - 0.4\delta_{i} & \text{if } \delta_{i} < 0.25 \\
0.9 - 0.4 \cdot (\delta_{i} - 0.25) & \text{if } 0.25 \leq \delta_{i} < 0.5 \\
0.8 - 0.8 \cdot (\delta_{i} - 0.5) & \text{if } 0.5 \leq \delta_{i} < 0.75 \\
0.6 - 0.6 \cdot (\delta_{i} - 0.75) & \text{if } 0.75 \leq \delta_{i}
\end{cases} \quad \text{where } \delta_{i} = \frac{d_{i} \times 10^{4} - 4 + S_{i}}{S_{i} - 3} \tag{G2}$$

$$\begin{cases} \text{If } d_i \leq (4-S_i) \times 10^{-4}: \quad \mathcal{C}_3(d_i,S_i) = 1 \\ \text{else:} \begin{cases} \text{If } g_{s_i}(d_i,S_i)(d_i,S_i) \leq 4 \times 10^{-4} - 10^{-4}S_i: \quad \mathcal{C}_3(d_i,S_i) = 1 \\ \text{else:} \end{cases} \\ \mathcal{C}_3(d_i,S_i) = 1 - 530 \cdot (0.8 - 0.2s) \cdot (-4 \times 10^{-4} + g_{s_i}(d_i,S_i) + 10^{-4}S_i) \end{cases}$$
 (G3)

where  $g_{s_i}(d_i, S_i)$  is defined by Eq. D6.

$$\begin{cases} \text{If } \frac{w_i}{w_i \max} < 0.9: \quad \mathcal{C}_4(w_i, \rho_i) = \begin{cases} 1 + \frac{w_i}{w_i \max} & \text{if } \frac{w_i}{w_i \max} < 0.1 \\ 1.1 - 2.35(\frac{w_i}{w_i \max} - 0.1) & \text{if } 0.1 \leq \frac{w_i}{w_i \max} < 0.3 \\ 0.63 - 0.4(\frac{w_i}{w_i \max} - 0.3) & \text{if } 0.3 \leq \frac{w_i}{w_i \max} < 0.9 \end{cases}$$
 (G4) else: 
$$\mathcal{C}_4(w_i, \rho_i) = \max\left(0.15, \min\left[0.35, (\rho_i - w_i) \times 10^{-4}\right]\right)$$

where  $w_{i \max}(\rho_i, w_i)$  is defined by Eq. 134.

$$\begin{cases} \text{If } h_{i} \in [0,1] \text{ or } \frac{w_{i}}{w_{i} \max} > 0.5 : \mathcal{C}_{5} = 1 \\ \\ \text{else:} \begin{cases} \text{If } w_{i} = 0 : \mathcal{C}_{5} = 1.5 \cdot \left(\frac{1.15 + 0.2(1 - S_{i})}{1.15}\right) \cdot \left(1 + \frac{0.2}{\mathcal{C}_{3}(d_{i}, S_{i})}\right) \\ \\ \text{else:} \end{cases} \begin{cases} \text{If } h_{i} \in [2,3], \mathcal{C}_{5} = 1 \\ \\ \text{else:} \end{cases} \begin{cases} \text{If } h_{i} \in [2,3], \mathcal{C}_{5} = 1 \\ \\ \text{else:} \end{cases} \begin{cases} 1.5 - 2\frac{w_{i}}{w_{i} \max} & \text{if } \frac{w_{i}}{w_{i} \max} < 0.1 \\ \\ 1.3 - 0.75\left(\frac{w_{i}}{w_{i} \max} - 0.1\right) & \text{if } \frac{w_{i}}{w_{i} \max} \ge 0.1 \end{cases}$$





## 1060 Appendix H: MEPRA expert rules

### H1 Classification of profiles

Table H1. MEPRA classification of superior profile

Condition	Type	$Z_{ m SUP}$
$\exists i : PP \in \Theta_i \text{ or } DF \in \Theta_i$	NEW	$\sum_{i=1}^{j} z_i + \sum_{i=j}^{k} z_i$
		$\int j : \mathrm{PP} \in \Theta_j \text{ or } \mathrm{DF} \in \Theta_j \text{ and } (\mathrm{PP} \notin \Theta_i \text{ and } \mathrm{DF} \notin \Theta_i)  \forall i \in [j,N]$
		where $\left\{ k: w_i \geq 5  \forall i \in [j,k] \right\}$
		$ \text{where } \begin{cases} j: \operatorname{PP} \in \Theta_j \text{ or } \operatorname{DF} \in \Theta_j \text{ and } (\operatorname{PP} \notin \Theta_i \text{ and } \operatorname{DF} \notin \Theta_i) \ \forall i \in [j, N] \\ k: w_i \geq 5 \ \forall i \in [j, k] \\ \text{and } \sum_l z_l < 0.01 \ \forall l \in [1, k]   (w_l < 5 \text{ and } \operatorname{MF} \in \Theta_l) \end{cases} $
$\exists i : MF \in \Theta_i \text{ and } Z_i < 0.03$		
For the uppermost layer $j$ satisfying above condition:	FRO	$\sum_{i=j}^{k} z_i$ where $k : MF \in \Theta_i \forall i \in [j,k]$
$\theta_j < -0.2 \text{ or } w_j < 5$		
$\begin{cases} \theta_j < -0.2 \text{ or } w_j < 5 \\ \exists i : \text{MF} \in \Theta_i \text{ and } Z_i < 0.03 \end{cases}$		
For the uppermost layer $j$ satisfying above condition:	WET	$\sum_{i=j}^{k} z_i$ where $k: \mathrm{MF} \in \Theta_i \forall i \in [j,k]$
$w_j \ge 5$		
Other cases	NAN	Undefined

Table H2. MEPRA classification of inferior profile

Condition	Type
$\mathcal{R}_{p_i} \leq 8  orall i \in [k,l]$ where $l: \sum_{i=k}^l z_i \leq rac{Z_{ ext{SUP}}}{4} < \sum_{i=k}^{l+1} z_i$	SOF
$\exists i \in [k,l]: \mathcal{R}_{p_i} > 8 \text{ and } \sum_{i=k}^l z_i \leq \frac{Z_{\text{SUP}}}{4} < \sum_{i=k}^{l+1} z_i$	HAR
$Z < 1.25 Z_{ m SUP}$	NAN

### **H2** Classification of avalanche situations

The avalanche situation is classified in 6 typical classes: NEW\_DRY (new snow, dry), NEW\_WET (new snow, wet), NEW\_MIX (new snow, mixed type), MEL\_SUR (melting at surface), MEL\_GRO (melting, not mainly at surface) and AVA\_NAN if could not identify to an other type. The expert rules determining avalanche type from superior profile, inferior profile, temperature





and liquid water content of layers of superior profile are described in following equation:

$$\begin{cases} \text{NEW} & \begin{cases} \text{If } w_i < 5 \, \forall i | Z_i \leq Z_{\text{SUP}} \rightarrow \text{NEW\_DRY} \\ \text{If } w_i \geq 5 \, \forall i | Z_i \leq Z_{\text{SUP}} \rightarrow \text{NEW\_WET} \\ \text{else} \rightarrow \text{NEW\_MIX} \\ \end{cases} \\ \begin{cases} \text{HAR} \rightarrow \text{MEL\_SUR} \\ \text{SOF} \rightarrow \text{MEL\_GRO} \\ \text{else} & \begin{cases} \text{If } w_i \geq 5 \, \forall i | 0.1 < Z_i \leq Z_{\text{SUP}} \rightarrow \text{MEL\_GRO} \\ \text{else} \rightarrow \text{MEL\_SUR} \end{cases} \\ \begin{cases} \text{If } \mathcal{H}_{\text{nat}} = 0 \rightarrow \text{AVA\_NAN} \\ \text{HAR} \rightarrow \text{MEL\_SUR} \\ \text{SOF} \rightarrow \text{MEL\_GRO} \\ \text{else} & \begin{cases} \text{If } w_k \geq 5 \, \text{for } k | Z_k = Z_{\text{SUP}} \\ \text{and } \sum_{i=j}^k z_i > \frac{Z_{\text{SUP}}}{3} \, \text{where } j | Z_{j-1} < 0.1 < Z_j \end{cases} \\ \end{cases} \rightarrow \text{MEL\_GRO} \\ \\ \text{NAN} \rightarrow \text{AVA\_NAN} \end{cases}$$

#### H3 Accounting for the temporal evolution in natural hazard indice

- If at time t, superior profile is NEW but avalanche type is not NEW\_MIX and if between  $t-\Delta t_M$  and t, avalanche type has remained unchanged and Z and  $Z_{\text{SUP}}$  have decreased, then  $\mathcal{H}_{\text{nat}}$  is updated from Table H3. The same rule is applied if avalanche type is NEW\_MIX but only if the continuous wet thickness  $Z_W = \sum_{i=0}^{n_W} z_i$  where  $n_W | w_i > 5 \, \forall i \in [1, n_W]$  has decreased or remained constant since  $t-\Delta t_M$ .
  - If superior profile is WET or FRO at t and at  $t \Delta t_M$  and  $Z Z_{SUP}$  has not reduced by more than 0.05 m between  $t \Delta t_M$  and t:
    - If  $\mathcal{H}_{nat} = 3$  then it is reduced to 2

- If superior profile is WET and  $\mathcal{H}_{nat}(t) \in [4,5]$  then:
  - If  $\mathcal{H}_{nat}(t \Delta t_M) \in [3, 4, 5]$ , then  $\mathcal{H}_{nat}(t) = 3$
  - If  $\mathcal{H}_{nat}(t \Delta t_M) = 1$ , then  $\mathcal{H}_{nat}(t) = 1$





**Table H3.** Update of  $\mathcal{H}_{nat}$  depending on  $\mathcal{H}_{nat}(t)$  as assessed from Eq. 156 and from its value at previous output time step  $\mathcal{H}_{nat}(t - \Delta t_M)$ . represents an undefined value.

24 (4 A4 )				$t_{\rm nat}(t$			
$\mathcal{H}_{ m nat}(t-\Delta t_M)$	0	1	2	3	4	5	-
0	0	1	2			5	-
1	0	1	1	1	4	5	-
2	0	1	1	1	4		-
3	0	1	1	1	3	4	-
4	0	1	2	3	3	4	-
5	0	1	2	3	3	4	-
-	0	1	2	3	4	5	-

#### H4 Equivalent natural hazard indice

080 In Eq. 160,  $\mathcal{H}_{eq}$  is designed to account for natural hazards in the assessment of the accidental hazard indice. It is defined by:

$$\begin{cases} \text{If } \mathcal{Z} \geq 0.2m \begin{cases} \text{If } \mathcal{H}_{\text{nat}} \geq 4: & \mathcal{H}_{\text{eq}} = 3 \\ \text{If } 2 \leq \mathcal{H}_{\text{nat}} < 4: & \mathcal{H}_{\text{eq}} = 2 \\ \text{If } \mathcal{H}_{\text{nat}} = 1: & \mathcal{H}_{\text{eq}} = 1 \end{cases} \end{cases}$$
(H2)
$$\text{else}: \qquad \qquad \mathcal{H}_{\text{eq}} = 1$$

### Appendix I: Numerical efficiency of loops

1085

1090

1095

All equations of this paper must be applied iteratively over all simulation points and often over all snow layers. The variable number of active snow layers N between points introduces a spatial dependence of the boundary of the loop iterator operating on snow layers. Furthermore, the maximum number of snow layers also depends on time. Several options are possible to implement these specificities, in the context where in SURFEX the leftmost dimension of arrays represent the spatial dimension, which is also the fastest varying dimension in Fortran with continous memory storage. Without extended analyses of their numerical impact, two options were implemented in previous versions of the code. A compressed-index form (CINDX, Algorithm II) where the loop over snow layers is inside the loop over points had been chosen by Vionnet et al. (2012) in most parts of the code. This option minimizes the number of iterations and operations as the boundary of the snow layer iterator can vary between points and dates. However, the successive accesses to the values of the arrays are not performed continuously relatively to the memory storage involving more expensive memory accesses and preventing from the vectorization of computations. A full iteration with condition (FCOND, Algorithm I2) had been chosen in other parts including the heat diffusion and the TARTES optical scheme. This option does not minimize the number of iterations but still minimizes the number of operations and allows continuous memory accesses. However, it adds a potentially expensive conditional statement which still





prevents from vectorization. Other options could be considered. For instance, a full iteration with a predefined mask (FMASK, Algorithm I3) allows continuous memory access and vectorization. However, it adds operations on empty layers so that the interest of this approach is expected to increase with the matrices density. Note also that some operations such as divisions must be secured with this approach to avoid floating point exceptions on empty layers.

## Algorithm I1 Loops with compressed index (CINDX): illustration for the computation of vertical gradient

```
\begin{array}{l} \text{for } p \in [1,N_p] \text{ do} \\ \text{for } i \in [1,N(p)-1] \text{ do} \\ \mathcal{G}(p,i) = 2\frac{T(p,i)-T(p,i+1)}{z(p,i)+z(p,i+1)} \\ \text{end for} \\ \end{array}
```

## Algorithm I2 Loops with full iteration with condition (FCOND): illustration for the computation of vertical gradient

```
\begin{split} &\text{for } i \in [1,N_{\max}-1] \text{ do} \\ &\text{ for } p \in [1,N_p] \text{ do} \\ &\text{ if } i \leq N(p)-1 \text{ then} \\ &\mathcal{G}(p,i) = 2\frac{T(p,i)-T(p,i+1)}{z(p,i)+z(p,i+1)} \\ &\text{ end if} \\ &\text{ end for} \end{split}
```

**Algorithm I3** Loops with full iteration with mask (FMASK): illustration for the computation of vertical gradient. MASK is a precomputed array with 1 values for defined snow layers  $(i \le N)$  and 0 for undefined layers (i > N)

```
\begin{split} & \textbf{for } i \in [1, N_{\max} - 1] \textbf{ do} \\ & \textbf{ for } p \in [1, N_p] \textbf{ do} \\ & \mathcal{G}(p, i) = 2 \frac{T(p, i) - T(p, i + 1)}{z(p, i) + z(p, i + 1)} \times \text{MASK}(p, i) \\ & \textbf{ end for} \\ & \textbf{ end for} \end{split}
```

1100

1105

Comparing the numerical efficiency of the whole model with these different options would represent a considerable amount of work because it would need to code all the model loops with these options. Therefore, the efficiency of these different options were only compared on simple test cases with random initialization values: the sum of a quantity over the vertical dimension (i.e. computation of total snow depth Z), the computation of the vertical gradient of a quantity (i.e. Eq. 42), the solving of a linear system with a tridiagonal matrix (i.e. Eq. 106), and finally the series of Equations to represent metamorphism (Section 2.4.5). The obtained results are presented in Table I1 and exhibit a large variability depending on the operations and matrix filling. Although, the initially implemented compressed-index method was found to be more efficient for all operations in the



1110



case of sparse matrices (N=12 layers), the efficiency is highly deteriorated in case of dense matrices (N closer to 50) probably due to the discontinuous accesses to memory. The full iteration with condition has the best efficiency for simple operations. The full iteration with mask improves the efficiency of the inversion of tridiagonal matrix compared to other methods but deteriorates the efficiency of the complex metamorphism routine with numerous conditional statements. Finally, the whole code was homogenized using a full iteration with condition (FCOND) allowing continuous memory accesses and presenting more stable computing times in the most common cases. We recommend that future developments follow the same approach, unless a dedicated efficiency performance test is able to demonstrate that an added value is obtained with another method for a specific and expensive algorithm.





**Table I1.** Comparison of computing time of loops based on compress-index form (CINDX), a full iteration with condition (FCOND), and a full iteration with mask (FMASK), for 4 types of operations: Sum over the layer dimension; Computation of vertical gradients; Solving of a linear system with tridiagonal matrix (Eq. 106); and the whole metamorphism routine (Sect. 2.4.5). Tests were applied with 3 different densities of matrices (12 layers / 50; 50 layers / 50; or random values between 12 and 50 layers / 50) and with two lengths of the spatial dimension (100 points and 4000 points, adjusting the number of iterations to have the same number of computations). Tests are performed with Intel®Fortran Compiler 18.0.5 and O2 optimization level on one physical core of a 2.2 GHz AMD©Rome computing node.

Points	Layers	Iterations	Operation	CINDX	FCOND	FMASK
100	12	4000000	Sum	2.2	4.5	6.1
100	12	4000000	Gradient	9.8	14.5	14.5
100	12	400000	Eq. 106	2.7	3.6	4.1
100	12	40000	Metamorphism	9.6	9.9	13.8
4000	12	100000	Sum	1.4	4.6	6.0
4000	12	100000	Gradient	10.2	14.6	14.7
4000	12	10000	Eq. 106	2.8	3.3	4.1
4000	12	1000	Metamorphism	9.0	10.1	13.9
100	50	4000000	Sum	9.3	4.5	6.0
100	50	4000000	Gradient	29.5	14.4	14.5
100	50	400000	Eq. 106	17.8	7.4	4.1
100	50	40000	Metamorphism	35.8	34.9	34.3
4000	50	100000	Sum	9.9	4.6	6.1
4000	50	100000	Gradient	37.4	14.5	14.7
4000	50	10000	Eq. 106	22.2	7.3	4.0
4000	50	1000	Metamorphism	34.9	35.3	35.1
100	[12-50]	4000000	Sum	5.0	4.6	6.0
100	[12-50]	4000000	Gradient	20.4	14.5	14.5
100	[12-50]	400000	Eq. 106	11.2	5.9	4.1
100	[12-50]	40000	Metamorphism	23.5	23.9	26.2
4000	[12-50]	100000	Sum	7.5	4.6	6.1
4000	[12-50]	100000	Gradient	29.6	14.6	14.7
4000	[12-50]	10000	Eq. 106	13.8	10.0	4.8
4000	[12-50]	1000	Metamorphism	23.0	24.2	28.1





# 1115 Appendix J: Symbols and units

## J1 Indexes

Symbol	Description
i	snow layer, $i=1$ refers to the surface layer, increasing indexes going down
j	type of Light-Absorbing Particles
k	spectral band for solar radiation
p	simulation point (spatial dimension)

## J2 Variables

Symbol	Units	Description
$A_i$	days	Age of snow layer $i$
$C_H$	-	Exchange coefficient for turbulent fluxes
$d_i$	m	Optical diameter of layer $i$
$d_n$	m	Optical diameter of new snow
$d_{\mathrm{SP}}$	m	Optical diameter of solid precipitation
$d_{ m BS}$	m	Optical diameter of blowing snow
D(i, i+1)	-	Similarity criteria between layers $i$ and $i+1$
${\cal D}_i$	-	Driftability indice of layer $i$
$f_i$	${\rm kg}{\rm m}^{-2}$	Mass of melting for layer $i$ during a time step
$E_{FRZ}$	${ m Wm^{-2}}$	Energy released at the surface by freezing of supercooled rain
$E_i$	${ m Wm^{-2}}$	Energy of phase change for layer $i$
$E_{f_i}$	${ m Wm^{-2}}$	Energy available for fusion in layer $i$
$E_{r_i}$	${ m Wm^{-2}}$	Energy available for refreezing in layer $i$
$E_{k_i}$	${ m Wm^{-2}}$	Absorbed solar radiation by layer $i$ for spectral band $k$
$\mathcal{F}_i$	${\rm kg}{\rm m}^{-2}$	Liquid water flow between layer $i$ and $i+1$ during a time step
$G_i$	${\rm K}{\rm m}^{-1}$	Vertical temperature gradient in layer $i$
$G_i$	${ m Wm^{-2}}$	Global heat flux between layers $i$ and $i-1$
$h_i$	-	Historical tracker of layer $i$
H	${ m Wm^{-2}}$	Surface turbulent sensible heat flux
$H_i$	$\mathrm{J}\mathrm{m}^{-2}$	Enthalpy of layer $i$
$\mathcal{H}_{\mathrm{nat}}$	0-5	Natural avalanche hazard indice of the simulated snow profile
$\mathcal{H}_{\mathrm{acc}}$	0-3	Accidental avalanche hazard indice of the simulated snow profile
$l_i$	${\rm kg}{\rm m}^{-2}$	Mass of liquid water of layer $i$
$K_i$	${ m Wm^{-2}}$	Conduction heat flux between layers $i$ and $i-1$
LE	${ m Wm^{-2}}$	Surface turbulent latent heat flux
$l_{\mathrm{inf}}, l_{\mathrm{sup}}$	-	Adjacent layers minimizing the penalty criteria
LW↓	${ m Wm^{-2}}$	Incoming atmospheric longwave radiation
$m_i$	${\rm kg}{\rm m}^{-2}$	Total mass of layer $i$
$m_n$	${\rm kg}{\rm m}^{-2}$	Mass of new snow
$m_{\mathrm{SP}}$	${\rm kg}{\rm m}^{-2}$	Mass of new solid precipitation
$m_{ m BS}$	${\rm kg}{\rm m}^{-2}$	Mass of new blowing snow
$m_{ m SM}$	${\rm kg}{\rm m}^{-2}$	Mass of new machine-made snow
$M_X$	${\rm kg}{\rm m}^{-2}$	Mass of snow more recent than $X$ days
$\mathcal{M}_{i,j}$	${\rm kg}{\rm m}^{-2}$	Mass of Light-Absorbing Particles of type $j$ in layer $i$
$MOB_i$	-	Mobility indice of layer i
N	_	Number of active layers





$N_p$	_	Number of simulation points
$n_X$	_	Number of layers more recent than X days
$n_r$	_	Number of refrozen layers at the surface
$n_w$	_	Number of wet layers at the surface
$\mathcal{P}_r$	${\rm kg}{\rm m}^{-2}{\rm s}^{-1}$	Rainfall flux
$\mathcal{P}_s$	$kg  m^{-2}  s^{-1}$	Snowfall flux
$P_s$	Pa	Atmospheric pressure at surface
P(i, i+1)	1 4	Penalty criteria for aggregation between layers $i$ and $i + 1$
, , ,	$kg kg^{-1}$	Air specific humidity at reference height $z_a$
$q_a$ $q_{sat}(T)$	kg kg <sup>-1</sup>	Saturation specific humidity for temperature $T$
	kg m <sup>-2</sup>	Mass of refrozen water for layer <i>i</i> during a time step
$r_i \ R_i$	${ m Wm^{-2}}$	Shortwave radiative flux between at the interface between layers $i$ and $i + 1$
Ri	VV 111	Richardson number
	kgf	Penetration resistance of layer i
$\mathcal{R}_{p_i}$	kgf dm <sup>-2</sup>	•
$\mathcal{R}_{s_i}$	kg m <sup>-2</sup>	Shear resistance of layer i
$s_i$	kg m	Mass of solid phase of layer i
$S_i$	-	Sphericity of layer i
$S_n$	-	Sphericity of new snow
$S_{\mathrm{SP}}$	-	Sphericity of solid precipitation
$S_{\mathrm{SP}}$	-	Sphericity of blowing snow
$\mathcal{S}_{nat_i}$	-	Stability indice of layer <i>i</i> for natural avalanche release
$\mathcal{S}_{acc_i}$	2, _1	Stability indice of layer i for accidental avalanche release
$SSA_i$	$\mathrm{m^2kg^{-1}}$ $\mathrm{Wm^{-2}}$	Specific Surface Area of snow layer i
$SW_{DIR} \downarrow$		Incoming direct solar shortwave radiation
$SW_{DIF} \downarrow$	${ m W}{ m m}^{-2}$	Incoming diffuse solar shortwave radiation
SW↓	${ m W}{ m m}^{-2}$	Incoming total solar shortwave radiation
$\mathrm{SW}_k\!\downarrow$	$\mathrm{W}\mathrm{m}^{-2}$	Incoming spectral shortwave radiation for band $k$
$T_a$	K	Air temperature at reference height $z_a$
$T_a^*$	°C	Air temperature at reference height $z_a$
$T_w^*$	°C	Wet bulb air temperature
$T_d^*$	°C	Dew point air temperature
$T_i$	K	Temperature of layer i
$T_{G_1}$	K	Temperature of surface soil layer
U	${\rm m}{\rm s}^{-1}$	Wind speed at reference height $z_u$
$U_{>1}$	${\rm m}{\rm s}^{-1}$	Wind speed at reference height $z_u$ with a minimum threshold of $1~{\rm ms}^{-1}$ for the computation of turbulent fluxes
$U_z$	${\rm ms}^{-1}$	Wind speed at height $z$
$\mathcal{V}_{ ext{SM}}$	$kg m^{-2} s^{-1}$	Water consumption for snow making
$w_i$	$\mathrm{kg}\mathrm{m}^{-3}$	Volumetric liquid water content of layer $i$
$w_{i \text{ max}}$	$kg m^{-3}$	Maximum liquid water holding capacity of layer $i$
${\mathcal W}_{d,j}$	$kg m^{-2} s^{-1}$	Dry deposition flux for Light-Absorbing Particles of type $j$
${\cal W}_{w,j}$	${\rm kg}{\rm m}^{-2}{\rm s}^{-1}$	Wet deposition flux for Light-Absorbing Particles of type $j$
$z_i$	m	Thickness of layer i
$z_n$	m	Thickness of new snowfall
${Z}_i$	m	Depth of the bottom of layer $i$ from the surface
$Z_X$	m	Thickness of snow more recent than $X$ days
$Z_r$	m	Thickness of refrozen snow at the surface
$Z_w$	m	Thickness of wet snow at the surface
$\alpha_k$		Spectral surface albedo for band $k$
$\beta_{k_i}$	$\mathrm{m}^{-1}$	Absorption coefficient of solar radiation for band $k$ and layer $i$
$\eta_i$	$\rm kgs^{-1}m^{-1}$	Viscosity of layer $i$
$ heta_i$	$^{\circ}\mathrm{C}$	Temperature of layer $i$
$\Theta_i$	-	Grain type of layer $i$ in the International Snow Classification





$\lambda_i$	$\mathrm{Wm^{-1}K^{-1}}$	Thermal conductivity of layer $i$
$\lambda_{G_1}$	$\mathrm{Wm^{-1}K^{-1}}$	Thermal conductivity of surface soil layer
$\overline{\lambda_i}$	$\mathrm{Wm^{-1}K^{-1}}$	Integrated thermal conductivity for layers $i$ and $i+1$
$\mu$	-	Cosine of solar zenithal angle
$\Pi_a$	-	Exner function at height $z_a$
$\Pi_s$	-	Exner function at the surface
$ ho_a$	${\rm kg}{\rm m}^{-3}$	air volumetric mass
$ ho_i$	${\rm kg}{\rm m}^{-3}$	Density of layer $i$
$ ho_n$	${\rm kg}{\rm m}^{-3}$	Density of new snow
$ ho_{ ext{SP}}$	${\rm kg}{\rm m}^{-3}$	Density of natural snowfall
$ ho_{ ext{BS}}$	${\rm kg}{\rm m}^{-3}$	Density of blowing snow
$\sigma_i$	Pa	Pressure of over burden snow for layer $i$
$\sigma_{\mathrm{GRO}_i}$	Pa	Static stress due to snowcat for layer $i$
$\phi_i$	-	Porosity of snow layer $i$
$\phi_{ extsf{FRZ}}$	-	Fraction of latent heat release due to the freezing of supercooled rain consumed by the heating up to $\mathcal{T}_0$

## J3 Fixed parameters

Symbol	Values and units	Description
		Thermodynamical and physical parameters
$c_I$	$2.106 \times 10^{3} \; \mathrm{J  kg^{-1}  K^{-1}}$	Ice specific heat capacity
$c_W$	$4.218 \times 10^{3} \; \mathrm{J  kg^{-1}  K^{-1}}$	Liquid water specific heat capacity
$c_P$	$1.0047 \times 10^{3} \; \mathrm{J  kg^{-1}  K^{-1}}$	Dry air specific heat capacity
$c_{P_v}$	$1.8461 \times 10^{3} \; \mathrm{J  kg^{-1}  K^{-1}}$	Vapor specific heat capacity
$c_{P_m}$	$1.013 \times 10^{3} \; \mathrm{J  kg^{-1}  K^{-1}}$	Typical moist air specific heat capacity
€VK	0.4	Von Karman constant
$L_m$	$3.337 \times 10^5 \; \mathrm{J  kg^{-1}}$	Latent heat of ice fusion
$L_v$	$2.5008 \times 10^6 \mathrm{Jkg^{-1}}$	Latent heat of vaporization of liquid water
$L_s$	$2.8345 \times 10^6 \; \mathrm{J  kg^{-1}}$	Latent heat of ice sublimation
$o_I$	$917  \mathrm{kg}  \mathrm{m}^{-3}$	Volumetric mass of pure ice
$o_w$	$1000  \mathrm{kg}  \mathrm{m}^{-3}$	Volumetric mass of liquid water
$R_a$	$287.05967 \mathrm{Jkg^{-1}K^{-1}}$	Specific gas constant for dry air
$R_v$	$461.52499 \mathrm{Jkg^{-1}K^{-1}}$	Specific gas constant for water vapor
$\Gamma_0$	273.16 K	water triple point temperature
τ	$5.6705 \times 10^{-8} \text{Wm}^{-2} \text{K}^{-4}$	Stefan-Boltzmann parameter
9	$9.80665~{ m ms}^{-2}$	Gravitational acceleration
		Layering parameters
$N_{\min}$	3	Minimum number of snow layers
$Z_{\min}$	0.03 m	Threshold for uniform layering
		Parameters for density of new snow when SNOWFALL=V12
$o_{\min}$	$50 \text{ kg m}^{-3}$	Minimum threshold
$\iota_{ ho}$	$109 \text{ kg m}^{-3}$	Regression coefficient
$\rho_{ ho}$	$6  \mathrm{kg}  \mathrm{m}^{-3} \mathrm{K}^{-1}$	Regression coefficient
$\mathbb{C}_{ ho}$	$26 \text{ kg m}^{-7/2} \text{s}^{+1/2}$	Regression coefficient
		Parameters for density of new snow when SNOWFALL=S14
$e_{\rho}$	3.28	Empirical parameter
$f_{\rho}$	0.03	Empirical parameter





$g_{ ho}$	-0.36	Empirical parameter
$h_{ ho}$	-0.75	Empirical parameter
$i_{ ho}$	0.8	Empirical parameter
$j_{ ho}$	0.3	Empirical parameter
J ρ		Empirical parameter
		Parameters for density of new snow when SNOWFALL=A76
$k_{ ho}$	$1.7 \text{ kg m}^{-3} \text{K}^{-1.5}$	Regression coefficient
$l_{\rho}$	15 K	Regression coefficient
		Parameters for metamorphism
sph <sub>1</sub>	$11574.07 \text{ s}^{-1}$	Empirical parameter
$sph_2$	$2314.81  \mathrm{s}^{-1}$	Empirical parameter
sph <sub>3</sub>	$7.2337 \times 10^{-7} \text{ s}^{-1}$	Empirical parameter
$a_s$	$1.1 \times 10^{-6} \text{m}^2 \text{kg}^{-1} \text{s}^{-1}$	Empirical parameter
$b_s$	$3.1 \times 10^{-8}$	Empirical parameter
$m_s$	3.1	Empirical parameter
	0.12	
	$2.22\mathrm{Wm^{-1}K^{-1}}$	Parameters for thermal conductivity when SNOWCOND=Y81
$a_{\lambda}$		Empirical parameter
$\lambda_{\min}$	$4 \times 10^{-2} \text{Wm}^{-1} \text{K}^{-1}$	Empirical parameter
		Parameters for thermal conductivity when SNOWCOND=C11
$b_{\lambda}$	$2.5 \times 10^{-6}  \mathrm{Wm}^{5} \mathrm{K}^{-1} \mathrm{kg}^{-2}$	Empirical parameter
$c_{\lambda}$	$-1.23 \times 10^{-4} \text{Wm}^2 \text{K}^{-1} \text{kg}^{-1}$	Empirical parameter
$d_{\lambda}$	$2.4 \times 10^{-2} \mathrm{Wm^{-1}K^{-1}}$	Empirical parameter
		Parameters for thermal conductivity when SNOWCOND=I02
0.	$2.0 \times 10^{-2} \mathrm{Wm^{-1}K^{-1}}$	Empirical parameter
$e_{\lambda}$	$2.5 \times 10^{-6} \text{Wm}^5 \text{K}^{-1} \text{kg}^{-2}$	
$f_{\lambda}$		Empirical parameter
$g_{\lambda}$	$-6.023 \times 10^{-2} \mathrm{Wm^{-1}K^{-1}}$	Empirical parameter
$h_{\lambda}$	-2.5425Wm <sup>-1</sup>	Empirical parameter
$i_{\lambda}$	-289.99K	Empirical parameter
$P_0$	$10^5  \mathrm{Pa}$	Empirical parameter
		Parameters for solar radiation absorption when SNOWRAD=B92
$\gamma_1$	0.71	Fraction of shortwave radiation in band [0.3-0.8 µm]
$\gamma_2$	0.21	Fraction of shortwave radiation in band [0.8-1.5 µm]
$\gamma_3$	0.08	Fraction of shortwave radiation in band [1.5-2.8 µm]
$P_{\text{CDP}}$	$8.7\times10^5\;\mathrm{Pa}$	Reference atmospheric pressure at Col de Porte
		Parameters for solar radiation absorption when SNOWRAD=T17
١	400 nm	Reference wavelength for dust MAE
$\lambda_0$		
$MAE(\lambda_0)$	$110 \mathrm{m^2 kg^{-1}}$	Mass Absorption Efficiency of dust at wavelength $\lambda_0$
AAE	4.1	Angström absorption exponent for dust
$\rho_{\mathrm{BC}}$	$1270 \mathrm{kg} \mathrm{m}^{-3}$	Density of black carbon
$m_{ m BC}$	1.95-0.79 i	Refractive index of black carbon
$f_{ m BC}$	1.638	Multiplicative factor to compute black carbon MAE
		Parameters for Light-Absorbing Particles
h	$0.005 \mathrm{\ m}$	E-folding depth of the exponential decay rate for dry deposition
		Parameters for compaction when SNOWCOMP=B92
$\eta_0$	$7.62237 \times 10^6 \text{ kg s}^{-1} \text{m}^{-1}$	Empirical parameter
$a_{\eta}$	$0.1  \mathrm{K}^{-1}$	Empirical parameter
	$0.023 \mathrm{m}^3\mathrm{kg}^{-1}$	Empirical parameter
$b_{\eta}$	$250 \text{ kg m}^{-3}$	
$c_{\eta}$	250 Kg III	Empirical parameter





		Parameters for compaction when SNOWCOMP=S14
$B_S$	$3.96 \times 10^{-2}$	Empirical parameter
$k_S$	0.18	Empirical parameter
		Parameters for snow drift
$a_{ m SUBL}$	$1.8 \times 10^{-3}$	Empirical parameter
$b_{ m SUBL}$	4	Empirical parameter
$c_{ m SUBL}$	2.868	Empirical parameter
$d_{ m SUBL}$	0.085	Empirical parameter
$\gamma_{ ext{SUBL}}$	3.6	Empirical parameter
		Parameters for percolation when SNOWLIQ=B02
$r_{\min}$	0.03	Mass of liquid fraction parameter in B02 parameterization
$r_{ m max}$	0.1	Mass of liquid fraction parameter in B02 parameterization
$ ho_r$	$200 \text{ kg m}^{-3}$	Density parameter in B02 parameterization
		Parameters for snowmaking and grooming
$\mathcal{A}_{\mathrm{SM}}$	$3300 \mathrm{\ m}^2$	Surface area covered by a snowgun
$\mathcal{L}_{\mathrm{SM}}$	0.4	Loss factor during snowmaking
$d_{\mathrm{SM}}$	$2.8\times10^{-4}~\mathrm{m}$	Optical diameter of machine-made snow
$S_{\mathrm{SM}}$	0.9	Sphericity of machine-made snow
$\rho_{ m GRO}$	$450 \text{ kg m}^{-3}$	Target density of groomed snow
$d_{\mathrm{GRO}}$	$2.6\times10^{-4}~\mathrm{m}$	Optical diameter of groomed snow
$S_{\rm GRO}$	0.9	Sphericity of groomed snow
		Parameters for unloading
$ ho_{ m UN}$	$200  {\rm kg  m^{-3}}$	Density of unloaded snow
$d_{\mathrm{UN}}$	$6 \times 10^{-4} \text{ m}$	Optical diameter of unloaded snow

# 1120 J4 Physiographic parameters

Symbol	units	Description
$z_{G_j}$ $\gamma$	m rad	Depth of soil layer $j$ Slope angle

## J5 Parameters adjustable in namelist

Symbol	Default values and units	Description
$N_{ m max}$	50	Maximum number of layers
$\Delta t$	900 s	model time step
$\epsilon$	0.99	snow emissivity
$Ri_l$	0.026	Threshold on the Richardson number for the exchange coefficient parameterization
$z_0$	$10^{-3} \text{m}$	snow roughness for momentum
$z_{0_h}$	$10^{-4} { m m}$	snow roughness for heat
$z_a$	2 m	Reference height for air temperature
$z_u$	10 m	Reference height for wind speed
$\alpha_{1_G}$	0.38	Glacier albedo in band [0.3-0.8 µm]
$\alpha_{2_G}$	0.23	Glacier albedo in band [0.8-1.5 $\mu m$ ]
$\alpha_{3_G}$	0.08	Glacier albedo in band [1.5-2.8 µm]



1125

1130

1135

1140



$ ho_G$	$850 \text{ kg m}^{-3}$	Density threshold to separate snow and ice on glaciers
$ au_a$	$60\mathrm{days}$	Time constant in visible albedo parameterization
$C_{\mathrm{scav},j}$	0	Scavenging coefficient for Light-Absorbing Particles of type $j$
$T_{ m lim}$	269.15 K	Snowmaking: wet but temperature threshold
$U_{ m lim}$	$4.2 \text{ m s}^{-1}$	Snowmaking: wind speed threshold
$day_1$	November 1st	Snowmaking: day of beginning of the base-layer generation production period
$day_2$	December 15th	Snowmaking: day of end of the base-layer generation production period
$day_3$	March 31st	Snowmaking: day of end of the reinforcement production period
$t_1$	0  s (= 0 am)	Snowmaking: time of beginning of the base-layer generation production period
$t_2$	86400 s (= 12pm)	Snowmaking: time of end of the base-layer generation production period
$t_3$	64800 s (= 6pm)	Snowmaking: time of beginning of the reinforcement production period
$t_4$	28800 s (= 8am)	Snowmaking: time of end of the reinforcement production period
$p_{ m lim}$	$150 \text{ kg m}^{-2}$	Snowmaking: water use allowance for the base-layer generation production period
$Z_{ m lim}$	0.6 m	Snowmaking: total (natural + machine-made) snow depth threshold for the reinforcement production period
$ ho_{ m SM}$	$500 \text{ kg m}^{-3}$	Snowmaking: machine-made snow density
$a_{ m SM}$	$-0.4377 \text{ kg K}^{-1} \text{ s}^{-1}$	Snowmaking: coefficient to compute the production potential mass of lance guns
$b_{ m SM}$	$-0.47 \text{ kg s}^{-1}$	Snowmaking: coefficient to compute the production potential mass of lance guns
$day_{\rm END}$	4, 30, 4, 30	Grooming: month and day at which grooming is stopped (without and with snowmaking, respectively)
$f_{\rm GRO}$	1 day <sup>-1</sup>	Grooming: daily frequency of grooming

Code and data availability. The Crocus snowpack model is developed within the opensource SURFEX project within CeCILL-C 1.0 license (https://cecill.info/licences/Licence\_CeCILL-C\_V1-en.html, last access 10 September 2025). The source code of the version referred in this work can be accessed freely on https://doi.org/10.5281/zenodo.16943239 (Lafaysse et al., 2025). Obviously, the code will evolve after submission and publication. The most up-to-date stable version of Crocus can be accessed through the branch cen of the SURFEX git repository. Although, the git repository is currently hosted on https://opensource.umr-cnrm.fr/projects/surfex\_git2 (last access 10 September 2025), requiring registration, it is expected to be transferred to https://github.com/UMR-CNRM/ (last access 10 September 2025) by December 2025 to allow a wider and free access to future versions. Latest developments not yet stabilized are in branch cen\_dev. For reproductibility of results, providing a git tag is recommended in any publication based on Crocus simulations with any modification of the source code compared to the version associated with this paper. The version described in this work is tagged as crocus3.0.

The SURFEX Land Surface Model comes with a comprehensive documentation including user's guide, technical and scientific documentation available at https://www.umr-cnrm.fr/surfex/, last access 10 September 2025. Nevertheless, we recommend to combine the use of SURFEX-Crocus with the snowtools\_git Python3 package (Section 4.3) which includes pre and post-processing tools. Version 2.0.3 of the snowtools package was fully tested with Crocus3.0 and archived on https://doi.org/10.5281/zenodo.17122726 (Viallon-Galinier et al., 2025). The installation of the most up-to-date version and execution procedures are described in https://umr-cnrm.github.io/snowtools-doc/, last access 10 September 2025. This documention includes a summarized documentation to install SURFEX-Crocus and run a first test case (https://umr-cnrm.github.io/snowtools-doc/misc/surfex-install.html, last access 10 September 2025). The users may request technical support on registration at https://github.com/UMR-CNRM/snowtools-tickets/ (last access 10 September 2025). We can not guarantee a fixed response time. Technical support requested by e-mail will not be considered.

The externalized version of Crocus is also available on https://doi.org/10.5281/zenodo.16943239 (Lafaysse et al., 2025). However, model developers who intent to couple their LSM with Crocus are encouraged to access the code through the SURFEX git repository following the dedicated procedure https://opensource.umr-cnrm.fr/projects/surfex\_git2/wiki/Install\_standalone\_version\_of\_Crocus, last access 1st



1150

1155

1165



September 2025. This will highly facilitate future updates of the code coming from the SURFEX implementation and allow to provide new contributions potentially useful for the whole Crocus community.

Author contributions. ML wrote the paper with contribution of all authors and has led the Crocus model development since 2012 with support of MD and SM. BDF (with major contribution), JB, KF, MB and LR read and help to fix typos in the equations and their consistency with the code. LVG wrote the description of the mechanical diagnoses and MEPRA. We only mention here the contributions to the code from the previous reference paper (2012). RN and MF undertook various technical improvements, merging and optimizations. BC and ML implemented the different multiphysics options. ML implemented TARTES within Crocus, the management of glacier configurations, and model diagnoses. ML coupled Crocus with MEB with the help of ABoo. ABou implemented unloading from vegetation with the scientific supervision of ABoo. FT implemented light-absorbing particles with the scientific supervision of MD. PS and CC implemented machine made snow and snow grooming with the scientific supervision of SM. CC initiated the implementation of the new formalism of metamorphism with the scientific supervision of SM. MB fixed this implementation of metamorphism as described in this paper. MB and AH coupled Crocus with Snowpappus and adjusted the drift parameterizations. LQ implemented the management of ice layers after freezing rain with the scientific supervision of VV. PH implemented the MEPRA module within SURFEX. VV coupled Crocus with the SYTRON blowing snow module within SURFEX. VV coupled the externalized version of Crocus with the SVS2 platform and has frequently provided contributions to the code. GM coupled Crocus with the FSM2 platform. MM has supervised the different updates of Crocus within SURFEX. SM, MD and ML led the snow modelling team of CNRM/CEN respectively from 2009 to 2015, 2015 to 2020, and 2021 to today.

1160 Competing interests. The authors declare that they have no conflict of interest.

Acknowledgements. Authors acknowledge the pioneering work of Eric Brun, now retired, who initially developed the model in the late 1980s and implemented a large part of the current version within the SURFEX platform in 2010. They also acknowledge the numerous contributions of students and permanent staff that contributed to the model development, evaluations and applications during 35 years. This paper receives contributions from authors (MD, BDF, KF, JB, LR, FT) funded by the European Research Council (ERC) under the European Union's Horizon 2020 research and innovation program (IVORI; grant no. 949516). CNRM/CEN is part of LabEX OSUG@2020.





#### References

- Agosta, C., Amory, C., Kittel, C., Orsi, A., Favier, V., Gallée, H., van den Broeke, M. R., Lenaerts, J. T. M., van Wessem, J. M., van de Berg, W. J., and Fettweis, X.: Estimation of the Antarctic surface mass balance using the regional climate model MAR (1979–2015) and identification of dominant processes, The Cryosphere, 13, 281–296, https://doi.org/10.5194/tc-13-281-2019, 2019.
- 1170 Anderson, E. A.: A point energy and mass balance model of a snow cover, Tech. rep., Office of Hydrology National Weather Service, 1976. Avanzi, F., De Michele, C., Morin, S., Carmagnola, C. M., Ghezzi, A., and Lejeune, Y.: Model complexity and data requirements in snow hydrology: seeking a balance in practical applications, Hydrol. Process., 30, 2106–2118, https://doi.org/10.1002/hyp.10782, 2016.
  - Baron, M.: Modelling soil thermal regimes in high altitude open environments of the french Alps: effect of wind-induced snow transport and vegetation, Theses, Université Grenoble Alpes [2020-2023], https://theses.hal.science/tel-04434521, 2023.
- Baron, M., Haddjeri, A., Lafaysse, M., Le Toumelin, L., Vionnet, V., and Fructus, M.: SnowPappus v1.0, a blowing-snow model for large-scale applications of the Crocus snow scheme, Geosci. Model Dev., 17, 1297–1326, https://doi.org/10.5194/gmd-17-1297-2024, 2024.
  - Barrere, M., Domine, F., Decharme, B., Morin, S., Vionnet, V., and Lafaysse, M.: Evaluating the performance of coupled snow-soil models in SURFEXv8 to simulate the permafrost thermal regime at a high Arctic site, Geosci. Model Dev., 10, https://doi.org/10.5194/gmd-10-3461-2017, 2017.
- Basnet, S. and Thériault, J. M.: Quantification of the impact of latent heat associated with the freezing of supercooled drops at the surface during freezing rain over Eastern Canada, Atmos. Res., 323, 108 120, https://doi.org/10.1016/j.atmosres.2025.108120, 2025.
  - Bond, T. C. and Bergstrom, R. W.: Light Absorption by Carbonaceous Particles: An Investigative Review, Aerosol Sci. Technol., 40, 27–67, https://doi.org/10.1080/02786820500421521, 2006.
- Boone, A.: Description du schema de neige ISBA-ES (Explicit Snow), Tech. rep., Note de Centre, Meteo-France/CNRM, 70, https://www. 1185 umr-cnrm.fr/IMG/pdf/snowdoc.pdf, 2002.
  - Boone, A. and Etchevers, P.: An intercomparison of three snow schemes of varying complexity coupled to the same land-surface model: Local scale evaluation at an Alpine site, J. Hydrometeorol., 2, 374 394, https://doi.org/10.1175/1525-7541(2001)002<0374%3AAIOTSS>2.0.CO%3B2, 2001.
- Boone, A., Samuelsson, P., Gollvik, S., Napoly, A., Jarlan, L., Brun, E., and Decharme, B.: The interactions between soil-biosphere– 1190 atmosphere land surface model with a multi-energy balance (ISBA-MEB) option in SURFEXv8 – Part 1: Model description, Geosci. Model Dev., 10, 843–872, https://doi.org/10.5194/gmd-10-843-2017, 2017.
  - Bouvet, L., Calonne, N., Flin, F., and Geindreau, C.: Snow Equi-Temperature Metamorphism Described by a Phase-Field Model Applicable on Micro-Tomographic Images: Prediction of Microstructural and Transport Properties, J. Adv. Model. Earth Syst., 14, https://doi.org/10.1029/2022MS002998, 2022.
- Bruland, O., Maréchal, D., Sand, K., and Killingtveit, Å.: Energy and water balance studies of a snow cover during snowmelt period at a high arctic site, Theoretical and Applied Climatology, 70, 53–63, https://doi.org/10.1007/s007040170005, 2001.
  - Brun, E., Martin, E., Simon, V., Gendre, C., and Coléou, C.: An energy and mass model of snow cover suitable for operational avalanche forecasting, J. Glaciol., 35, 333 342, https://doi.org/10.3189/S0022143000009254, 1989.
- Brun, E., David, P., Sudul, M., and Brunot, G.: A numerical model to simulate snow-cover stratigraphy for operational avalanche forecasting,

  J. Glaciol., 38, 13 22, https://doi.org/10.3189/S0022143000009552, 1992.
  - Brun, E., Vionnet, V., Boone, A., Decharme, B., Peings, Y., Valette, R., Karbou, F., and Morin, S.: Simulation of northern Eurasian local snow depth, mass and density using a detailed snowpack model and meteorological reanalysis, J. Hydrometeor., 14, 203–219, https://doi.org/10.1175/JHM-D-12-012.1, 2013.



1215



- Calonne, N., Richter, B., Löwe, H., Cetti, C., ter Schure, J., Van Herwijnen, A., Fierz, C., Jaggi, M., and Schneebeli, M.: The RHOSSA campaign: multi-resolution monitoring of the seasonal evolution of the structure and mechanical stability of an alpine snowpack, The Cryosphere, 14, 1829–1848, https://doi.org/10.5194/tc-14-1829-2020, 2020.
  - Calonne, N., Flin, F., Morin, S., Lesaffre, B., du Roscoat, S. R., and Geindreau, C.: Numerical and experimental investigations of the effective thermal conductivity of snow, Geophys. Res. Lett., 38, L23 501, https://doi.org/10.1029/2011GL049234, 2011.
- Caponi, L., Formenti, P., Massabó, D., Di Biagio, C., Cazaunau, M., Pangui, E., Chevaillier, S., Landrot, G., Andreae, M. O., Kandler, K., Piketh, S., Saeed, T., Seibert, D., Williams, E., Balkanski, Y., Prati, P., and Doussin, J.-F.: Spectral- and size-resolved mass absorption efficiency of mineral dust aerosols in the shortwave spectrum: a simulation chamber study, Atmos. Chem. Phys., 17, 7175–7191, https://doi.org/10.5194/acp-17-7175-2017, 2017.
  - Carmagnola, C. M., Morin, S., Lafaysse, M., Domine, F., Lesaffre, B., Lejeune, Y., Picard, G., and Arnaud, L.: Implementation and evaluation of prognostic representations of the optical diameter of snow in the SURFEX/ISBA-Crocus detailed snowpack model, The Cryosphere, 8, 417–437, https://doi.org/10.5194/tc-8-417-2014, 2014.
  - Castebrunet, H., Eckert, N., Giraud, G., Durand, Y., and Morin, S.: Projected changes of snow conditions and avalanche activity in a warming climate: the French Alps over the 2020-2050 and 2070-2100 periods, The Cryosphere, 8, 1673–1697, https://doi.org/10.5194/tc-8-1673-2014, 2014.
- Charrois, L., Cosme, E., Dumont, M., Lafaysse, M., Morin, S., Libois, Q., and Picard, G.: On the assimilation of optical reflectances and snow depth observations into a detailed snowpack model, The Cryosphere, 10, 1021–1038, https://doi.org/10.5194/tc-10-1021-2016, 2016.
  - Cluzet, B., Revuelto, J., Lafaysse, M., Tuzet, F., Cosme, E., Picard, G., Arnaud, L., and Dumont, M.: Towards the assimilation of satellite reflectance into semi-distributed ensemble snowpack simulations, Cold Reg. Sci. Tech., 170, 102918, https://doi.org/10.1016/j.coldregions.2019.102918, 2020.
- Cluzet, B., Lafaysse, M., Cosme, E., Albergel, C., Meunier, L.-F., and Dumont, M.: CrocO\_v1.0: a particle filter to assimilate snowpack observations in a spatialised framework, Geosci. Model Dev., 14, 1595–1614, https://doi.org/10.5194/gmd-14-1595-2021, 2021.
  - Cluzet, B., Lafaysse, M., Deschamps-Berger, C., Vernay, M., and Dumont, M.: Propagating information from snow observations with CrocO ensemble data assimilation system: a 10-years case study over a snow depth observation network, The Cryosphere, 16, 1281–1298, https://doi.org/10.5194/tc-16-1281-2022, 2022.
- D'Amboise, C. J. L., Müller, K., Oxarango, L., Morin, S., and Schuler, T. V.: Implementation of a physically based water percolation routine in the Crocus/SURFEX (V7.3) snowpack model, Geosci. Model Dev., 10, 3547–3566, https://doi.org/10.5194/gmd-10-3547-2017, 2017.
- Dang, H., Genthon, C., and Martin, E.: Numerical modeling of snow cover over polar icesheets, Ann. Glaciol., 25, 170–176, https://doi.org/10.3189/S0260305500013987, 1997.
  - Decharme, B., Brun, E., Boone, A., Delire, C., Le Moigne, P., and Morin, S.: Impacts of snow and organic soils parameterization on northern Eurasian soil temperature profiles simulated by the ISBA land surface model, The Cryosphere, 10, 853–877, https://doi.org/10.5194/tc-10-853-2016, 2016.
  - Deschamps-Berger, C., Cluzet, B., Dumont, M., Lafaysse, M., Berthier, E., Fanise, P., and Gascoin, S.: Improving the Spatial Distribution of Snow Cover Simulations by Assimilation of Satellite Stereoscopic Imagery, Water Resour. Res., 58, e2021WR030271, https://doi.org/10.1029/2021WR030271, 2022.
- Di Mauro, B., Garzonio, R., Rossini, M., Filippa, G., Pogliotti, P., Galvagno, M., Morra di Cella, U., Migliavacca, M., Baccolo, G., Clemenza,

  M., Delmonte, B., Maggi, V., Dumont, M., Tuzet, F., Lafaysse, M., Morin, S., Cremonese, E., and Colombo, R.: Saharan dust events in





- the European Alps: role in snowmelt and geochemical characterization, The Cryosphere, 13, 1147–1165, https://doi.org/10.5194/tc-13-1147-2019, 2019.
- Dick, O., Viallon-Galinier, L., Tuzet, F., Hagenmuller, P., Fructus, M., Reuter, B., Lafaysse, M., and Dumont, M.: Can Saharan dust deposition impact snowpack stability in the French Alps?, The Cryosphere, 17, 1755–1773, https://doi.org/10.5194/tc-17-1755-2023, 2023.
- Domine, F., Morin, S., Brun, E., Lafaysse, M., and Carmagnola, C. M.: Seasonal evolution of snow permeability under equi-temperature and temperature-gradient conditions, The Cryosphere, 7, 1915–1929, https://doi.org/10.5194/tc-7-1915-2013, 2013.
  - Domine, F., Barrere, M., and Morin, S.: The growth of shrubs on high Arctic tundra at Bylot Island: impact on snow physical properties and permafrost thermal regime, Biogeosciences, 13, 6471–6486, https://doi.org/10.5194/bg-13-6471-2016, 2016.
- Dumont, M., Tuzet, F., Gascoin, S., Picard, G., Kutuzov, S., Lafaysse, M., Cluzet, B., Nheili, R., and Painter, T. H.: Accelerated Snow Melt in the Russian Caucasus Mountains After the Saharan Dust Outbreak in March 2018, J. Geophys. Res. Earth. Surf., 125, e2020JF005 641, https://doi.org/10.1029/2020JF005641, 2020.
  - Durand, Y., Giraud, G., Brun, E., Mérindol, L., and Martin, E.: A computer-based system simulating snowpack structures as a tool for regional avalanche forecasting, J. Glaciol., 45, 469–484, https://doi.org/10.3189/S0022143000001337, 1999.
- Durand, Y., Guyomarc'h, G., and Mérindol, L.: Numerical experiments of wind transport over a mountainous instrumented site: I. Regional scale, Ann. Glaciol., 32, 187–194, https://doi.org/10.3189/172756401781819445, 2001.
  - Durand, Y., Giraud, G., Laternser, M., Etchevers, P., Mérindol, L., and Lesaffre, B.: Reanalysis of 44 Yr of Climate in the French Alps (1958–2002): Methodology, Model Validation, Climatology, and Trends for Air Temperature and Precipitation., J. Appl. Meteor. Climat., 48, 429–449, https://doi.org/10.1175/2008JAMC1808.1, 2009.
- Eckert, N., Coleou, C., Castebrunet, H., Deschatres, M., Giraud, G., and Gaume, J.: Cross-comparison of meteorological and avalanche data for characterising avalanche cycles: The example of December 2008 in the eastern part of the French Alps, Cold Reg. Sci. Tech., 64, 119–136, https://doi.org/https://doi.org/10.1016/j.coldregions.2010.08.009, international Snow Science Workshop 2009 Davos, 2010.
  - Eidhammer, T., Booth, A., Decker, S., Li, L., Barlage, M., Gochis, D., Rasmussen, R., Melvold, K., Nesje, A., and Sobolowski, S.: Mass balance and hydrological modeling of the Hardangerjøkulen ice cap in south-central Norway, Hydrol. Earth Syst. Sci., 25, 4275–4297, https://doi.org/10.5194/hess-25-4275-2021, 2021.
- Essery, R., Martin, E., Douville, H., Fernandez, A., and Brun, E.: A comparison of four snow models using observations from an alpine site, Clim. Dynam., 15, 583–593, https://doi.org/10.1007/s003820050302, 1999.
  - Essery, R., Morin, S., Lejeune, Y., and Bauduin-Ménard, C.: A comparison of 1701 snow models using observations from an alpine site, Adv. Water Res., 55, 131–148, https://doi.org/10.1016/j.advwatres.2012.07.013, 2013.
- Essery, R., Mazzotti, G., Barr, S., Jonas, T., Quaife, T., and Rutter, N.: A Flexible Snow Model (FSM 2.1.1) including a forest canopy, Geosci.

  Model Dev., 18, 3583–3605, https://doi.org/10.5194/gmd-18-3583-2025, 2025.
  - Etchevers, P., Martin, E., Brown, R., Fierz, C., Lejeune, Y., Bazile, E., Boone, A., Dai, Y.-J., Essery, R., Fernandez, A., Gusev, Y., Jordan, R., Koren, V., Kowalczyk, E., Nasonova, N. O., Pyles, R. D., Schlosser, A., Shmakin, A. B., Smirnova, T. G., Strasser, U., Verseghy, D., Yamazaki, T., and Yang, Z.-L.: Intercomparison of the surface energy budget simulated by several snow models (SNOWMIP project), Ann. Glaciol., 38, 150 158, https://doi.org/10.3189/172756404781814825, 2004.
- Evin, G., Lafaysse, M., Taillardat, M., and Zamo, M.: Calibrated ensemble forecasts of the height of new snow using quantile regression forests and ensemble model output statistics, Nonlin. Proc. Geophys., 28, 467–480, https://doi.org/10.5194/npg-28-467-2021, 2021.





- Fettweis, X., Box, J. E., Agosta, C., Amory, C., Kittel, C., Lang, C., van As, D., Machguth, H., and Gallée, H.: Reconstructions of the 1900–2015 Greenland ice sheet surface mass balance using the regional climate MAR model, The Cryosphere, 11, 1015–1033, https://doi.org/10.5194/tc-11-1015-2017, 2017.
- 1280 Fierz, C., Armstrong, R. L., Durand, Y., Etchevers, P., Greene, E., McClung, D. M., Nishimura, K., Satyawali, P. K., and Sokratov, S. A.:

  The international classification for seasonal snow on the ground, IHP-VII Technical Documents in Hydrology n 83, IACS Contribution n
  1, https://unesdoc.unesco.org/ark:/48223/pf0000186462, 2009.
  - Flanner, M., Liu, X., Zhou, C., and Penner, J.: Enhanced solar energy absorption by internally-mixed black carbon in snow grains, Atmos. Chem. Phys., 12, 4699–4721, https://doi.org/doi:10.5194/acp-12-4699-2012, 2012.
- 1285 Flanner, M. G. and Zender, C. S.: Linking snowpack microphysics and albedo evolution, J. Geophys. Res., 111, D12 208, https://doi.org/10.1029/2005JD006834, 2006.
  - Fourteau, K., Brondex, J., Brun, F., and Dumont, M.: A novel numerical implementation for the surface energy budget of melting snowpacks and glaciers, Geosci. Model Dev., 17, 1903–1929, https://doi.org/10.5194/gmd-17-1903-2024, 2024.
  - Fourteau, K., Brondex, J., Cancès, C., and Dumont, M.: Numerical strategies for representing Richards' equation and its couplings in snowpack models, EGUsphere, 2025, 1–30, https://doi.org/10.5194/egusphere-2025-444, 2025.
  - François, H., Samacoïts, R., Bird, D. N., Köberl, J., Prettenthaler, F., and Morin, S.: Climate change exacerbates snow-water-energy challenges for European ski tourism, Nat. Clim. Change, pp. 1–32, https://doi.org/10.1038/s41558-023-01759-5, 2023.
  - Gaillard, M., Vionnet, V., Lafaysse, M., Dumont, M., and Ginoux, P.: Improving large-scale snow albedo modeling using a climatology of light-absorbing particle deposition, The Cryosphere, 19, 769–792, https://doi.org/10.5194/tc-19-769-2025, 2025.
- Gallée, H., Guyomarc'h, G., and Brun, E.: Impact of snow drift on the Antarctic ice sheet surface mass balance: possible sensitivity to snow-surface properties, Bound.-Layer Meteorol., 99, 1–19, https://doi.org/10.1023/A:1018776422809, 2001.
  - Giraud, G., Navarre, J.-P., and Coléou, C.: Estimation du risque avalancheux dans le système expert MEPRA, https://hal.archives-ouvertes. fr/hal-02638748, documentation scientifique, 2002.
- Gordon, M., Simon, K., and Taylor, P.: On snow depth predictions with the Canadian land surface scheme including a parametrization of blowing snow sublimation, Atmos.-Ocean, 44, 239–255, https://doi.org/10.3137/ao.440303, 2006.
  - Gouttevin, I., Vionnet, V., Seity, Y., Boone, A., Lafaysse, M., Deliot, Y., and Merzisen, H.: To the Origin of a Wintertime Screen-Level Temperature Bias at High Altitude in a Kilometric NWP Model, J. Hydrometeorol., 24, 53 71, https://doi.org/10.1175/JHM-D-21-0200.1, 2022.
- Guyomarc'h, G. and Merindol, L.: Validation of an application for forecasting blowing snow, Ann. Glaciol., 26, 138–143, https://doi.org/10.3189/1998AoG26-1-138-143, 1998.
  - Günther, D., Marke, T., Essery, R., and Strasser, U.: Uncertainties in Snowpack Simulations—Assessing the Impact of Model Structure, Parameter Choice, and Forcing Data Error on Point-Scale Energy Balance Snow Model Performance, Water Resour. Res., 55, 2779–2800, https://doi.org/10.1029/2018WR023403, 2019.
- Haddjeri, A., Baron, M., Lafaysse, M., Le Toumelin, L., Deschamps-Berger, C., Vionnet, V., Gascoin, S., Vernay, M., and Dumont, M.:
   Analyzing the sensitivity of a blowing snow model (SnowPappus) to precipitation forcing, blowing snow, and spatial resolution, The Cryosphere, 18, 3081–3116, https://doi.org/10.5194/tc-18-3081-2024, 2024.
  - Hadley, O. and Kirchstetter, T.: Black-Carbon reduction of snow albedo, Nat. Clim. Change, 2, 437–440, https://doi.org/10.1038/nclimate1433, 2012.





- Hanzer, F., Carmagnola, C., Ebner, P., Koch, F., Monti, F., Bavay, M., Bernhardt, M., Lafaysse, M., Lehning, M., Strasser, U., François,
   H., and Morin, S.: Simulation of snow management in Alpine ski resorts using three different snow models, Cold Reg. Sci. Tech., 172, https://doi.org/doi.org/10.1016/j.coldregions.2020.102995, 2020.
  - Herla, F., Horton, S., Mair, P., and Haegeli, P.: Snow profile alignment and similarity assessment for aggregating, clustering, and evaluating snowpack model output for avalanche forecasting, Geosci. Model Dev., 14, 239–258, https://doi.org/10.5194/gmd-14-239-2021, 2021.
- Jordan, R.: A One-Dimensional Temperature Model for a Snow Cover: Technical Documentation for SNTHERM. 89., Tech. rep., Cold Regions Research and Engineering Lab. Hanover NH, http://hdl.handle.net/11681/11677, 1991.
  - Kadioglu, S. Y., Nourgaliev, R. R., and Mousseau, V. A.: A Comparative Study of the Harmonic and Arithmetic Averaging of Diffusion Coefficients for Non-linear Heat Conduction Problems, Tech. rep., Idaho National Lab. (INL), Idaho Falls, ID (United States), https://doi.org/10.2172/928087, 2008.
- Kokhanovsky, A. and Zege, E.: Scattering optics of snow, Applied Optics, 43(7), 1589–1602, https://doi.org/doi:10.1364/AO.43.0001589, 2004.
  - Krinner, G., Derksen, C., Essery, R., Flanner, M., Hagemann, S., Clark, M., Hall, A., Rott, H., Brutel-Vuilmet, C., Kim, H., Ménard, C. B., Mudryk, L., Thackeray, C., Wang, L., Arduini, G., Balsamo, G., Bartlett, P., Boike, J., Boone, A., Chéruy, F., Colin, J., Cuntz, M., Dai, Y., Decharme, B., Derry, J., Ducharne, A., Dutra, E., Fang, X., Fierz, C., Ghattas, J., Gusev, Y., Haverd, V., Kontu, A., Lafaysse, M., Law, R., Lawrence, D., Li, W., Marke, T., Marks, D., Ménégoz, M., Nasonova, O., Nitta, T., Niwano, M., Pomeroy, J., Raleigh, M. S.,
- Schaedler, G., Semenov, V., Smirnova, T. G., Stacke, T., Strasser, U., Svenson, S., Turkov, D., Wang, T., Wever, N., Yuan, H., Zhou, W., and Zhu, D.: ESM-SnowMIP: assessing snow models and quantifying snow-related climate feedbacks, Geosci. Model Dev., 11, 5027–5049, https://doi.org/10.5194/gmd-11-5027-2018, 2018.
  - Lackmann, G. M., Keeter, K., Lee, L. G., and Ek, M. B.: Model Representation of Freezing and Melting Precipitation: Implications for Winter Weather Forecasting, Weather Forecast., 17, 1016 1033, https://doi.org/10.1175/1520-0434(2003)017<1016:MROFAM>2.0.CO;2, 2002.
  - Lackner, G., Domine, F., Nadeau, D. F., Parent, A.-C., Anctil, F., Lafaysse, M., and Dumont, M.: On the energy budget of a low-Arctic snowpack, The Cryosphere, 16, 127–142, https://doi.org/10.5194/tc-16-127-2022, 2022.
  - Lafaysse, M., Dumont, M., De Fleurian, B., Fructus, M., Nheili, R., Viallon-Galinier, L., Baron, M., Boone, A., Bouchet, A., Brondex, J., Carmagnola, C., Cluzet, B., Fourteau, K., Haddjeri, A., Hagenmuller, P., Mazzotti, G., Minvielle, M., Morin, S., Quéno, L., Roussel, L.,
- Spandre, P., Tuzet, F., and Vionnet, V.: Version 3.0 of the Crocus snowpack model: source code of implementation within SURFEX and externalized version, https://doi.org/10.5281/zenodo.16943240, 2025.
  - Lafaysse, M., Cluzet, B., Dumont, M., Lejeune, Y., Vionnet, V., and Morin, S.: A multiphysical ensemble system of numerical snow modelling, The Cryosphere, 11, 1173–1198, https://doi.org/10.5194/tc-11-1173-2017, 2017.
- Langlois., A., Brucker, L., Kohn, J., Royer, A., Derksen, C., Cliche, P., Picard, G., Fily, M., and Willemet, J.: Simulation of Snow Water Equivalent (SWE) using Thermodynamic Snow Models in southern Qébec between 2005 and 2006, J. Hydrometeorol., 10(6), 1447–1462, https://doi.org/10.1175/2009JHM1154.1, 2009.
  - Largeron, C., Dumont, M., Morin, S., Boone, A., Lafaysse, M., Metref, S., Cosme, E., Jonas, T., Winstral, A., and Margulis, S. A.: Toward Snow Cover Estimation in Mountainous Areas Using Modern Data Assimilation Methods: A Review, Front. Earth Sci., 8, https://doi.org/10.3389/feart.2020.00325, 2020.
- 1350 Le Roux, E., Evin, G., Eckert, N., Blanchet, J., and Morin, S.: A non-stationary extreme-value approach for climate projection ensembles: application to snow loads in the French Alps, Earth Syst Dyn, 13, 1059–1075, https://doi.org/10.5194/esd-13-1059-2022, 2022.

https://doi.org/10.1175/BAMS-D-19-0329.1, 2021.



1360



- Lehning, M., Bartelt, P., Brown, B., Russi, T., Stöckli, U., and Zimmerli, M.: SNOWPACK model calculations for avalanche warning based upon a new network of weather and snow stations, Cold Reg. Sci. Tech., 30, 145–157, https://doi.org/10.1016/S0165-232X(99)00022-1, 1999.
- Lehning, M., Bartelt, P., Brown, B., Fierz, C., and Satyawali, P.: A physical SNOWPACK model for the Swiss avalanche warning. Part II: snow microstructure., Cold Reg. Sci. Technol., 35, 147 167, https://doi.org/10.1016/S0165-232X(02)00073-3, 2002.
  - Lejeune, Y.: Apports des modèles de neige CROCUS et de sol ISBA à l'étude du bilan glaciologique d'un glacier tropical et du bilan hydrologique de son bassin, Ph.D. thesis, Université Joseph Fourier, Grenoble, France, https://theses.hal.science/tel-00480008/, 2009.
  - Lejeune, Y., Wagnon, P., Bouilloud, L., Chevallier, P., Etchevers, P., Martin, E., Sicart, E., and Habets, F.: Melting of snow cover in a tropical mountain environment in Bolivia: Processes and modeling, J. Hydrometeorol., 8(4), 922–937, https://doi.org/10.1175/JHM590.1, 2007.
  - Lejeune, Y., Dumont, M., Panel, J.-M., Lafaysse, M., Lapalus, P., Le Gac, E., Lesaffre, B., and Morin, S.: 57 years (1960–2017) of snow and meteorological observations from a mid-altitude mountain site (Col de Porte, France, 1325 m of altitude), Earth Syst. Sci. Data, 11, 71–88, https://doi.org/10.5194/essd-11-71-2019, 2019.
- Libois, Q., Picard, G., Arnaud, L., Dumont, M., Lafaysse, M., Morin, S., and Lefebvre, E.: Summertime evolution of snow specific surface area close to the surface on the Antarctic Plateau, The Cryosphere, 9, 2383–2398, https://doi.org/10.5194/tc-9-2383-2015, 2015.
  - Marbouty, D.: An experimental study of temperature-gradient metamorphism, J. Glaciol., 26, 303–312, https://doi.org/10.3189/S0022143000010844, 1980.
  - Martin, E. and Lejeune, Y.: Turbulent fluxes above the snow surface, Ann. Glaciol., 26, 179–183, https://doi.org/10.3189/1998AoG26-1-179-183, 1998.
- Masson, V., Le Moigne, P., Martin, E., Faroux, S., Alias, A., Alkama, R., Belamari, S., Barbu, A., Boone, A., Bouyssel, F., Brousseau, P., Brun, E., Calvet, J.-C., Carrer, D., Decharme, B., Delire, C., Donier, S., Essaouini, K., Gibelin, A.-L., Giordani, H., Habets, F., Jidane, M., Kerdraon, G., Kourzeneva, E., Lafaysse, M., Lafont, S., Lebeaupin Brossier, C., Lemonsu, A., Mahfouf, J.-F., Marguinaud, P., Mokhtari, M., Morin, S., Pigeon, G., Salgado, R., Seity, Y., Taillefer, F., Tanguy, G., Tulet, P., Vincendon, B., Vionnet, V., and Voldoire, A.: The SURFEXv7.2 land and ocean surface platform for coupled or offline simulation of Earth surface variables and fluxes, Geosci. Model Dev., 6, 929–960, https://doi.org/10.5194/gmd-6-929-2013, 2013.
  - Mazzotti, G., Nousu, J.-P., Vionnet, V., Jonas, T., Nheili, R., and Lafaysse, M.: Exploring the potential of forest snow modeling at the tree and snowpack layer scale, The Cryosphere, 18, 4607–4632, https://doi.org/10.5194/tc-18-4607-2024, 2024.
- Menard, C. B., Essery, R., Krinner, G., Arduini, G., Bartlett, P., Boone, A., Brutel-Vuilmet, C., Burke, E., Cuntz, M., Dai, Y., Decharme, B., Dutra, E., Fang, X., Fierz, C., Gusev, Y., Hagemann, S., Haverd, V., Kim, H., Lafaysse, M., Marke, T., Nasonova, O., Nitta, T.,
   Niwano, M., Pomeroy, J., Schädler, G., Semenov, V. A., Smirnova, T., Strasser, U., Swenson, S., Turkov, D., Wever, N., and Yuan, H.: Scientific and Human Errors in a Snow Model Intercomparison, Bulletin of the American Meteorological Society, 102, E61 E79,
  - Morin, S., Lejeune, Y., Lesaffre, B., Panel, J.-M., Poncet, D., David, P., and Sudul, M.: A 18-years long (1993 2011) snow and meteorological dataset from a mid-altitude mountain site (Col de Porte, France, 1325 m alt.) for driving and evaluating snowpack models, Earth Syst. Sci. Data, 4, 13–21, https://doi.org/10.5194/essd-4-13-2012, 2012.
  - Morin, S., Domine, F., Dufour, A., Lejeune, Y., Lesaffre, B., Willemet, J.-M., Carmagnola, C. M., and Jacobi, H.-W.: Measurements and modeling of the vertical profile of specific surface area of an alpine snowpack, Adv. Water Res., 55, 111–120, https://doi.org/10.1016/j.advwatres.2012.01.010, 2013.



1405

1415



- Morin, S., Horton, S., Techel, F., Bavay, M., Coléou, C., Fierz, C., Gobiet, A., Hagenmuller, P., Lafaysse, M., Ližar, M., Mitterer, C., Monti,
   F., Müller, K., Olefs, M., Snook, J. S., van Herwijnen, A., and Vionnet, V.: Application of physical snowpack models in support of operational avalanche hazard forecasting: A status report on current implementations and prospects for the future, Cold Reg. Sci. Tech.,
   170, 102 910, https://doi.org/10.1016/j.coldregions.2019.102910, 2020.
  - Morin, S., Samacoïts, R., François, H., Carmagnola, C. M., Abegg, B., Demiroglu, O. C., Pons, M., Soubeyroux, J.-M., Lafaysse, M., Franklin, S., Griffiths, G., Kite, D., Hoppler, A. A., George, E., Buontempo, C., Almond, S., Dubois, G., and Cauchy,
- A.: Pan-European meteorological and snow indicators of climate change impact on ski tourism, Climate Services, 22, 100215, https://doi.org/https://doi.org/10.1016/j.cliser.2021.100215, 2021.
  - Napoly, A., Boone, A., and Welfringer, T.: ISBA-MEB (SURFEX v8.1): model snow evaluation for local-scale forest sites, Geosci. Model Dev., 13, 6523–6545, https://doi.org/10.5194/gmd-13-6523-2020, 2020.
- Navari, M., Kumar, S., Wang, S., Geiger, J., Mocko, D. M., Arsenault, K. R., and Kemp, E. M.: Enabling Advanced Snow Physics Within

  Land Surface Models Through an Interoperable Model-Physics Coupling Framework, J. Adv. Model. Earth Syst., 16, e2022MS003 236, https://doi.org/10.1029/2022MS003236, 2024.
  - Navarre, J.: Modèle unidimensionnel d'évolution de la neige déposée: modèle perce-neige, La Météorologie, VI, 109-120, 1975.
  - Nicoud, B., Bayle, A., Corona, C., Chambard, R. P., Francon, L., Fructus, M., Bensa, M., and Choler, P.: Climate, not land-use, drives a recent acceleration of larch expansion at the forest-grassland ecotone in the southern French alps, Sci. Total Environ., 959, 178 326, https://doi.org/10.1016/j.scitotenv.2024.178326, 2025.
  - Niwano, M., Aoki, T., Kuchiki, K., Hosaka, M., and Kodama, Y.: Snow Metamorphism and Albedo Process (SMAP) model for climate studies: Model validation using meteorological and snow impurity data measured at Sapporo, J. Geophys. Res., 117, F03 008, https://doi.org/10.1029/2011JF002239, 2012.
- Noilhan, J. and Mahfouf, J.-F.: The ISBA land surface parameterization scheme, Glob. Planet. Change, 17, 145–159, https://doi.org/10.1016/0921-8181(95)00043-7, 1996.
  - Nousu, J.-P., Lafaysse, M., Vernay, M., Bellier, J., Evin, G., and Joly, B.: Statistical post-processing of ensemble forecasts of the height of new snow, Nonlin. Proc. Geophys., 26, 339–357, https://doi.org/10.5194/npg-26-339-2019, 2019.
  - Nousu, J.-P., Lafaysse, M., Mazzotti, G., Ala-aho, P., Marttila, H., Cluzet, B., Aurela, M., Lohila, A., Kolari, P., Boone, A., Fructus, M., and Launiainen, S.: Modeling snowpack dynamics and surface energy budget in boreal and subarctic peatlands and forests, The Cryosphere, 18, 231–263, https://doi.org/10.5194/tc-18-231-2024, 2024.
  - Olefs, M., Fischer, A., and Lang, J.: Boundary Conditions for Artificial Snow Production in the Austrian Alps., J. Appl. Meteorol. Climatol., 49, 1096–1113, https://doi.org/10.1175/2010JAMC2251.1, 2010.
  - Picard, G. and Libois, Q.: Simulation of snow albedo and solar irradiance profile with the two-stream radiative transfer in snow (TARTES) v2.0 model, EGUsphere, 2024, 1–42, https://doi.org/10.5194/egusphere-2024-1176, 2024.
- 1420 Quéno, L., Karbou, F., Vionnet, V., and Dombrowski-Etchevers, I.: Satellite products of incoming solar and longwave radiations used for snowpack modelling in mountainous terrain, Hydrology and Earth System Sciences Discussions, 2017, 1–33, https://doi.org/10.5194/hess-2017-563, 2017.
  - Quéno, L., Vionnet, V., Cabot, F., Vrécourt, D., and Dombrowski-Etchevers, I.: Forecasting and modelling ice layer formation on the snow-pack due to freezing precipitation in the Pyrenees, Cold Reg. Sci. Tech., 146, 19–31, https://doi.org/10.1016/j.coldregions.2017.11.007, 2018.



1430

1435



- Raleigh, M. S., Lundquist, J. D., and Clark, M. P.: Exploring the impact of forcing error characteristics on physically based snow simulations within a global sensitivity analysis framework, Hydrol. Earth Syst. Sci., 19, 3153–3179, https://doi.org/10.5194/hess-19-3153-2015, 2015.
- Reuter, B., Viallon-Galinier, L., Horton, S., van Herwijnen, A., Mayer, S., Hagenmuller, P., and Morin, S.: Characterizing snow instability with avalanche problem types derived from snow cover simulations, Cold Reg. Sci. Tech., 194, 103 462, https://doi.org/10.1016/j.coldregions.2021.103462, 2022.
- Reuter, B., Hagenmuller, P., and Eckert, N.: Trends in avalanche problems in the French Alps between 1958 and 2020, Cold Reg. Sci. Tech., 238, https://doi.org/10.1016/j.coldregions.2025.104555, 2025.
- Réveillet, M., Six, D., Vincent, C., Rabatel, A., Dumont, M., Lafaysse, M., Morin, S., Vionnet, V., and Litt, M.: Relative performance of empirical and physical models in assessing the seasonal and annual glacier surface mass balance of Saint-Sorlin Glacier (French Alps), The Cryosphere, 12, 1367–1386, https://doi.org/10.5194/tc-12-1367-2018, 2018.
- Reveillet, M., Dumont, M., Gascoin, S., Lafaysse, M., Nabat, P., Ribes, A., Nheili, R., Tuzet, F., Menegoz, M., Morin, S., Picard, G., and Ginoux, P.: Black carbon and dust alter the response of mountain snow cover under climate change, Nat. Commun., 13, https://doi.org/10.1038/s41467-022-32501-y, 2022.
- Revuelto, J., Lecourt, G., Lafaysse, M., Zin, I., Charrois, L., Vionnet, V., Dumont, M., Rabatel, A., Six, D., Condom, T., et al.: Multi1440 Criteria Evaluation of Snowpack Simulations in Complex Alpine Terrain Using Satellite and In Situ Observations, Remote Sens., 10, 
  1171, https://doi.org/10.3390/rs10081171, 2018.
  - Revuelto, J., Cluzet, B., Duran, N., Fructus, M., Lafaysse, M., Cosme, E., and Dumont, M.: Assimilation of surface reflectance in snow simulations: Impact on bulk snow variables, J. Hydrol., 603, 126 966, https://doi.org/10.1016/j.jhydrol.2021.126966, 2021.
- Ricchiazzi, P., Yang, S., Gautier, C., and Sowle, D.: SBDART: A Research and Teaching Software Tool for Plane-Parallel Radiative Transfer in the Earth's Atmosphere, Bull. Amer. Meteorol. Soc., 79, 2101 2114, https://doi.org/10.1175/1520-0477(1998)079<2101:SARATS>2.0.CO;2, 1998.
  - Roussel, L., Dumont, M., Gascoin, S., Monteiro, D., Bavay, M., Nabat, P., Ezzedine, J. A., Fructus, M., Lafaysse, M., Morin, S., and Maréchal, E.: Snowmelt duration controls red algal blooms in the snow of the European Alps, Proceedings of the National Academy of Sciences, 121, e2400362121, https://doi.org/10.1073/pnas.2400362121, 2024.
- 1450 Roussel, L., Dumont, M., Réveillet, M., Six, D., Kneib, M., Nabat, P., Fourteau, K., Monteiro, D., Gascoin, S., Thibert, E., Rabatel, A., Sicart, J.-E., Bonnefoy, M., Piard, L., Laarman, O., Jourdain, B., Fructus, M., Vernay, M., and Lafaysse, M.: Saharan dust impacts on the surface mass balance of Argentière Glacier (French Alps), EGUsphere, 2025, 1–48, https://doi.org/10.5194/egusphere-2025-1741, 2025.
  - Rousselot, M., Durand, Y., Giraud, G., Mérindol, L., Dombrowski-Etchevers, I., Déqué, M., and Castebrunet, H.: Statistical adaptation of ALADIN RCM outputs over the French Alps -application to future climate and snow cover, The Cryosphere, 6, 785–805, https://doi.org/10.5194/tc-6-785-2012, 2012.
  - Royer, A., Picard, G., Vargel, C., Langlois, A., Gouttevin, I., and Dumont, M.: Improved Simulation of Arctic Circumpolar Land Area Snow Properties and Soil Temperatures, Front. Earth Sci., 9, https://doi.org/10.3389/feart.2021.685140, 2021.
  - Sauter, T. and Obleitner, F.: Assessing the uncertainty of glacier mass-balance simulations in the European Arctic based on variance decomposition, Geosci. Model Dev., 8, 3911–3928, https://doi.org/10.5194/gmd-8-3911-2015, 2015.
- Schleef, S., Loewe, H., and Schneebeli, M.: Influence of stress, temperature and crystal morphology on isothermal densification and specific surface area decrease of new snow, The Cryosphere, 8, 1825–1838, https://doi.org/10.5194/tc-8-1825-2014, 2014.



1475



- Schmucki, E., Marty, C., Fierz, C., and Lehning, M.: Evaluation of modelled snowdepth and snow water equivalent at three contrasting sites in Switzerland using SNOWPACK simulations driven by different meteorological data input, Cold Reg. Sci. Technol., 99, 27–37, https://doi.org/10.1016/j.coldregions.2013.12.004, 2014.
- Skaugen, T., Luijting, H., Saloranta, T., Vikhamar-Schuler, D., and Müller, K.: In search of operational snow model structures for the future comparing four snow models for 17 catchments in Norway, Hydrol. Res., 49, 1929–1945, https://doi.org/10.2166/nh.2018.198, 2018.
  - Spandre, P., Morin, S., Lafaysse, M., Lejeune, Y., François, H., and George-Marcelpoil, E.: Integration of snow management processes into a detailed snowpack model, Cold Reg. Sci. Tech., 125, 48 64, https://doi.org/10.1016/j.coldregions.2016.01.002, 2016.
- Spandre, P., François, H., Verfaillie, D., Pons, M., Vernay, M., Lafaysse, M., George, E., and Morin, S.: Winter tourism under climate change in the Pyrenees and the French Alps: relevance of snowmaking as a technical adaptation, The Cryosphere, 13, 1325–1347, https://doi.org/10.5194/tc-13-1325-2019, 2019.
  - Strasser, U. and Etchevers, P.: Simulation of daily discharges for the upper Durance catchment (French Alps) using subgrid parameterization for topography and a forest canopy climate model, Hydrol. Process., 19, 2361–2373, https://doi.org/10.1002/hyp.5889, 2005.
  - Strasser, U., Etchevers, P., and Lejeune, Y.: Inter-Comparison of two Snow Models with Different Complexity using Data from an Alpine Site, Nordic Hydrology, 33, 15–26, https://doi.org/10.2166/nh.2002.0002, 2002.
  - Teufelsbauer, H.: A two-dimensional snow creep model for alpine terrain, Natural Hazards, 56, 481–497, https://doi.org/10.1007/s11069-010-9515-8, 2011.
  - Tuzet, F., Dumont, M., Picard, G., Lamare, M., Voisin, D., Nabat, P., Lafaysse, M., Larue, F., Revuelto, J., and Arnaud, L.: Quantification of the radiative impact of light-absorbing particles during two contrasted snow seasons at Col du Lautaret (2058 m a.s.l., French Alps), The Cryosphere, 14, 4553–4579, https://doi.org/10.5194/tc-14-4553-2020, 2020.
  - Tuzet, F., Dumont, M., Lafaysse, M., Picard, G., Arnaud, L., Voisin, D., Lejeune, Y., Charrois, L., Nabat, P., and Morin, S.: A multilayer physically based snowpack model simulating direct and indirect radiative impacts of light-absorbing impurities in snow, The Cryosphere, 11, 2633–2653, https://doi.org/10.5194/tc-11-2633-2017, 2017.
- Verfaillie, D., Lafaysse, M., Déqué, M., Eckert, N., Lejeune, Y., and Morin, S.: Multi-component ensembles of future meteorological and natural snow conditions for 1500 m altitude in the Chartreuse mountain range, Northern French Alps, The Cryosphere, 12, 1249–1271, https://doi.org/10.5194/tc-12-1249-2018, 2018.
  - Vernay, M., Lafaysse, M., Merindol, L., Giraud, G., and Morin, S.: Ensemble Forecasting of snowpack conditions and avalanche hazard, Cold Reg. Sci. Tech., 120, 251–262, https://doi.org/10.1016/j.coldregions.2015.04.010, 2015.
- Vernay, M., Lafaysse, M., Monteiro, D., Hagenmuller, P., Nheili, R., Samacoïts, R., Verfaillie, D., and Morin, S.: The S2M meteorological and snow cover reanalysis over the French mountainous areas: description and evaluation (1958–2021), Earth Syst. Sci. Data, 14, 1707–1733, https://doi.org/10.5194/essd-14-1707-2022, 2022.
  - Veyssière, G., Karbou, F., Morin, S., Lafaysse, M., and Vionnet, V.: Evaluation of Sub-Kilometric Numerical Simulations of C-Band Radar Backscatter over the French Alps against Sentinel-1 Observations, Remote Sens., 11, https://doi.org/10.3390/rs11010008, 2019.
- Viallon-Galinier, L., Hagenmuller, P., and Lafaysse, M.: Forcing and evaluating detailed snow cover models with stratigraphy observations, Cold Reg. Sci. Tech., 180, 103 163, https://doi.org/10.1016/j.coldregions.2020.103163, 2020.
  - Viallon-Galinier, L., Hagenmuller, P., Reuter, B., and Eckert, N.: Modelling snowpack stability from simulated snow stratigraphy: Summary and implementation examples, Cold Reg. Sci. Tech., 201, 103 596, https://doi.org/10.1016/j.coldregions.2022.103596, 2022.
  - Viallon-Galinier, L., Hagenmuller, P., and Eckert, N.: Combining modelled snowpack stability with machine learning to predict avalanche activity, The Cryosphere, 17, 2245–2260, https://doi.org/10.5194/tc-17-2245-2023, 2023.





- 1500 Viallon-Galinier, L., Lafaysse, M., Fructus, M., Vernay, M., and Radanovics, S.: Snowtools v2.0.3 python package for pre- and post-processing of SURFEX-Crocus snow model simulations., https://doi.org/10.5281/zenodo.17122726, 2025.
  - Vionnet, V., Brun, E., Morin, S., Boone, A., Martin, E., Faroux, S., Le-Moigne, P., and Willemet, J.-M.: The detailed snowpack scheme Crocus and its implementation in SURFEX v7.2, Geosci. Model. Dev., 5, 773–791, https://doi.org/10.5194/gmd-5-773-2012, 2012.
- Vionnet, V., Guyomarc'h, G., Bouvet, F. N., Martin, E., Durand, Y., Bellot, H., Bel, C., and Puglièse, P.: Occurrence of blowing snow events at an alpine site over a 10-year period: Observations and modelling, Adv. Water Res., 55, 53 63, https://doi.org/10.1016/j.advwatres.2012.05.004, 2013.
  - Vionnet, V., Martin, E., Masson, V., Guyomarc'h, G., Naaim-Bouvet, F., Prokop, A., Durand, Y., and Lac, C.: Simulation of wind-induced snow transport and sublimation in alpine terrain using a fully coupled snowpack/atmosphere model, The Cryosphere, 8, 395–415, https://doi.org/10.5194/tc-8-395-2014, 2014.
- 1510 Vionnet, V., Martin, E., Masson, V., Lac, C., Naaim Bouvet, F., and Guyomarc'h, G.: High-Resolution Large Eddy Simulation of Snow Accumulation in Alpine Terrain, J. Geophys. Res. Atmos., 122, 11,005–11,021, https://doi.org/10.1002/2017JD026947, 2017.
  - Vionnet, V., Guyomarc'h, G., Lafaysse, M., Naaim-Bouvet, F., Giraud, G., and Deliot, Y.: Operational implementation and evaluation of a blowing snow scheme for avalanche hazard forecasting, Cold Reg. Sci. Tech., 147, 1–10, https://doi.org/10.1016/j.coldregions.2017.12.006, 2018.
- 1515 Vionnet, V., Six, D., Auger, L., Dumont, M., Lafaysse, M., Quéno, L., Réveillet, M., Dombrowski Etchevers, I., Thibert, E., and Vincent, C.: Sub-kilometer precipitation datasets for snowpack and glacier modeling in alpine terrain, Front. Earth Sci., 7, 182, https://doi.org/10.3389/feart.2019.00182, 2019.
  - Vionnet, V., Verville, M., Fortin, V., Brugman, M., Abrahamowicz, M., Lemay, F., Thériault, J. M., Lafaysse, M., and Milbrandt, J. A.: Snow Level From Post-Processing of Atmospheric Model Improves Snowfall Estimate and Snowpack Prediction in Mountains, Water Resour. Res., 58, e2021WR031778, https://doi.org/10.1029/2021WR031778, 2022.
  - Vionnet, V., Leroux, N. R., Fortin, V., Abrahamowicz, M., Woolley, G., Mazzotti, G., Gaillard, M., Lafaysse, M., Royer, A., Domine, F., Gauthier, N., Rutter, N., Derksen, C., and Bélair, S.: Enhancing simulations of snowpack properties in land surface models with the Soil, Vegetation and Snow scheme v2.0 (SVS2), EGUsphere, 2025, 1–43, https://doi.org/10.5194/egusphere-2025-3396, 2025.
- Vionnet, V., Dombrowski-Etchevers, I., Lafaysse, M., Quéno, L., Seity, Y., and Bazile, E.: Numerical weather forecasts at kilometer scale in the French Alps: evaluation and applications for snowpack modelling, J. Hydrometeor., https://doi.org/10.1175/JHM-D-15-0241.1, 2016.
  - Wagnon, P., Lafaysse, M., Lejeune, Y., Maisincho, L., Rojas, M., , and Chazarin, J. P.: Understanding and modeling the physical processes that govern the melting of snow cover in a tropical mountain environment in Ecuador, J. Geophys. Res., 114, D19113, https://doi.org/10.1029/2009JD012292, 2009.
    - Warren, S.: Optical properties of snow, Rev. Geophys., 20, 67–89, https://doi.org/10.1029/RG020i001p00067, 1982.
- Wever, N., Fierz, C., Mitterer, C., Hirashima, H., and Lehning, M.: Solving Richards Equation for snow improves snowpack meltwater runoff estimations in detailed multi-layer snowpack model, The Cryosphere, 8, 257–274, https://doi.org/10.5194/tc-8-257-2014, 2014.
  - Wever, N., Vera Valero, C., and Fierz, C.: Assessing wet snow avalanche activity using detailed physics based snowpack simulations, Geophys. Res. Lett., 43, 5732–5740, https://doi.org/10.1002/2016GL068428, 2016b.
- Wever, N., Schmid, L., Heilig, A., Eisen, O., Fierz, C., and Lehning, M.: Verification of the multi-layer SNOWPACK model with different water transport schemes, The Cryosphere, 9, 2271–2293, https://doi.org/10.5194/tc-9-2271-2015, 2015.
  - Wever, N., Wurzer, S., Fierz, C., and Lehning, M.: Simulating ice layer formation under the presence of preferential flow in layered snow-packs, The Cryosphere, 10, 2731–2744, https://doi.org/10.5194/tc-10-2731-2016, 2016a.





- Wever, N., Comola, F., Bavay, M., and Lehning, M.: Simulating the influence of snow surface processes on soil moisture dynamics and streamflow generation in an alpine catchment, Hydrol. Earth Sci. Syst., 21, 4053–4071, https://doi.org/10.5194/hess-21-4053-2017, 2017.
- Woolley, G. J., Rutter, N., Wake, L., Vionnet, V., Derksen, C., Essery, R., Marsh, P., Tutton, R., Walker, B., Lafaysse, M., and Pritchard, D.: Multi-physics ensemble modelling of Arctic tundra snowpack properties, The Cryosphere, 18, 5685–5711, https://doi.org/10.5194/tc-18-5685-2024, 2024.
  - Yen, Y.-C.: Review of the thermal properties of snow, ice and sea ice, Tech. Rep. 81-10, Cold Regions Research and Engineering Laboratory, Hanover, NH, https://hdl.handle.net/11681/9469, 1981.
- 1545 Yepes-Arbós, X., van den Oord, G., Acosta, M. C., and Carver, G. D.: Evaluation and optimisation of the I/O scalability for the next generation of Earth system models: IFS CY43R3 and XIOS 2.0 integration as a case study, Geosci. Model Dev., 15, 379–394, https://doi.org/10.5194/gmd-15-379-2022, 2022.
- Zweigel, R. B., Westermann, S., Nitzbon, J., Langer, M., Boike, J., Etzelmüller, B., and Vikhamar Schuler, T.: Simulating Snow Redistribution and its Effect on Ground Surface Temperature at a High-Arctic Site on Svalbard, J. Geophys. Res. Earth. Surf., 126, e2020JF005 673, https://doi.org/10.1029/2020JF005673, 2021.